UiO : University of Oslo

Marte Julie Sætra

Computational modeling of ion concentration dynamics and metabolic oxygen consumption in brain tissue

Thesis submitted for the degree of Philosophiae Doctor

Department of Physics
Faculty of Mathematics and Natural Sciences

2020

Series of dissertations submitted to the
Faculty of Mathematics and Natural Sciences, University of Oslo
No. 2323

ISSN 1501-7710

Cover: Hanne Baadsgaard Utigard.
Print production: Reprosentralen, University of Oslo.

Acknowledgements

The present work was conducted at the Centre for Integrative Neuroplasticity (CINPLA) and the Department of Physics at the University of Oslo in the period 2016–2020, under the supervision of Prof. Gaute T. Einevoll, Dr. Geir Halnes, and Prof. Anders Malthe-Sørenssen.

First of all, I want to thank my excellent supervisors. Thank you for all you have taught me throughout these years, your enthusiasm and generosity, for inspiring me to engage in popular science, and supporting me in spending time on it.

To all the members at CINPLA: thank you for making the group such a friendly place. A special thanks to Solveig Næss and Elise Holter Thompson, who I have been lucky to share an office with. Your support has been invaluable.

I want to thank mamma and pappa for always being there for me, and finally: a big thanks to friends and family for all the cheers along the way.

Marte Julie Sætra
Oslo, August 2020

Abstract

To study the mammalian brain is no longer reserved the scientist with a lab coat. During the last decades, we have seen increased use of computers and mathematics as tools to understand this mysterious organ inside us. In the field of computational neuroscience, researchers make use of mathematical models – often based on physical laws – to explore brain function.

A major focus of computational neuroscience is on the electrical signals of neurons, and how they arise and propagate. The signals stem from the movement of ions through so-called ion channels in the neuronal membrane. The ionic flow depends on ion concentration differences between the inside and the outside of the cell. Such ion concentration differences are usually maintained by a large group of supporting mechanisms. This includes a type of structures known as ion pumps and cotransporters embedded in the neuronal membrane working to move ions in the opposite direction of the flow through ion channels. The pumps need energy to function and rely on a continuous supply of oxygen and glucose by the blood. Another important supporter is the astrocyte, a cell type belonging to a group of brain cells called neuroglia. The astrocyte helps preserve a proper chemical environment for the neurons, for example by taking up excess K^+ ions from the extracellular space.

Most computational modelers of neurons do not model the supporting mechanisms explicitly. They simply assume that the supporters do their job and set ion concentrations to be constant. However, the supporting mechanisms can be worth modeling – not only because of their faithful service but because of their ability to fail. The neural activity can be too high for the ion pumps and cotransporters to keep up with the activity, or they can suffer from a lack of energy supply. This may lead to dramatic changes in ion concentrations, which is seen in several pathological conditions, such as stroke and epilepsy.

In this thesis, I give the supporters their deserved attention. In the first part of my thesis (Paper I and Paper II), I model ion concentration dynamics and look at the contribution from ion pumps, cotransporters, and astrocytes. In the second part of my thesis (Paper III), I present a method for estimating the metabolic rate of oxygen consumption based on measurements of oxygen partial pressure in the rat cortex. An estimate of oxygen consumption can help us understand the coupling between neural activity, energy metabolism, and blood flow, and is an important indicator of brain function and pathology. Further, estimates of oxygen consumption can improve our understanding of functional magnetic resonance imaging (fMRI).

List of Papers

Paper I

Sætra, M.J., Einevoll, G.T., and Halnes, G. 'An electrodiffusice Pinsky–Rinzel model with homeostatic mechanisms'. In: *PLoS Computational Biology* vol. 16, no. 4 (2020), e1007661. DOI: 10.1371/journal.pcbi.1007661.

Paper II

Sætra, M.J., Einevoll, G.T., and Halnes, G. 'An electrodiffusive neuron-extracellular-glia model with somatodendritic interactions'. *Submitted for publication.*

Paper III

Sætra, M.J., Solbrå, A.V., Devor, A., Sakadžić, S., Dale, A.M., Einevoll, G.T. 'Spatially resolved estimation of metabolic oxygen consumption from optical measurements in cortex'. In: *Neurophotonics* vol. 7, no. 3 (2020), 035005. DOI: 10.1117/1.NPh.7.3.035005

Contents

Chapter 1

Introduction

1.1 What is this thesis about?

Every atom of the universe is subject to the laws of nature, also the atoms that make up your brain. Bound together by the natural forces, the brain atoms form more than 80 billion nerve cells [1], which we call *neurons*, each connected to thousands of other cells. When you think, feel, and interact with the outside world, the neurons fire electrical signals mediated by the movement of charged particles across their membranes.

The physical nature of brain activity allows us to study the human mind using physical laws and mathematics. An important foundation for this approach was laid by Alan Hodgkin (1914–1998) and Andrew Huxley (1917–2012), two British scientists who, in 1952, published a detailed mathematical model describing the generation and propagation of electrical signals within neurons [2]. The signals are known as *action potentials* and are seen as spontaneous voltage pulses if you measure them using an electrode (see Box 1.1).

Action potentials arise from the movement of *ions*, another word for charged particles, across the neuronal membrane. Hodgkin and Huxley saw from experiments that the movement was voltage-dependent and unique to different ion species. However, exactly *how* ions cross the membrane was unclear at the time. Hodgkin and Huxley did not know about the structures now known as *ion channels*, pore-like structures embedded in the neuronal membrane letting ions through the otherwise closed wall. Still, by fitting equations to experimental data from a squid neuron, Hodgkin and Huxley managed to develop a model that, in a precise and qualitative way, could describe the ionic currents across the membrane and how they give rise to action potentials.

The original Hodgkin–Huxley model only applied to the axon of a neuron but is now extended to describe electrical propagation through the whole cell. Much of Hodgkin and Huxley's methodology is still in use today and has formed the development of thousands of new models used to study both single cells and network dynamics. They also set the starting point for studying the biophysical properties of ion channels. Considering their impact on modern neuroscience, it is arguably the greatest success story of computational biology. The Hodgkin–Huxley model is the perfect example of how physics-based modeling of the brain can give new insight and set the path for further studies and new experiments.

Since the pioneering work of Hodgkin and Huxley, computational neuroscientists have paid a lot of attention to the electrical signals of neurons. The signals depend on a difference in ion concentrations across the neuronal membrane, or more precisely: the ionic flow giving rise to the electrical signals depends on ion concentration differences. The reason is that ions tend to move from places

of high concentrations to low concentrations and will stop moving if they even out. The gradient size is important as well, as larger differences give rise to stronger ionic currents and hence a different neural dynamic compared to smaller differences and weaker currents. A major assumption of most neuron models is that the ion concentration differences are maintained throughout the simulated period. The ion concentrations are, therefore, set constant.

Box 1.1: The neuron

The neuron is a complicated structure, with numerous thin cables branching out of a central body, the *soma*. If you insert an electrode, you will see that it measures a voltage across the cell's membrane, typically around $-65\,\mathrm{mV}$ in magnitude. This electrical property of the neuron and its intricate branching structure are essential for neuronal communication.

Most of the neuron's branches are so-called *dendrites* that receive electrochemical signals from other nerve cells. They forward these signals in the form of a current to the soma, and if the current is large enough, it will ignite a spontaneous voltage pulse called an *action potential*. Using your electrode, you will see the potential go from negative to positive, before it is back at baseline after a millisecond or so. The action potential then travels through a single branch called the *axon*, whose job is to make sure that the signal reaches other neurons. This journey can, for some neurons in your body, be as long as a meter. Axons are often wrapped in an insulating coating called the *myelin sheath*, making the transport of action potentials more efficient.

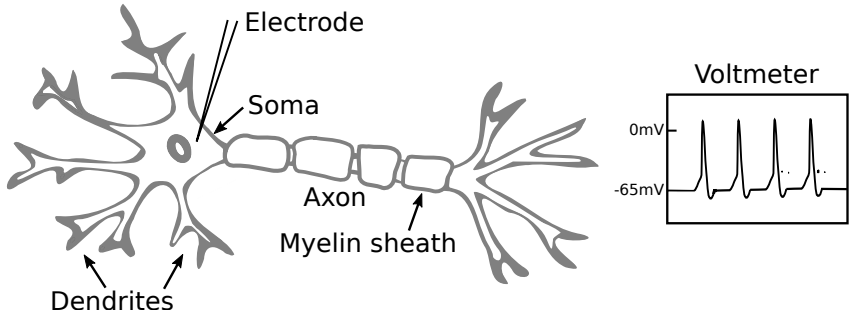

The figure is adapted from Solbrå, 2019 [3] and Wikimedia Commons [4].

To assume constant ion concentrations is reasonable in many cases. The number of ions needed to cross the membrane to generate an action potential is often insufficient to make a significant change in the ion concentrations (see, e.g., Box 2.3 in [5]). This was true for the experiments run by Hodgkin and Huxley, who studied a large axon from a squid, and it is true for many other axon types. Even after hundreds of action potentials, the assumption is often

justifiable. Modelers know, and rely on the fact, that behind every successful neuron, there is a huge machinery working to maintain a proper difference in ion concentrations.

Among the neurons' supporters are the so-called *ion pumps* and *cotransporters* — specialized structures embedded in the neuronal membrane. Their job is to move ions in the opposite direction of the flow through ion channels. There is a large family of ions dissolved in the intra- and extracellular fluid, flowing in different directions. The most abundant species are sodium (Na^+), potassium (K^+), and chloride (Cl^-). There is usually more K^+ on the inside of a neuron than on the outside, making K^+ flow outwards, and more Na^+ and Cl^- on the outside than on the inside, making Na^+ and Cl^- flow inwards. Different types of pumps and cotransporters take care of different ion species. The so-called *Na^+/K^+ pump* or *Na^+/K^+-ATPase* does a major job of transporting Na^+ out of the cell and K^+ into the cell.

Ion pumps and cotransporters need energy to function. The Na^+/K^+ pump stands for as much as 50 % of the brains' energy expenditure [6]. The energy comes from adenosine triphosphate (ATP) molecules, which release a large amount of energy if they convert to adenosine diphosphate (ADP). Cotranporters are different. They exploit that the unbalanced ion concentrations of a neuron have the ability to do useful work. When ions go from a place of high concentration to a place of lower concentration, the process releases energy. The energy can be used to transport other ions from lower to higher concentrations, which requires energy. An example of a cotransporter is the KCC2, which spends energy from K^+ concentration differences to restore the difference in Cl^- concentrations across the membrane. It transports one Cl^- ion out of the cell, from low to high concentrations, for every K^+ ion it carries in the same direction, but from high to lower concentrations. Note that the work of the KCC2 cotransporter still leads indirectly to the expenditure of ATP, since the K^+ ions that it transports into the cell eventually must be transported back by the Na^+/K^+ pump. To maintain a reservoir of ATP, the brain must be fueled with O_2 and glucose. There are little of these substrates in the brain, so brain function depends on a continuous supply of O_2 and glucose by the blood.

Another essential supporter is the *astrocyte*, a star-shaped cell type belonging to a group of brain cells called *neuroglia*, *glial cells*, or simply *glia*. Scientists used to believe that neuroglia works as passive, structural support for neurons. The term itself reflects the belief; the word glia is Greek and means *glue*. However, during the last 30 years, neuroglia has been recognized to perform a variety of different tasks.

A significant function of astrocytes is to maintain a proper chemical environment for the neurons, and they accomplish this task in different ways. For example, astrocytes help to avoid a build-up of K^+ in the extracellular space when neurons are active. They do so by taking up excess K^+ ions from sites of high extracellular K^+ concentration and distributing them to neighboring astrocytes that extrude the ions at sites of low extracellular K^+ concentration. This process is known as *K^+ spatial buffering* [7, 8]. In a similar process called *K^+ spatial siphoning*, astrocytes release K^+ ions directly into the bloodstream

[7, 9].

To put it all briefly: the brain is more than what most computational neuroscientists model. An ensemble of actors is at play and contributes to the big theater that represents *us*. In this thesis, I join forces with the supporting actors. Specifically, I model ion concentration dynamics and look at the contributions from cotransporters, ion pumps, and astrocytes. I also present a method for estimating the metabolic rate of oxygen consumption ($CMRO_2$) in brain tissue from measurements of oxygen partial pressure (pO_2).

1.2 Motivation

1.2.1 Motivation for modeling ion concentrations

Although the assumption of constant ion concentrations is valid in many cases, there are scenarios where it does not hold. Firstly, the ion concentrations may change during an action potential if the neuron is very thin. Hodgkin and Huxley studied an axon that is thicker than most axon types. The diameter of the squid giant axon is around 0.5 mm, and the volume is therefore big enough for the number of ions crossing the membrane during an action potential to not make a significant change to the ion concentrations. The diameter of a typical axon is closer to 1 µm, and some axons can be even thinner than this. In the smallest systems, the changes in ion concentrations can be notable on the time scale of a few action potentials [10]. Secondly, the pumps and cotransporters may fail to do their job. The neuron activity could be too high for the ion pumps and cotransporters to keep up with the ionic currents, or the ion pumps could fail because of a lack of energy supply.

Changes in ion concentrations are associated with a number of pathological conditions, such as seizures, stroke, and spreading depression. To study these conditions, we need models that account for changes in ion concentrations.

In Papers I and II, we highlight the importance of spreading depression. The condition was first described by Leão [11] as a wave of neural hyperactivity followed by silence, spreading throughout the entire cortex, the outer layer of the mammalian brain. Since Leão, spreading depression has been observed in most brain regions, in several animal species, and under various experimental conditions. It is associated with many other pathologies, including stroke, traumatic brain injury, migraine, and epileptic seizures [12–14].

1.2.2 Motivation for estimating oxygen consumption

An estimate of the $CMRO_2$ in brain tissue is key in understanding the tight coupling between neural activity, energy metabolism, and blood flow. A better understanding of these connections would give us deepened insight into diseases like stroke and Alzheimer's disease [15], and help us interpret some of the methods we use to study brain activity in humans [16, 17].

Measuring human brain activity is a challenging task because the measurements should preferably happen outside the head. Direct measurements using

electrodes inside the brain are, therefore, not an option in most cases. It is possible to capture electric and magnetic fields arising from neural activity using EEG and MEG recordings, where the electrodes are placed at the scalp, but it is hard to localize the source of these signals. An alternative approach is to utilize metabolic processes. One such method is functional magnetic resonance imaging (fMRI) based on a phenomenon called the blood oxygenation level-dependent (BOLD) effect. The technique is widely used, but its physiological basis is poorly understood.

The basis of BOLD fMRI is the method's sensitivity to the magnetic properties of hemoglobin, a molecule in blood that carries oxygen. When hemoglobin lets go of the O_2 it carries and becomes deoxyhemoglobin, its magnetic properties slightly change, and the change is caught by fMRI. An increase in blood oxygenation leads to an increase in the measured signal. When neurons are active, both cerebral blood flow and the $CMRO_2$ increase but not to the same extent. Cerebral blood flow, which increases blood oxygenation, increases more than the $CMRO_2$, which decreases the blood oxygenation. This leads to an overall increase in blood oxygenation and causes the fMRI signal to increase as well.

Because the BOLD signal depends on how much the cerebral blood flow has changed relative to how much the $CMRO_2$ has changed, fMRI is hard to interpret as a measure of neural activity unless we understand how these three measures relate to each other. Like Devor et al. question in [16], how do you know if different BOLD responses, for example from different tasks, are caused by different neural activity, a different response in oxygen delivery by blood, or a different $CMRO_2$? To study this, we need measures of the three components. Standard methods exist for measuring neural activity and blood flow, but there is no "gold standard" for measuring the $CMRO_2$.

1.3 My contribution

1.3.1 My contribution to modeling ion concentrations

A key challenge when modeling ion concentration dynamics is to account for all ionic movement. The movement of ions is driven by two processes: diffusion and electric drift. Diffusion describes the tendency of ions to move from a place of high concentration to a place of lower concentration. It is the same process you observe if you spill a drop of ink in a glass of water; the drop will slowly spread until it is evenly distributed throughout the glass. Electric drift is the process where ions, because of their charge, move in the presence of an electric field, which is expressed as a difference in electrical potential. Positively charged ions will move from a place of high electric potential to a place of lower electric potential, and negatively charged ions will move in the opposite direction. A single ion in a vacuum would accelerate in the presence of an electric field, but in neurons, ions collide with each other and lose momentum. As a consequence, ions travel at an average speed that depends on the potential difference. The joint effect of diffusion and electric drift is called electrodiffusion.

In neurons, diffusion and electric drift carry ions across the membrane and longitudinally in the intra- and extracellular space. Since ions carry charge, they affect the electrical potentials, and electrical potentials affect the movement of ions via electric drift. To my knowledge, no available neuron model accounts for this relationship in a consistent way, both intracellularly and extracellularly, and with the contribution from both longitudinal currents and membrane currents. Several models exist that include ion concentration dynamics, but many are so-called *single-compartment models*, meaning that they do not account for the neuron's spatial extension and, therefore, only consider the membrane currents, see e.g [18–32]. Among the models *with* spatial extension, neither account for electric drift, only diffusion, see e.g. [33–41]. In this way, they miss the electrodiffusive coupling between the movement of ions and electrical potentials.

In this thesis, I model spatially extended neurons in an electrodiffusive consistent way. Paper I presents a system containing a single neuron and extracellular space, and Paper II presents a system comprising a neuron, extracellular space, and an astrocyte. The model in Paper II also accounts for cellular swelling, another consequence of ion concentration differences. Ions create an osmotic pressure on both sides of the cell membrane, and water tends to move from places of high osmotic pressure to places of low osmotic pressure. This changes the cell volume as water fills or empties the cell.

1.3.2 My contribution to estimating oxygen consumption

Traditionally, $CMRO_2$ has been estimated from combined measurements of blood flow and oxygenation, but researchers question the accuracy of the results [42]. However, recent development in two-photon microscopy imaging makes it possible to estimate $CMRO2_2$ from a single quantity only, namely the pO_2, which relates to the concentration of O_2 through Henry's law, that is, $[O_2] = \alpha \cdot pO_2$, where α is the solubility coefficient. The two-photon microscopy technique makes it possible to measure pO_2 in tissue with a high spatial resolution [43].

In Sakadžić et al. (2016) [42], they estimated the $CMRO_2$ around diving arterioles in rat cortex using the so-called *Krogh method* [44]. The method is limited to tissue surrounding single blood vessels, assumes a circular symmetry of the pO_2, and outputs a single estimate of the $CMRO_2$, that is, it assumes a homogenous $CMRO_2$. For diving arterioles, Sakadžić et al. argue that this is a reasonable assumption, as the arterioles seem to be responsible for oxygen supply within a radius of $\sim 100\,\mu$m. However, in cases where several blood vessels provide the oxygen, or the $CMRO_2$ is inhomogenous, the method can not be used.

In Paper III, we present a new method of estimating $CMRO_2$. It is based on the same type of two-photon measurements as the Krogh method, but does not assume that a single vessel provides all the oxygen, and it outputs a spatially resolved map of $CMRO_2$, rather than a single estimate.

Chapter 2

Methods

This chapter is intended for those who want a bit more technical introduction to the papers than what is provided in Chapter 1. You can skip this chapter and still understand, at least most of, Chapters 3 and 4.

2.1 Ion concentration dynamics

Most computational models of neurons assume ion concentrations to remain constant over the simulated period. In this section, I present how the assumption is incorporated into the Hodgkin–Huxley type models, what the models lack to account for ion concentration dynamics, and, to some extent, how ion concentrations affect neuronal signaling. As an example, I will present the Pinsky–Rinzel model [45], which we used in Paper I as a starting point to develop an electrodiffusive neuron model with ion concentration dynamics.

2.1.1 The Pinsky–Rinzel model

When modeling neurons, there are many ways to represent the cell morphology. In the most simplified cases, the neuron is represented as a single point, with one equation describing the membrane potential. To account for the neuron's spatial extension, one can instead divide the neuron into multiple compartments (see Fig 2.1), and assign an equation to each of them. This approach is usually referred to as *compartmental modeling*.

Some compartmental models include thousands of compartments, which allow for a detailed description of the neuron. However, to reduce a model's complexity by including only a few compartments can be useful in many ways. In fact, by stripping models down to their bare essentials, they may be easier to interpret than their more complex siblings. Reduced compartmental models are also more computationally efficient and are, for this reason, useful when modeling networks of cells.

The Pinsky–Rinzel model includes two compartments: one is representing the neuron's soma, and one is representing its dendrites. It is a reduced version of the Traub model, a 19-compartment model of a hippocampal pyramidal cell [46].

The membrane potentials of the two compartments are given by the following

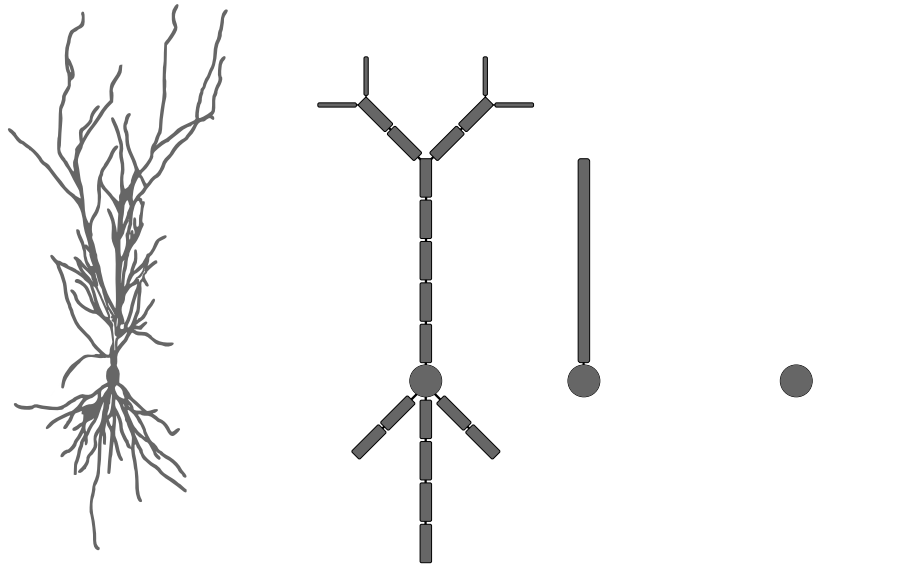

Fig 2.1. Compartmental modeling of neurons. We can represent a neuron's morphology (left) by dividing the neuron into compartments (right). By reducing the number of compartments, we also reduce the level of detail in our model (going from left to right). The figure is adapted from Tennøe, 2019 [47] using the morphology of a CA2 pyramidal cell in mice, NeuroMorpho.Org ID: NMO_112049 [48].

differential equations:

$$C_{\mathrm{m}}\frac{dV_{\mathrm{s}}}{dt} = -g_{\mathrm{Na}}(V_{\mathrm{s}}-E_{\mathrm{Na}}) - g_{\mathrm{DR}}(V_{\mathrm{s}}-E_{\mathrm{K}}) - \bar{g}_{\mathrm{L}}(V_{\mathrm{s}}-E_{\mathrm{L}}) + \frac{g_{\mathrm{c}}}{p}(V_{\mathrm{d}}-V_{\mathrm{s}}) + \frac{I_{\mathrm{s}}}{p}, \tag{2.1}$$

$$C_{\mathrm{m}}\frac{dV_{\mathrm{d}}}{dt} = -g_{\mathrm{Ca}}(V_{\mathrm{d}}-E_{\mathrm{Ca}}) - g_{\mathrm{AHP}}(V_{\mathrm{d}}-E_{\mathrm{K}}) - g_{\mathrm{C}}(V_{\mathrm{d}}-E_{\mathrm{K}}) - \bar{g}_{\mathrm{L}}(V_{\mathrm{d}}-E_{\mathrm{L}}) + \frac{g_{\mathrm{c}}}{1-p}(V_{\mathrm{s}}-V_{\mathrm{d}}). \tag{2.2}$$

The equations are equivalent to the description of an electric circuit, illustrated in Fig 2.2. The vertical resistors represent the membrane's ion channels, and the capacitors represent the membrane's channel-free parts. The horizontal resistor represents the coupling between the soma and the dendrites.

In Eq 2.1, V_{s} is the somatic membrane potential, $-g_{\mathrm{Na}}(V_{\mathrm{s}}-E_{\mathrm{Na}})$ describes a Na^+ current (I_{Na}), $-g_{\mathrm{DR}}(V_{\mathrm{s}}-E_{\mathrm{K}})$ describes a delayed rectifyer K^+ current (I_{DR}), $g_{\mathrm{c}}(V_{\mathrm{d}}-V_{\mathrm{s}})/p$ describes the intracellular current (I_{c}), I_{s} describes a current injected by an electrode, and $-\bar{g}_{\mathrm{L}}(V_{\mathrm{s}}-E_{\mathrm{L}})$ describes the so-called *leak*

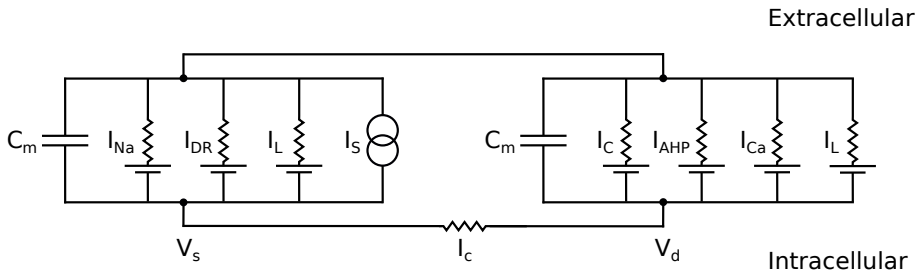

Fig 2.2. Circuit diagram of the Pinsky–Rinzel model. A neuron can be represented as an electric circuit where resistors resemble ion channels, and capacitors resemble the channel-free parts of the membrane. Here, the vertical resistor resembles the coupling between the soma (left) and the dendrites (right), and I_S is the current injected by an electrode. The figure is adapted from Sterratt et al., 2011 [5].

current (I_{leak}). The leak current represents the summed contribution from all sorts of processes that are not modeled explicitly by the other ion channels. These include the pumps and cotransporters and the transport of positively and negatively charged ions through passive leakage channels, that is, channels with static ion conductance.

In Eq 2.2, V_d is the dendritic membrane potential, $-g_{Ca}(V_d - E_{Ca})$ describes a Ca^{2+} current (I_{Ca}), $-g_{AHP}(V_d - E_K)$ describes a K^+ afterhyperpolarization current (I_{AHP}), $-g_C(V_d - E_K)$ describes a calcium-dependent K^+ current (I_C), $-\bar{g}_L(V_s - E_L)$ describes the leak current (I_{leak}), and $g_c(V_s - V_d)/(1-p)$ describes the intracellular current (I_c). Further, $C_m = 3\,\mu\text{Fcm}^{-2}$ is the membrane capacitance, $p = 0.5$ is the proportion of the membrane that is taken up by the soma, g's are ion conductances, and E's are so-called *reversal potentials* (see Sec 2.1.2 below).

The ion conductances of the active channels are given by

$$g_{Na} = \bar{g}_{Na} m_\infty^2 h, \tag{2.3}$$

$$g_{DR} = \bar{g}_{DR} n, \tag{2.4}$$

$$g_{Ca} = \bar{g}_{Ca} s^2, \tag{2.5}$$

$$g_C = \bar{g}_C c \chi([Ca^{2+}]), \tag{2.6}$$

$$g_{AHP} = \bar{g}_{AHP} q, \tag{2.7}$$

where $\bar{g}_{Na}$, $\bar{g}_{DR}$, $\bar{g}_{Ca}$, $\bar{g}_C$, and $\bar{g}_{AHP}$ are maximum conductances, χ is a function of Ca^{2+} given by

$$\chi([Ca^{2+}]) = \min([Ca^{2+}]/250, 1), \tag{2.8}$$

and m_∞, h, n, s, c, and q, are state variables that vary between 0 and 1, depending on the membrane potential or the intracellular Ca^{2+} concentration. Hodgkin–Huxley type models are characterized by their use of state variables to calculate ion conductances. The state variables are found by solving the

following equation:

$$\frac{dx}{dt} = \alpha_{\mathrm{x}}(1-x) - \beta_{\mathrm{x}}x, \quad \text{with } x = h, n, s, c, q, \tag{2.9}$$

except m_∞, which is given by:

$$m_\infty = \frac{\alpha_{\mathrm{m}}}{\alpha_{\mathrm{m}} + \beta_{\mathrm{m}}}. \tag{2.10}$$

The parameters α and β are rate coefficients given by:

$$\begin{aligned}
\alpha_{\mathrm{m}} &= -\frac{0.32V_1}{\exp(-V_1/4)-1}, & \beta_{\mathrm{m}} &= \frac{0.28V_2}{\exp(V_2/5)-1},\\
\alpha_{\mathrm{h}} &= 0.128\exp\left(\frac{-43-V}{18}\right), & \beta_{\mathrm{h}} &= \frac{4}{1+\exp(-V_5/5)},\\
\alpha_{\mathrm{n}} &= -\frac{0.016V_3}{\exp(-V_3/5)-1}, & \beta_{\mathrm{n}} &= 0.25\exp\left(\frac{-V_4}{40}\right),\\
\alpha_{\mathrm{s}} &= -\frac{1.6}{1+\exp(-0.072(V-5))}, & \beta_{\mathrm{s}} &= \frac{0.02V_6}{\exp(V_6/5)-1},\\
\alpha_{\mathrm{q}} &= \min(0.00002[\mathrm{Ca}^{2+}], 0.01), & \beta_{\mathrm{q}} &= 0.001,
\end{aligned} \tag{2.11}$$

$$\alpha_{\mathrm{c}} = \begin{cases} 0.0527\exp\left(\frac{V_8}{11} - \frac{V_7}{27}\right) & \text{for } V \le -10\,\mathrm{mV},\\ 2\exp(-V_7/27) & \text{otherwise,}\end{cases}$$

$$\beta_{\mathrm{c}} = \begin{cases} 2\exp(-V_7/27) - \alpha_{\mathrm{c}} & \text{for } V \le -10\,\mathrm{mV},\\ 0 & \text{otherwise,}\end{cases}$$

where $V_1 = V + 46.9$, $V_2 = V + 19.9$, $V_3 = V + 24.9$, $V_4 = V + 40$, $V_5 = V + 20$, $V_6 = V + 8.9$, $V_7 = V + 53.5$, and $V_8 = V + 50$ in units of mV. Since g_{C} and g_{AHP} are Ca^{2+}-dependent, we need to know the intracellular Ca^{2+} concentration of the dendrites. It is calculated from:

$$\frac{d[\mathrm{Ca}^{2+}]}{dt} = -0.13I_{\mathrm{Ca}} - 0.075[\mathrm{Ca}^{2+}]. \tag{2.12}$$

The values of the maximum conductances, in units of mScm^{-2}, are:

$$\bar{g}_{\mathrm{L}} = 0.1, \quad \bar{g}_{\mathrm{Na}} = 30, \quad \bar{g}_{\mathrm{DR}} = 15, \quad \bar{g}_{\mathrm{Ca}} = 10, \quad \bar{g}_{\mathrm{AHP}} = 0.8, \quad \bar{g}_{\mathrm{C}} = 15. \tag{2.13}$$

The reversal potentials are

$$E_{\mathrm{L}} = -68\,\mathrm{mV}, \quad E_{\mathrm{Na}} = 60\,\mathrm{mV}, \quad E_{\mathrm{K}} = -75\,\mathrm{mV}, \quad E_{\mathrm{K}} = 80\,\mathrm{mV}. \tag{2.14}$$

I have listed the model equations and parameter values like they are given in [5] (with errata in [49]), except the leak reversal potential, which value is taken from Paper I. I have implemented the model in Python and made it available at https://github.com/CINPLA/PRmodel. An example simulation is shown in Fig 2.3.

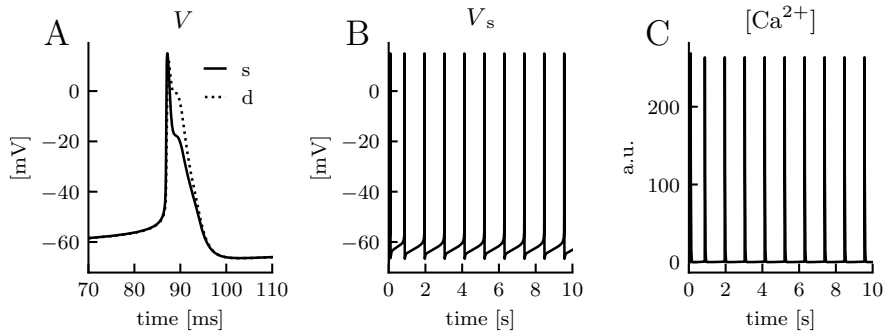

Fig 2.3. Example simulation of the Pinsky–Rinzel model. I ran the Pinsky–Rinzel model for 10 s with a constant stimulus current making the neuron fire with a firing rate of 1 Hz. **A:** Snapshot of the first action potential. The solid line shows the somatic membrane potential, and the dotted line shows the dendritic membrane potential. **B:** The somatic membrane potential over the full simulation period. **C:** The intracellular Ca^{2+} concentration of the dendrites. **A-C:** Parameter values: the stimulus current $I_S = 0.78\,\mu A/cm^2$, and the coupling conductance $g_c = 10.5\,mS/cm^2$.

2.1.2 Reversal potentials

The reversal potential E_k describes at which membrane potential the ionic current of an ion species k is zero. To understand the reversal potential, imagine that we have a box with two compartments, one to the left and one to the right. The compartments are separated by a membrane and filled with positively and negatively charged ions, let us call them P^+ and N^-. There are more ions in the left compartment than in the right compartment, but no net charge (Fig 2.4A).

We now do a thought experiment where we make the membrane separating the two compartments permeable to P^+ and N^-. Because of diffusion, the ions will start to flow from the compartment with high concentrations to the compartment with low concentrations (Fig 2.4B). The flow will continue until there is an equal amount of ions on both sides of the membrane (Fig 2.4C).

In a second thought experiment, we let the membrane be permeable to the P^+ ions only (Fig 2.5A). The P^+ ions will start to flow from high to low concentrations due to diffusion. Once an ion crosses the membrane, the electroneutrality will break, and the charge will create a potential difference between the two compartments (Fig 2.5B). As positively charged ions tend to move from places of high electric potential to places of low electric potential, the potential difference will oppose the diffusion. As more ions diffuse, the potential difference grows bigger, and after some time, the diffusion and electric drift components will be equally large. The transport of ions is now zero (Fig 2.5C), and the potential across the membrane is equal to what we call the *reversal potential*.

We can derive an expression for the reversal potential from the *Nernst–Planck*

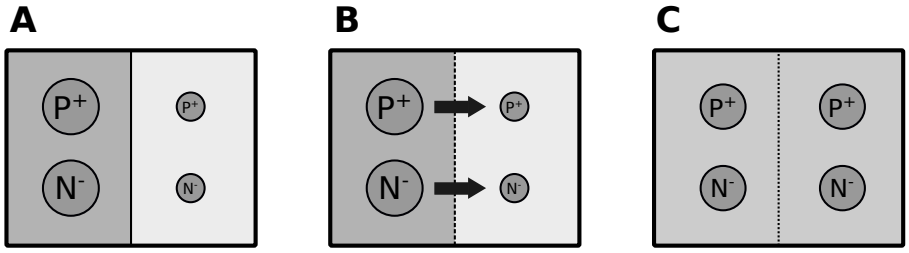

Fig 2.4. Illustration of diffusion. Diffusion is when molecules go from a place of high concentration to a place of low concentration. **A:** In a thought experiment, imagine that you have a box with two compartments. The compartments are separated by a membrane and filled with ions: P^+ and N^-. There are more ions in the left compartment than in the right compartment, but both of them are electroneutral. **B:** We make the membrane separating the two compartments permeable to the ions. The ions will flow from the compartment with high concentrations to the compartment with low concentrations until the ions are evened out **(C)**. The figure is adapted from Sterratt et al., 2011 [5].

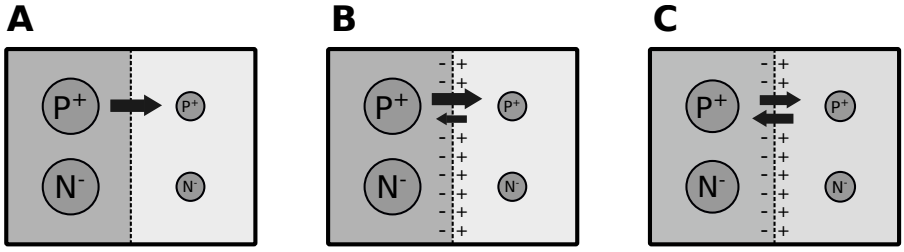

Fig 2.5. Illustration of electrodiffusion. Electrodiffusion is the joint effect of diffusion (see Fig 2.4) and electric drift, which is when ions go from a place of high electric potential to a place of lower electric potential. **A:** Imagine the same box as in Fig 2.4, except that the membrane is permeable only to the P^+ ions. The P^+ ions will start to flow from the compartment with high concentrations to the compartment with low concentrations due to diffusion. **B:** Because of the ions' charge, the flow will cause a potential difference across the membrane. The potential difference will oppose the diffusion due to electric drift. **C:** After some time, the diffusion and the electric drift components will be equally large, making the transport of P^+ zero. The figure is adapted from Sterratt et al., 2011 [5].

equation, which describes the electrodiffusive transport of ions in a given medium. On the general form, the Nernst–Planck equation reads:

$$j_{\mathrm{k}} = -D_{\mathrm{k}}\nabla[\mathrm{k}] - \frac{D_{\mathrm{k}} z_{\mathrm{k}} F}{RT}[\mathrm{k}]\nabla V. \tag{2.15}$$

Here, j_{k} describes the flux of a given ion species k, that is, the amount of ions flowing through a unit area per unit time, D_{k} is the diffusion coefficient, [k] is the ion concentration, z_{k} is the ionic charge number, F is the Faraday constant, R is the gas constant, T is absolute temperature, and V is the potential. The first term is known as *Fick's first law* and describes diffusion, and the second term is the electric drift component. To describe electrodiffusion across a membrane, we exchange D_{k} with the membrane permeability P_{k}.

For a discrete one-dimensional system, Eq 2.15 for electrodiffusion across a membrane simplifies to:

$$j_{\mathrm{k}} = -P_{\mathrm{k}}\frac{d[\mathrm{k}]}{dx} - \frac{P_{\mathrm{k}} z_{\mathrm{k}} F}{RT}[\mathrm{k}]\frac{dV}{dx}. \tag{2.16}$$

To derive the reversal potential from 2.16, we start by setting the ionic flux equal to zero, which gives:

$$\frac{1}{[\mathrm{k}]}\frac{d[\mathrm{k}]}{dx} = -\frac{z_{\mathrm{k}} F}{RT}\frac{dV}{dx}. \tag{2.17}$$

By integrating across the membrane, we obtain:

$$-\int_{V_{\mathrm{left}}}^{V_{\mathrm{right}}} dV = \int_{[\mathrm{k}]_{\mathrm{left}}}^{[\mathrm{k}]_{\mathrm{right}}} \frac{RT}{z_{\mathrm{k}} F[\mathrm{k}]} d[\mathrm{k}] \tag{2.18}$$

$$V_{\mathrm{left}} - V_{\mathrm{right}} = \frac{RT}{z_{\mathrm{k}} F}\ln\frac{[\mathrm{k}]_{\mathrm{right}}}{[\mathrm{k}]_{\mathrm{left}}} \tag{2.19}$$

The potential difference $V_{\mathrm{left}} - V_{\mathrm{right}}$ equals the reversal potential E_{k}. For neurons, a potential difference across the membrane is, by definition, defined as the intracellular potential minus the extracellular potential, which gives us the following expression for E_{k}:

$$E_{\mathrm{k}} = \frac{RT}{z_{\mathrm{k}} F}\ln\frac{[\mathrm{k}]_{\mathrm{out}}}{[\mathrm{k}]_{\mathrm{in}}}, \tag{2.20}$$

where $[\mathrm{k}]_{\mathrm{in}}$ and $[\mathrm{k}]_{\mathrm{out}}$ are the intra- and extracellular ion concentrations, respectively. Equation 2.20 is known as the *Nernst equation*.

As an example, let us calculate the reversal potential of K^+ using the initial K^+ concentrations in Paper I, and a temperature of 309 K:

$$E_{\mathrm{K}} = \frac{(8.314\,\mathrm{J/(molK)})(309\,\mathrm{K})}{(+1)(9.648\cdot 10^4\,\mathrm{C/mol})}\ln\frac{5.9\,\mathrm{mM}}{139.5\,\mathrm{mM}} = -84\,\mathrm{mV}. \tag{2.21}$$

This tells us that if the membrane potential is higher than −84 mV, the diffusive current of K^+ will be greater than the electric drift, and K^+ will, therefore, flow

outwards. If the membrane potential gets below $-84\,\mathrm{mV}$, the electric drift will dominate and make the K^+ flow inwards. This change of direction is why it is called the reversal potential. It is also known as the *equilibrium potential*, as E_K represents at which membrane potential the K^+ current is zero, that is, when the diffusive and electric drift components are in equilibrium.

2.1.3 The resting membrane potential

The resting membrane potential of a neuron lies somewhere between the reversal potentials of the different ion species. We can use the *Goldman–Hodgkin–Katz voltage equation* to calculate its value. For a membrane that is permeable to Na^+, K^+, and Cl^-, the Goldman–Hodgkin–Katz equation reads:

$$E_m = \frac{RT}{F} \ln \frac{P_K[K^+]_{out} + P_{Na}[Na^+]_{out} + P_{Cl}[Cl^-]_{in}}{P_K[K^+]_{in} + P_{Na}[Na^+]_{in} + P_{Cl}[Cl^-]_{out}}. \tag{2.22}$$

In Eq 2.22, R is the gas constant, T is the absolute temperature, F is the Faraday constant, P's are membrane permeabilities, and $[k]_{in}$ and $[k]_{out}$ are the intra- and extracellular concentrations of ion species k, respectively. Typical values of the reversal potentials are given in Eq 2.14, and a typical resting potential of a mammalian neuron lies around $-70\,\mathrm{mV}$ to $-65\,\mathrm{mV}$. A negative membrane potential indicates a more negative inside.

The reversal potential of Na^+ is above the resting potential, so Na^+ ions will flow inwards through open channels, making the inside more positive. The K^+ reversal potential is below the resting potential, so K^+ will flow outwards through open channels, making the inside more negative. However, the membrane is much more permeable to K^+ than it is to Na^+, so K^+ has the biggest influence on the resting membrane potential.

2.1.4 The assumption of constant ion concentrations

The Pinsky–Rinzel model may seem like it has nothing to do with ion concentrations at first glance, but that is not true. As we saw in Sec 2.1.2, the reversal potentials depend on ion concentrations. If we assume the ion concentrations to not change over time, the reversal potentials will not change either and can be given constant values. That is how the assumption is incorporated into the model.

To equip the Pinsky–Rinzel model with ion concentrations dynamics, we must, in short, start by adding currents that represent pumps and cotransporters. Secondly, we must make the leak currents ion-specific. Thirdly, we must add equations that keep track of ion concentrations, and finally, we must calculate the reversal potentials of the different ion species at each time step (Eq 2.20).

Changes in ion concentrations will then affect the neural dynamics through changes in the reversal potentials. If, for example, the K^+ concentration difference becomes smaller due to a build-up of K^+ in the extracellular space, E_K will increase. This will affect the K^+ current, which again affects the membrane potential, and hence the firing pattern of the cell. In the most extreme case,

changes in ion concentrations can make the neuron incapable of firing new action potentials.

2.1.5 The KNP framework for ion concentration dynamics

In Papers I and II, we use the Kirchoff–Nernst–Planck (KNP) framework [50, 51] to model ion concentration dynamics. The framework starts with the *continuity equation*, which gives us the time evolution of an ion concentration [k] within a given volume:

$$\frac{\partial[\mathrm{k}]}{\partial t} = -\nabla \cdot j_{\mathrm{k}} + f_{\mathrm{k}}. \tag{2.23}$$

Equation 2.23 is the mathematical way of saying that the amount of ions within a volume must change by the amount flowing into or out of the volume's boundaries, plus the amount flowing into a sink or out of a source. In our case, j_{k} is the intra- or extracellular flux of ions and f_{k} represents all ions of ion species k flowing into or out of the neuronal membrane. We use the Nernst–Planck equation (Eq 2.15) to describe the intra- and extracellular fluxes, and by combining Eqs 2.15 and 2.23, we get:

$$\frac{\partial[\mathrm{k}]}{\partial t} = \nabla \cdot \left[D_{\mathrm{k}} \nabla[\mathrm{k}] + \frac{D_{\mathrm{k}} z_{\mathrm{k}} F}{RT}[\mathrm{k}] \nabla V \right] + f_{\mathrm{k}}. \tag{2.24}$$

In reality, brain tissue is not a continuous medium. Ions crash into obstacles and are limited by the volume they have to their disposal. Neurons take up around 40 % of the tissue volume, and the ECS takes up only 20 % [52]. To account for this, one can use the porous medium approximation [53], which affects Eq 2.24 in two ways. Firstly, it modifies the diffusion constant of ion species k as:

$$\tilde{D}_{\mathrm{k}} = \frac{D_{\mathrm{k}}}{\lambda^2}, \tag{2.25}$$

where λ is a unitless parameter called the *tortuosity*. It accounts for the extra distance that ions need to move to get past various hindrances. Secondly, it modifies the source term as:

$$\tilde{f}_{\mathrm{k}} = \frac{f_{\mathrm{k}}}{\alpha}, \tag{2.26}$$

where α is the relevant volume fraction.

For a discrete, one-dimensional system, like the one illustrated in Fig 2.6, Eq 2.24 with modifications simplifies to:

$$\frac{d[\mathrm{k}]}{dt} = \left[-\tilde{D}_{\mathrm{k}} \frac{d[\mathrm{k}]}{dx} - \frac{\tilde{D}_{\mathrm{k}} z_{\mathrm{k}} F}{RT} \overline{[\mathrm{k}]} \frac{dV}{dx} \right] \cdot \frac{A_{\mathrm{e}}}{\mathrm{vol}} + j_{\mathrm{m1,k}} \cdot \frac{A_{\mathrm{m}}}{\mathrm{vol}}, \tag{2.27}$$

where I have chosen the shaded compartment in Fig 2.6 as my given volume. Here, $d[\mathrm{k}]/dx$ is the extracellular concentration gradient of ion species k, $\overline{[\mathrm{k}]}$ is the average extracellular ion concentration, dV/dx is the extracellular potential gradient, A_{e} is the area of the cross-section between the extracellular

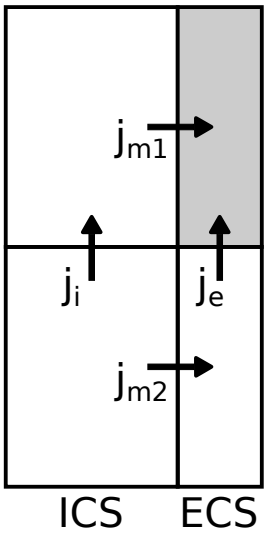

Fig 2.6. Illustration of a one-dimensional neuron. A one-dimensional neuron with two intracellular compartments (left) and two extracellular compartments (right). Ionic movement is driven by the intracellular flux j_{i}, the extracellular flux j_{e}, and the membrane fluxes j_{m1} and j_{m2}. The abbreviations ICS and ECS stand for *intracellular space* and *extracellular space*, respectively.

compartments, vol is the compartment volume, $j_{\mathrm{m1,k}}$ is the membrane flux, and A_{m} is the membrane area.

To solve Eq 2.27, we need to know the potentials V. To overcome this, the KNP framework assumes that all net charge in the intra- and extracellular space is on the membrane, that is, the bulk solution is electroneutral. Under this assumption, we can express the potentials in terms of ion concentrations.

Since the membrane acts as a capacitor, we know that it separates a charge Q_1 on one side of the membrane from an opposite charge $-Q_1$ on the other side of the membrane and the membrane potential is given by:

$$V_{\mathrm{m1}} = \frac{Q_1}{C_{\mathrm{m1}}}. \tag{2.28}$$

Here, C_{m1} is the membrane's capacitance. The assumption of electroneutrality allows us to express Q_1 by summing over all ion concentrations in the shaded compartment and multiply by $F \cdot \mathrm{vol} \cdot z_{\mathrm{k}}$. This gives us:

$$V_{\mathrm{m1}} = (F \cdot \mathrm{vol} \cdot \sum_{\mathrm{k}} z_{\mathrm{k}}[\mathrm{k}])/C_{\mathrm{m1}}. \tag{2.29}$$

Similarly, V_{m2} is given by Q_2/C_{m2}. To find the intra- and extracellular potentials, we require them to ensure charge antisymmetry across the membrane. In Papers I and II, we derive and solve the full set of KNP equations for our specific systems.

2.2 Diffusion of oxygen in brain tissue

The continuity equation (Eq 2.23) also applies to oxygen in brain tissue. Since O_2 does not have charge, the flux is driven by diffusion only, and we get:

$$\frac{\partial [O_2]}{\partial t} = \nabla \cdot (D \nabla [O_2]) + f. \tag{2.30}$$

In this case, f represents the metabolic oxygen consumption, $CMRO_2$. Oxygen can pass through cell membranes, so we do not have to consider tortuosity and volume fractions as we must for ions [54]. However, since O_2 is a gas, its amount is often measured as a partial pressure (pO_2), not a concentration. It may be a bit strange to think about pressure in an aqueous solution. To get a better intuition, imagine a liquid that is in contact with air. Oxygen will move between the two solutions until they are in equilibrium. The concentrations are not the same at this point, as one could think, but the pO_2s are. The O_2 molecules have walked from a place of high pO_2 to a place of lower pO_2. However, there is a simple relationship between pO_2 and the concentration of O_2: $[O_2] = \alpha \cdot pO_2$, where α is the solubility.

If we substitute $[O_2]$ in Eq 2.30 with $\alpha \cdot pO_2$, and f with $-CMRO_2$, we get:

$$\alpha \frac{\partial pO_2}{\partial t} = \nabla \cdot (D \alpha \nabla pO_2) - CMRO_2. \tag{2.31}$$

For a system that has reached steady-state and has a constant $D\alpha$, Eq 2.31 reduces to:

$$\nabla^2 pO_2 = \frac{CMRO_2}{D\alpha}. \tag{2.32}$$

Equations on this form are known as *Poisson equations*. In Paper III, we use Eq 2.32 to derive a method for estimating $CMRO_2$ based on measurements of pO_2.

Chapter 3

Summary of papers

Paper I

An electrodiffusive, ion conserving Pinsky–Rinzel model with homeostatic mechanisms

In Paper I, we present a neuron model with ion concentration dynamics. We call it the *electrodiffusive Pinsky–Rinzel (edPR) model*, and it is, to our knowledge, the first multicompartment neuron model that accounts for ion concentration dynamics in a way that ensures a consistent relationship between ion concentrations, charge, and membrane potentials. We used the Pinsky–Rinzel model [45] as our starting point, equipped it with ion concentration dynamics, and embedded it into the Kirchoff–Nernst–Planck framework (cf. Chapter 2), which efficiently accounts for electrodiffusion on a tissue scale [51]. A motivation for using the previously developed Pinsky–Rinzel model as a baseline was that we could apply it as a "ground truth" when constraining the edPR model. The original Pinsky–Rinzel model is already well-studied and can reproduce various activity patterns seen in real cells. It contains two compartments, which is the minimal number of compartments needed to model electrodiffusion. To include ion concentration dynamics, we added two extra compartments representing the extracellular space of the neuron.

While the key dynamical variable of the original Pinsky–Rinzel model is the membrane potential, the edPR model outputs a variety of parameters, including the ion concentration of all ion species (Na^+, K^+, Cl^-, and Ca^{2+}) in all four compartments, the electric potential in all compartments, the ion pumps' expenditure of ATP, and the electrical conductivity of the intra- and extracellular medium, which is a concentration-dependent parameter describing the medium's ability to transmit ions.

We show that for low to moderate neural activity, the edPR model can fire action potentials for an arbitrarily long time without the ion concentrations changing noteworthy. However, for a too-high firing frequency, the pumps and cotransporters cannot keep up with the activity, and the ion concentrations change significantly. The changes cause the neuron to enter a so-called *depolarization block*, a phenomenon where the neuronal membrane potential gets stuck at a value well above its initial resting state, and the neuron becomes unable to fire new action potentials. Depolarization blocks are often caused by high extracellular K^+ concentrations [55], and this is also what we see in the edPR model. High extracellular K^+ concentrations lead to increased K^+ reversal potentials and explain why the neuron becomes unable to repolarize.

In addition to the depolarization block, we also illustrate the *wave of death*, which is a burst of activity followed by silence and the inability to fire new action

potentials. The wave of death is caused by dysfunctional ion pumps and can, for instance, occur due to a lack of oxygen. We also study the effect of diffusion versus electric drift on the longitudinale movement of ions and the extracellular potentials. We show that neglecting one of them could lead to inaccurate results.

Paper II

An electrodiffusive neuron-extracellular-glia model with somatodendritic interactions

In Paper II, we present a brain tissue model with ion concentration dynamics. The model includes a neuron, neuroglia, and extracellular space. We call it the *electrodiffusive neuron-extracellular-glia (edNEG) model*, and we believe it is the first model of neuro-glial brain tissue to combine multicompartmental neuron modeling with an electrodiffusive framework for intra- and extracellular ion concentration dynamics. The edNEG model is an expansion of the edPR model from Paper I. It includes two important contributors to ion concentration dynamics not accounted for in the first paper: glial cells and cellular swelling.

We show that the neuron can sustain regular activity for low to moderate firing rates and that it goes into depolarization block for too-high firing rates. We also show that with glia present, the neuron can tolerate a higher firing rate without going into depolarization block compared to the neuron without glia since glia works to prevent the extracellular K^+ concentration from increasing too much. We also show that glia reduces cellular swelling.

Paper III

Spatially resolved estimation of metabolic oxygen consumption from optical measurements in cortex

In Paper III, we present a method for estimating spatially resolved maps of metabolic oxygen consumption ($CMRO_2$) based on measurements of oxygen partial pressure (pO_2) in the rat cortex. The method is based on the Poisson equation for the relationship between $CMRO_2$ and pO_2 (cf. Eq 2.32 in Chapter 2). The equation tells us that if we know pO_2 from measurements, we can estimate $CMRO_2/D\alpha$, where D is the diffusion coefficient, and α is the solubility, by applying the Laplace operator, a multivariable second derivative.

Recent developments in two-photon microscopy imaging make it possible to measure pO_2 in tissue with high spatial resolution [43]. However, all experimental measurements come with some kind of error – or *noise* – and two-photon measurements are not an exception. The Laplace operator is highly sensitive to this noise, meaning that just a little noise in the measurements can lead to large errors in the estimated $CMRO_2$.

To reduce the effects of noise, we smooth the data before applying the Laplace operator. The smoothing technique does what the name implies: it

makes data more smooth, that is, it removes sharp changes in the data, changes that are often related to noise. To perform smoothing, we use the `csaps` function from MATLAB'S Curve Fitting Toolbox. Our choice of smoothing method was motivated by a wish to develop an estimation method that is easy to use and based on publically available software. However, the `csaps` function is not flawless. While it removes noise from the data, and consequently much of the error introduced by the Laplace operator, it adds a *bias* around the blood vessel, that is, a systematic error. The bias grows bigger if we increase the amount of smoothing. The challenge then becomes to find an optimal balance between reducing as much noise as possible from the experimental data without introducing too much bias around the vessel.

To test our estimation method, and to study the challenge of bias, we create synthetic pO_2 data with a known $CMRO_2$. We do this by solving the Poisson equation given a known right-hand side, and adding a layer of noise. We study the $CMRO_2$ estimation method for several scenarios: one with a single blood vessel and uniform $CMRO_2$, one with several blood vessels delivering oxygen, and one with a single blood vessel, but with inhomogenous $CMRO_2$ in tissue.

Chapter 4

Discussion

4.1 The interpretation of brain tissue

An ion's journey through brain tissue is filled with obstacles. The extracellular space takes up only ∼20 % of the total brain tissue [52] and contains not only ions but also the extracellular matrix, which is a network of proteins and polysaccharides. Once a modeler does not account for the explicit morphology of brain cells, how they are packed, and all components of the extracellular space, she must assume a spatial average of the obstacles. Two fundamental questions then arise: How should she do this in an efficient, still realistic, way, and how should she interpret her results? In this section, I will not answer these questions, but I want to shed light on a couple of issues to keep in mind when modeling and interpreting brain tissue.

4.1.1 Spatial scales of brain tissue

Ion concentration dynamics: In Papers I and II, any obstacle an ion may run into is accounted for by the tortuosity and volume fractions, representing an average hindrance (cf. Eqs 2.25 and 2.26 in Methods). We can compare this approximation to how we may study water flowing down a valley.

On its way down a valley, water encounters grains of sand and stones of different shapes and sizes, like ions run into cells and molecules in the extracellular fluid. To study the water flow, we are interested in the hydraulic conductivity, that is, the valley's ability to transmit water. If we measure the average conductivity within, let us say a cubic centimeter, the measurement will strongly depend on position. If the volume is placed within a stone, the conductivity is zero. If the volume is filled with water only, water is moving freely. A description of water flow on a centimeter scale would thus require a detailed description of the valley.

To simplify our study of water flow, we can increase the volume we look into, let us say to a cubic meter. This time, the position of our measurement will likely not matter. On this spatial scale, we can consider the valley as a continuous medium with constant conductivity. This would work as an efficient approximation if we, for instance, would like to estimate how much water that flows through the valley during a day, but we could not use it to study the river on a centimeter scale.

Similarly to how we may assume a constant hydraulic conductivity of the valley, we may assume a constant electrical conductivity of brain tissue. In Papers I and II, the electrical conductivity depends on ion concentrations, but we still assume the hindrances to be homogenous. Either way, when we interpret our results, we must be conscious of what spatial scale our approximation is

reasonable. The "rocks and sand" of brain tissue can change dramatically on a micrometer scale [56, 57]. To assume a homogenous electrical conductivity seems justifiable within the cortex [57, 58], while the conductivity is layer-specific within the hippocampus [57, 59].

Oxygen consumption: In Paper III, we estimate oxygen consumption on a spatial grid. From a mathematical perspective, a high density of grid points is warranted as it minimizes discretization errors. However, it is not clear how one should interpret a change in oxygen consumption from one pixel to the next if the pixel size is smaller than the average distance between mitochondria, the sites at which oxygen consumption happens. For the densest grids, a reasonable approach might be to make a spatial average over neighboring pixels covering the average distance between mitochondria.

4.1.2 Temporal scales of brain tissue

Ion concentration dynamics: When using the KNP framework, we assume the bulk solution to be electroneutral (cf. Methods). This assumption is only justifiable on a certain time scale. On a time scale shorter than some tens of nanoseconds, diffusion of ions leads to separation of charge. However, this is soon counteracted by electric drift, and the system settles at a quasi-steady state. The KNP framework assumes that the system reaches quasi-steady-state instantaneously, which is a valid assumption if we model the system on a temporal resolution of microseconds or more [51].

4.2 Comparison to other work

Before ending these introductory chapters, I want to add a short discussion on methods found in the litterature. Although we here present the first multicompartment neuron models to account for electrodiffusion in a biophysically consistent way, mathematical frameworks for constructing such models already exist. Many apply the Poisson–Nernst–Planck (PNP) framework to studies of electrodiffusion and neural processes [3, 60–64]. In this approach, the electrical potential is assumed to follow the Poisson equation for electrostatics. Combined with the Nernst–Planck equation (Eq 2.15 in Methods), it gives a physically correct result at all points in space. However, the PNP equations are very computationally demanding as they require to be solved on a dense spatiotemporal grid at the scale of nanometers and nanoseconds [51]. It has, for this reason, only been used to study parts of a neuron and is not suitable for modeling on a tissue scale [3].

Several frameworks, including the KNP equations used in this thesis, overcome the PNP framework's limitations by assuming the bulk solution to be electroneutral [50, 51, 65–67]. Solbrå et al. [51] showed that the KNP framework gives nearly identical results as the PNP framework on spatiotemporal scales coarser than tens of nanometers and tens of nanoseconds. They derived the KNP

equations in 3-D and used them to study electrodiffusion in the extracellular space. In a different study, Ellingsrud et al. [10] used the KNP framework in 3-D to study ephaptic effects on an axon bundle, though using a Hodgkin–Huxley type axon model without homeostatic mechanisms. Our work in Paper I and Paper II are most comparable to a model presented by Halnes et al. [50], who, like us, derived the KNP equations in 1-D, which allow for more efficient modeling than modeling in 3-D. However, Halnes et al. did not apply the framework to a neuron but to an astrocyte.

When it comes to $CMRO_2$ estimation, most available approaches require measurements of both blood flow and oxygenation and are essentially based on solving a mass balance equation [42]. Sakadžić et al. [42] were the first to suggest a method based on a single quantity only, namely two-photon measurements of pO_2. They related their measurements to $CMRO_2$ through the Poisson equation for oxygen diffusion (Eq 2.32 in Methods) and used it to estimate an assumed constant $CMRO_2$ in the tissue surrounding a single blood vessel. Our work in Paper III can be viewed as an extension of the work presented by Sakadžić et al. From the same starting point, we derive a method for estimating spatial maps of $CMRO_2$. The method allows for heterogeneous oxygen consumption and multiple blood vessels in the tissue.

4.3 Outlook

In each paper of this thesis, we discuss the works' prospects. In short, we envision that the edPR model (Paper I) and the edNEG model (Paper II) will become useful for the field in two main ways. Firstly, as they account for both diffusion and electric drift, the models can be used to explore the effects of electrodiffusion on neurons' electrical properties, as we do in Paper I for some selected cases. Secondly, the models open up for simulating a range of pathological conditions, such as spreading depression and epilepsy. A natural next step for the oxygen consumption estimation method presented in Paper III would be to study alternative smoothing methods to see if it can tolerate higher noise levels. All code used to produce the results in each paper is available on Github (links in papers) and allows for reproducibility as well as easy exploration and development.

Bibliography

[1] Azevedo, F. A. et al. “Equal numbers of neuronal and nonneuronal cells make the human brain an isometrically scaled-up primate brain”. In: *Journal of comparative neurology* vol. 513, no. 5 (2009), pp. 532–541.

[2] Hodgkin, A. L. and Huxley, A. F. “A quantitative description of membrane current and its application to conduction and excitation in nerve”. In: *The Journal of physiology* vol. 117, no. 4 (1952), p. 500.

[3] Solbrå, A. V. “Modeling electrical and diffusive transport in neural tissue”. University of Oslo, 2019.

[4] *Sketch of a brain neuron*. https://commons.wikimedia.org/wiki/File:Sketch_of_a_brain_neuron.png. Accessed: 2020-07-31.

[5] Sterratt, D. et al. *Principles of computational modelling in neuroscience*. Cambridge University Press, 2011.

[6] Ames III, A. “CNS energy metabolism as related to function”. In: *Brain research reviews* vol. 34, no. 1-2 (2000), pp. 42–68.

[7] Wang, D. D. and Bordey, A. “The astrocyte odyssey”. In: *Progress in neurobiology* vol. 86, no. 4 (2008), pp. 342–367.

[8] Kuffler, S. W. and Nicholls, J. G. “The physiology of neuroglial cells”. In: *Ergebnisse der physiologie biologischen chemie und experimentellen pharmakologie*. Springer, 1966, pp. 1–90.

[9] Newman, E. A. “High potassium conductance in astrocyte endfeet”. In: *Science* vol. 233, no. 4762 (1986), pp. 453–454.

[10] Ellingsrud, A. J. et al. “Finite element simulation of ionic electrodiffusion in cellular geometries”. In: *Frontiers in neuroinformatics* vol. 14 (2020), p. 11.

[11] Leão, A. A. P. “Spreading depression of activity in the cerebral cortex”. In: *Journal of neurophysiology* vol. 7, no. 6 (1944), pp. 359–390.

[12] Dreier, J. P. “The role of spreading depression, spreading depolarization and spreading ischemia in neurological disease”. In: *Nature medicine* vol. 17, no. 4 (2011), pp. 439–447.

[13] Somjen, G. G. “Mechanisms of spreading depression and hypoxic spreading depression-like depolarization”. In: *Physiological reviews* vol. 81, no. 3 (2001), pp. 1065–1096.

[14] Ayata, C. and Lauritzen, M. “Spreading depression, spreading depolarizations, and the cerebral vasculature”. In: *Physiological reviews* vol. 95, no. 3 (2015), pp. 953–993.

[15] Iadecola, C. “Neurovascular regulation in the normal brain and in Alzheimer’s disease”. In: *Nature reviews neuroscience* vol. 5, no. 5 (2004), pp. 347–360.

[16] Devor, A. et al. “Neuronal basis of non-invasive functional imaging: from microscopic neurovascular dynamics to BOLD fMRI”. In: *Neural metabolism in vivo*. Springer, 2012, pp. 433–500.

[17] Buxton, R. B. *Introduction to functional magnetic resonance imaging: principles and techniques*. Cambridge university press, 2009.

[18] Barreto, E. and Cressman, J. R. “Ion concentration dynamics as a mechanism for neuronal bursting”. In: *Journal of biological physics* vol. 37, no. 3 (2011), pp. 361–373.

[19] Øyehaug, L. et al. “Dependence of spontaneous neuronal firing and depolarisation block on astroglial membrane transport mechanisms”. In: *Journal of computational neuroscience* vol. 32, no. 1 (2012), pp. 147–165.

[20] Somjen, G., Kager, H., and Wadman, W. “Computer simulations of neuron-glia interactions mediated by ion flux”. In: *Journal of computational neuroscience* vol. 25, no. 2 (2008), pp. 349–365.

[21] Florence, G. et al. “The role of extracellular potassium dynamics in the different stages of ictal bursting and spreading depression: a computational study”. In: *Journal of theoretical biology* vol. 258, no. 2 (2009), pp. 219–28.

[22] Cressman, J. R. et al. “The influence of sodium and potassium dynamics on excitability, seizures, and the stability of persistent states: I. Single neuron dynamics”. In: *Journal of computational neuroscience* vol. 26, no. 2 (2009), pp. 159–170.

[23] Ullah, G. et al. “The influence of sodium and potassium dynamics on excitability, seizures, and the stability of persistent states: II. Network and glial dynamics”. In: *Journal of computational neuroscience* vol. 26, no. 2 (2009), pp. 171–183.

[24] Lee, J. and Kim, S. J. “Spectrum measurement of fast optical signal of neural activity in brain tissue and its theoretical origin”. In: *Neuroimage* vol. 51, no. 2 (2010), pp. 713–722.

[25] Lee, J., Boas, D. A., and Kim, S. J. “Multiphysics neuron model for cellular volume dynamics”. In: *IEEE Transactions on biomedical engineering* vol. 58, no. 10 (2011), pp. 3000–3003.

[26] Zandt, B.-J. et al. “Neural dynamics during anoxia and the “wave of death””. In: *PLoS one* vol. 6, no. 7 (2011), e22127.

[27] Hübel, N., Schöll, E., and Dahlem, M. A. “Bistable dynamics underlying excitability of ion homeostasis in neuron models”. In: *PLoS computational biology* vol. 10, no. 5 (2014), e1003551.

[28] Dahlem, M. A., Schumacher, J., and Hübel, N. “Linking a genetic defect in migraine to spreading depression in a computational model”. In: *PeerJ* vol. 2 (2014), e379.

[29] Hübel, N. and Dahlem, M. A. "Dynamics from seconds to hours in Hodgkin-Huxley model with time-dependent ion concentrations and buffer reservoirs". In: *PLoS computational biology* vol. 10, no. 12 (2014), e1003941.

[30] Wei, Y. et al. "Oxygen and seizure dynamics: II. Computational modeling". In: *Journal of neurophysiology* vol. 112, no. 2 (2014), pp. 213–223.

[31] Wei, Y., Ullah, G., and Schiff, S. J. "Unification of neuronal spikes, seizures, and spreading depression". In: *Journal of neuroscience* vol. 34, no. 35 (2014), pp. 11733–11743.

[32] Hübel, N. et al. "The role of glutamate in neuronal ion homeostasis: A case study of spreading depolarization". In: *PLoS computational biology* vol. 13, no. 10 (2017), e1005804.

[33] Kager, H., Wadman, W. J., and Somjen, G. G. "Simulated seizures and spreading depression in a neuron model incorporating interstitial space and ion concentrations". In: *Journal of neurophysiology* vol. 84, no. 1 (2000), pp. 495–512.

[34] Kager, H., Wadman, W., and Somjen, G. "Conditions for the triggering of spreading depression studied with computer simulations". In: *Journal of neurophysiology* vol. 88, no. 5 (2002), pp. 2700–2712.

[35] Kager, H., Wadman, W., and Somjen, G. "Seizure-like afterdischarges simulated in a model neuron". In: *Journal of computational neuroscience* vol. 22, no. 2 (2007), pp. 105–128.

[36] Cataldo, E. et al. "Computational model of touch sensory cells (T Cells) of the leech: role of the afterhyperpolarization (AHP) in activity-dependent conduction failure". In: *Journal of computational neuroscience* vol. 18, no. 1 (2005), pp. 5–24.

[37] Forrest, M. D. et al. "The sodium-potassium pump controls the intrinsic firing of the cerebellar Purkinje neuron". In: *PLoS one* vol. 7, no. 12 (2012), e51169.

[38] Le Masson, G., Przedborski, S., and Abbott, L. "A computational model of motor neuron degeneration". In: *Neuron* vol. 83, no. 4 (2014), pp. 975–988.

[39] Forrest, M. D. "Simulation of alcohol action upon a detailed Purkinje neuron model and a simpler surrogate model that runs $>$ 400 times faster". In: *BMC neuroscience* vol. 16, no. 1 (2015), p. 27.

[40] Zylbertal, A. et al. "Prolonged intracellular Na^+ dynamics govern electrical activity in accessory olfactory bulb mitral cells". In: *PLoS biology* vol. 13, no. 12 (2015), e1002319.

[41] Zylbertal, A., Yarom, Y., and Wagner, S. "The slow dynamics of intracellular sodium concentration increase the time window of neuronal integration: A simulation study". In: *Frontiers in computational neuroscience* vol. 11 (2017), p. 85.

[42] Sakadžić, S. et al. “Two-photon microscopy measurement of cerebral metabolic rate of oxygen using periarteriolar oxygen concentration gradients”. In: *Neurophotonics* vol. 3, no. 4 (2016), p. 045005.

[43] Sakadžić, S. et al. “Two-photon high-resolution measurement of partial pressure of oxygen in cerebral vasculature and tissue”. In: *Nature methods* vol. 7, no. 9 (2010), p. 755.

[44] Krogh, A. “The number and distribution of capillaries in muscles with calculations of the oxygen pressure head necessary for supplying the tissue”. In: *The Journal of physiology* vol. 52, no. 6 (1919), pp. 409–415.

[45] Pinsky, P. F. and Rinzel, J. “Intrinsic and network rhythmogenesis in a reduced Traub model for CA3 neurons”. In: *Journal of computational neuroscience* vol. 1, no. 1-2 (1994), pp. 39–60.

[46] Traub, R. D. et al. “A model of a CA3 hippocampal pyramidal neuron incorporating voltage-clamp data on intrinsic conductances”. In: *Journal of neurophysiology* vol. 66, no. 2 (1991), pp. 635–650.

[47] Tennøe, S. “Uncertainty quantification in neuroscience”. University of Oslo, 2019.

[48] Helton, T. D. et al. “Diversity of dendritic morphology and entorhinal cortex synaptic effectiveness in mouse CA2 pyramidal neurons”. In: *Hippocampus* vol. 29, no. 2 (2019), pp. 78–92.

[49] *Errata, Principles of computational modelling in neuroscience*. http://www.compneuroprinciples.org/errata. Accessed: 2020-01-04.

[50] Halnes, G. et al. “Electrodiffusive model for astrocytic and neuronal ion concentration dynamics”. In: *PLoS computational biology* vol. 9, no. 12 (2013), e1003386.

[51] Solbrå, A. et al. “A Kirchhoff-Nernst-Planck framework for modeling large scale extracellular electrodiffusion surrounding morphologically detailed neurons”. In: *PLoS computational biology* vol. 14, no. 10 (2018), e1006510.

[52] Chen, K. C. and Nicholson, C. “Spatial buffering of potassium ions in brain extracellular space”. In: *Biophysical journal* vol. 78, no. 6 (2000), pp. 2776–2797.

[53] Nicholson, C. and Phillips, J. “Ion diffusion modified by tortuosity and volume fraction in the extracellular microenvironment of the rat cerebellum.” In: *The Journal of physiology* vol. 321, no. 1 (1981), pp. 225–257.

[54] Nicholson, C. “Diffusion and related transport mechanisms in brain tissue”. In: *Reports on progress in physics* vol. 64, no. 7 (2001), p. 815.

[55] “Depolarization Block”. In: *Encyclopedia of Neuroscience*. Ed. by Binder, M. D., Hirokawa, N., and Windhorst, U. Springer Berlin Heidelberg, 2009, pp. 943–944.

[56] Nicholson, C. and Syková, E. “Extracellular space structure revealed by diffusion analysis”. In: *Trends in neurosciences* vol. 21, no. 5 (1998), pp. 207–215.

[57] Ness, T. V. et al. “Computing extracellular electric potentials from neuronal simulations”. In: *arXiv preprint arXiv:2006.16630* (2020).

[58] Logothetis, N. K., Kayser, C., and Oeltermann, A. “In vivo measurement of cortical impedance spectrum in monkeys: implications for signal propagation”. In: *Neuron* vol. 55, no. 5 (2007), pp. 809–823.

[59] López-Aguado, L., Ibarz, J., and Herreras, O. “Activity-dependent changes of tissue resistivity in the CA1 region in vivo are layer-specific: modulation of evoked potentials”. In: *Neuroscience* vol. 108, no. 2 (2001), pp. 249–262.

[60] Pods, J., Schönke, J., and Bastian, P. “Electrodiffusion models of neurons and extracellular space using the Poisson–Nernst–Planck equations—numerical simulation of the intra- and extracellular potential for an axon model”. In: *Biophysical journal* vol. 105, no. 1 (2013), pp. 242–254.

[61] Lopreore, C. L. et al. “Computational modeling of three-dimensional electrodiffusion in biological systems: application to the node of Ranvier”. In: *Biophysical journal* vol. 95, no. 6 (2008), pp. 2624–2635.

[62] Cartailler, J., Schuss, Z., and Holcman, D. “Analysis of the Poisson–Nernst–Planck equation in a ball for modeling the Voltage–Current relation in neurobiological microdomains”. In: *Physica D: Nonlinear phenomena* vol. 339 (2017), pp. 39–48.

[63] Cartailler, J., Schuss, Z., and Holcman, D. “Electrostatics of non-neutral biological microdomains”. In: *Scientific reports* vol. 7, no. 1 (2017), pp. 1–7.

[64] Lagache, T., Jayant, K., and Yuste, R. “Electrodiffusion models of synaptic potentials in dendritic spines”. In: *Journal of computational neuroscience* vol. 47, no. 1 (2019), pp. 77–89.

[65] Pods, J. “A comparison of computational models for the extracellular potential of neurons”. In: *Journal of integrative neuroscience* vol. 16, no. 1 (2017), pp. 19–32.

[66] Mori, Y. and Peskin, C. “A numerical method for cellular electrophysiology based on the electrodiffusion equations with internal boundary conditions at membranes”. In: *Communications in applied mathematics and computational science* vol. 4, no. 1 (2009), pp. 85–134.

[67] Mori, Y., Liu, C., and Eisenberg, R. S. “A model of electrodiffusion and osmotic water flow and its energetic structure”. In: *Physica D: Nonlinear phenomena* vol. 240, no. 22 (2011), pp. 1835–1852.

Papers

Paper I

An electrodiffusive, ion conserving Pinsky–Rinzel model with homeostatic mechanisms

Marte J. Sætra[1,2], Gaute T. Einevoll[1,2,3], Geir Halnes[1,3,*]

1 Centre for Integrative Neuroplasticity, University of Oslo, Oslo, Norway
2 Department of Physics, University of Oslo, Oslo, Norway
3 Faculty of Science and Technolgy, Norwegian University of Life Sciences, Ås, Norway

Published in *PLoS Computational Biology* vol. 16, no. 4 (2020), e1007661. https://doi.org/10.1371/journal.pcbi.1007661

Abstract

In most neuronal models, ion concentrations are assumed to be constant, and effects of concentration variations on ionic reversal potentials, or of ionic diffusion on electrical potentials are not accounted for. Here, we present the electrodiffusive Pinsky–Rinzel (edPR) model, which we believe is the first multicompartmental neuron model that accounts for electrodiffusive ion concentration dynamics in a way that ensures a biophysically consistent relationship between ion concentrations, electrical charge, and electrical potentials in both the intra- and extracellular space. The edPR model is an expanded version of the two-compartment Pinsky–Rinzel (PR) model of a hippocampal CA3 neuron. Unlike the PR model, the edPR model includes homeostatic mechanisms and ion-specific leakage currents, and keeps track of all ion concentrations (Na^+, K^+, Ca^{2+}, and Cl^-), electrical potentials, and electrical conductivities in the intra- and extracellular space. The edPR model reproduces the membrane potential dynamics of the PR model for moderate firing activity. For higher activity levels, or when homeostatic mechanisms are impaired, the homeostatic mechanisms fail in maintaining ion concentrations close to baseline, and the edPR model diverges from the PR model as it accounts for effects of concentration changes on neuronal firing. We envision that the edPR model will be useful for the field in three main ways. Firstly, as it relaxes commonly made modeling assumptions, the edPR model can be used to test the validity of these assumptions under various firing conditions,

* geir.halnes@nmbu.no

as we show here for a few selected cases. Secondly, the edPR model should supplement the PR model when simulating scenarios where ion concentrations are expected to vary over time. Thirdly, being applicable to conditions with failed homeostasis, the edPR model opens up for simulating a range of pathological conditions, such as spreading depression or epilepsy.

Author summary

Neurons generate their electrical signals by letting ions pass through their membranes. Despite this fact, most models of neurons apply the simplifying assumption that ion concentrations remain effectively constant during neural activity. This assumption is often quite good, as neurons contain a set of homeostatic mechanisms that make sure that ion concentrations vary quite little under normal circumstances. However, under some conditions, these mechanisms can fail, and ion concentrations can vary quite dramatically. Standard models are thus not able to simulate such conditions. Here, we present what to our knowledge is the first multicompartmental neuron model that accounts for ion concentration variations in a way that ensures complete and consistent ion concentration and charge conservation. In this work, we use the model to explore under which activity conditions the ion concentration variations become important for predicting the neurodynamics. We expect the model to be of great value for the field of neuroscience, as it can be used to simulate a range of pathological conditions, such as spreading depression or epilepsy, which are associated with large changes in extracellular ion concentrations.

Introduction

The neuronal action potential (AP) is generated by a transmembrane influx of Na^+, which depolarizes the neuron, followed by an efflux of K^+, which repolarizes it. Likewise, all neurodynamics is fundamentally about the movement of ions, which are the charge carriers in the brain. Therefore, it might seem peculiar that most models of neuronal activity are based on the approximation that the concentrations of the main charge carriers (Na^+, K^+, and Cl^-) do not change over time. This approximation is, for example, incorporated in the celebrated Hodgkin–Huxley model [1], and a large number of later models based on a Hodgkin–Huxley type formalism (see, e.g., [2–7]).

Setting the ion concentrations to not change over time is often a fairly good approximation. The reason is that the number of ions that need to cross the membrane to charge up the neuron by, say, an AP worth of millivolts, is too small to have any notable impact on ion concentrations on either side of the membrane (see, e.g., Box 2.2 in [8]), meaning that concentration changes on a short time scale can be neglected. On a longer time-scale, the ionic exchange due to APs (or other neuronal events), is normally reversed by a set of homeostatic mechanisms such as ion pumps and cotransporters, which work to maintain constant baseline concentrations. In Hodgkin–Huxley type models, the large number of ion pumps,

cotransporters and passive ionic leakages that strive towards maintaining baseline conditions are therefore not explicitly modeled. Instead, they are simply assumed to do their job and are grouped into a single *passive* and non-specific leakage current $I_{\text{leak}} = g_{\text{leak}}(\phi_{\text{m}} - E_{\text{leak}})$, which determines the cell's resting potential (for a critical study of this approximation, see [9]).

Another approximation commonly applied by modelers of neurons is that the extracellular potential is constant and grounded ($\phi_{\text{e}} = 0$) so that the only voltage variable that one needs to worry about when simulating neurodynamics is the transmembrane potential (ϕ_{m}). This assumption is implicit in the majority of morphologically explicit models of neurons, where the (spatial) signal propagation in dendrites and axons are computed using the cable equation (see, e.g., [10–12]). Cable-equation based, multicompartmental neuronal models are widely used within the field of neuroscience, both for understanding dendritic integration and neuronal response properties at the single neuron level (see, e.g., [3, 4, 6, 7]) and for exploring the dynamics of large neuronal networks (see e.g., [13–15]). They are even used in the context of performing forward modeling of extracellular potentials, such as local field potentials (LFP), the electrocorticogram (ECoG), and electroencephalogram (EEG) (see, e.g., [16–18]), despite the evident inconsistency involved when first computing neurodynamics under the approximation that $\phi_{\text{e}} = 0$ (Fig 1A), and then in the next step using this dynamics to predict a nonzero ϕ_{e} (Fig 1B). The approximation is nevertheless useful since ϕ_{e} is typically so much smaller than ϕ_{m} that the (ephaptic) effect of ϕ_{e} on neurodynamics can be neglected without severe loss in accuracy [19].

There are, however, scenarios where the assumptions of constant ion concentrations and a grounded extracellular space are not justifiable. Notably, large-scale extracellular ion concentration changes are a trademark of several pathological conditions, including epilepsy and spreading depression [22–25]. In these cases, neurons are unable to maintain their baseline conditions because they for various reasons are too active and/or their homeostatic mechanisms are too slow. During spreading depression, the extracellular K^+ concentration can change from a baseline value of about 3-5 mM to pathological levels of several tens of mM, and the increased K^+ concentration tends to coincide with a slow, direct-current (DC) like drop in the extracellular potential, which may be several tens of millivolts in amplitude [25, 26], and can give rise to large spatial gradients. For example, one experiment saw the extracellular K^+-concentration and ϕ_{e} vary by as much as 30 mM and 20 mV, respectively, over the hippocampal depth [26]. Such dramatic gradients in the extracellular environment are likely to have a strong impact on the dynamical properties of neurons, both through the concentration-dependent changes in ion-channel reversal potentials [27–29] and putatively through a direct ephaptic effect from ϕ_{e} on the membrane potential.

The construction of accurate neuron models that include ion concentration dynamics (and conservation) poses two key challenges. Firstly, ion conserving models need a finely adjusted balance between the homeostatic machinery and all passive and active ion-specific currents so that all ion concentrations, as well as voltages, vary in a biophysically realistic way over time when the neuron is active. Secondly, in spatially extended models, ions will not move only across

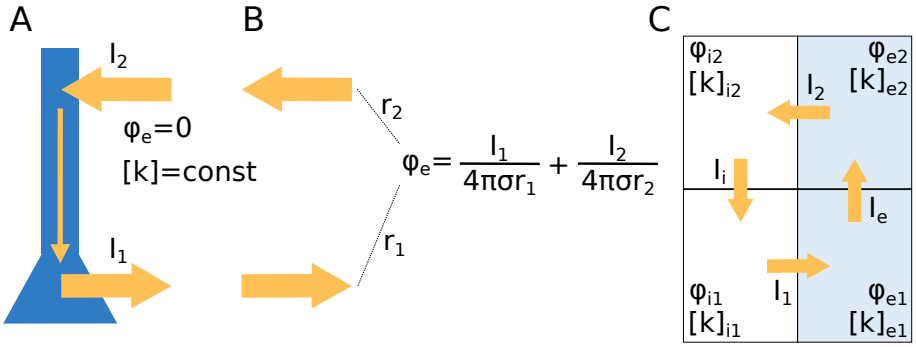

Fig 1. Modeling intra- and extracellular dynamics: standard theory vs. unified framework. (A) The dynamics of the membrane potential (ϕ_m) and transmembrane currents of neurons are typically modeled using cable theory. It is then assumed that the extracellular environment is grounded ($\phi_e = 0$). Typically, it is also assumed that ion concentrations both in the intra- and extracellular space are constant, so that also ionic reversal potentials remain constant. **(B)** When knowing the transmembrane neuronal currents (as computed in **(A)**), standard volume conductor theory [20, 21] allows us to estimate the extracellular potential, which is computed as the sum of neuronal point-current sources weighted by their distance to the recording location. An underlying assumption is that fluctuations in ϕ_e (as computed in **(B)**) are so small that they have no effect on the neurodynamics (as computed in **(A)**), i.e., there is no ephaptic coupling. Another underlying assumption (cf. constant ion concentrations) is that extracellular diffusive currents do not affect electrical potentials. **(C)** We propose a unified, electrodiffusive framework for intra- and extracellular ion concentration and voltage dynamics, assuring a consistent relationship between ion concentrations, electrical charge, and electrical potential in all compartments.

membranes, but also within the extracellular and intracellular space. Such ionic movement may be propelled both by diffusion and electrical drift. Ionic diffusion can, in principle, affect the electrical potential (since ions carry charge), and the electrical potential can, in principle, affect ion concentration dynamics (since ions drift along potential gradients) [30–32]. Accurate modeling of such systems thus requires a unified, electrodiffusive framework that ensures a physically consistent relationship between ion concentrations, charge density, and electrical potentials.

Intra- or extracellular electrodiffusion is not an issue in single-compartment models, of which there are quite a few that incorporate ion concentration dynamics in a more or less consistent way [28, 29, 33–47]. Single compartment models are useful in many aspects. However, in order to represent morphological features of neurons, such as e.g., differential expression of ion channels in the soma versus dendrites, or account for transport processes in the space inside or outside neurons, one needs models with more than a single compartment. Among the several morphologically explicit models that have included homeostatic

machinery and explicitly simulated ion concentration dynamics (see e.g., [27, 48–57]), neither have accounted for the electrodiffusive coupling between the movement of ions and electrical potentials (see Results section titled Loss in accuracy when neglecting electrodiffusive effects on concentration dynamics). Hence, to our knowledge, no morphologically explicit neuron model has so far been developed that ensures biophysically consistent dynamics in ion concentrations and electrical potentials during long-time activity, although useful mathematical framework for constructing such models are available [58–62].

The goal of this work is to propose what we may refer to as "a minimal neuronal model that has it all". By "has it all", we mean that it (1) has a spatial extension, (2) considers both extracellular- and intracellular dynamics, (3) keeps track of all ion concentrations (Na^+, K^+, Ca^{2+}, and Cl^-) in all compartments, (4) keeps track of all electrical potentials (ϕ_m, ϕ_e, and ϕ_i - the latter being the intracellular potential) in all compartments, (5) has differential expression of ion channels in soma versus dendrites, and can fire somatic APs and dendritic calcium spikes, (6) contains the homeostatic machinery that ensures that it maintains a realistic dynamics in ϕ_m and all ion concentrations during long-time activity, and (7) accounts for transmembrane, intracellular and extracellular ionic movements due to both diffusion and electrical migration, and thus ensures a consistent relationship between ion concentrations and electrical charge. Being based on a unified framework for intra- and extracellular dynamics (Fig 1C), the model thus accounts for possible ephaptic effects from extracellular dynamics, as neglected in standard feedforward models based on volume conductor theory (Fig 1A-B). By "minimal" we simply mean that we reduce the number of spatial compartments to the minimal, which in this case is four, i.e., two neuronal compartments (a soma and a dendrite), plus two extracellular compartments (outside soma and outside dendrite). Technically, the model was constructed by adding homeostatic mechanisms and ion concentration dynamics to an existing model, i.e., the two-compartment Pinsky–Rinzel (PR) model [3], and embedding in it a consistent electrodiffusive framework, i.e., the previously developed Kirchhoff-Nernst-Planck framework [31, 32, 60, 62]. For the remainder of this paper, we refer to our model as the electrodiffusive Pinsky–Rinzel (edPR) model.

The remainder of this article is organized as follows. First, we present the edPR model and illustrate the numerous variables that it can simulate. Next, we show that the edPR model can reproduce the firing properties of the original PR model. By running long-time simulations (several minutes of biological time) on both models, we identify the firing conditions under which the two models maintained a similar firing pattern, and under which conditions concentration effects became important so that dynamics of the edPR model diverged from the original PR model over time. Finally, we use the edPR model to explore the validity of some important assumptions commonly made in the field of computational neuroscience, regarding the decoupling of electrical and diffusive signals. We believe that the edPR model will be of great value for the field of neuroscience, partly because it gives a deepened insight into the balance between neuronal firing and ion homeostasis, partly because it lends itself to explore under which conditions the common modeling assumption of constant

ion concentrations is warranted, and most importantly because it opens for more detailed mechanistic studies of pathological conditions associated with large changes in ion concentrations, such as epilepsy and spreading depression [22–25].

Results

An electrodiffusive Pinsky–Rinzel model

The here proposed electrodiffusive Pinsky–Rinzel (edPR) model is inspired by the original Pinsky–Rinzel (PR) model [3], which is a two-compartment (soma + dendrite) version of a CA3 hippocampal cell model, initially developed by Traub et al. [2]. In the original PR model, the somatic compartment contains Na^+, and K^+ delayed rectifier currents (I_{Na} and I_{K-DR}), while the dendritic compartment contains a voltage-dependent Ca^{2+} current (I_{Ca}), a voltage-dependent K^+ afterhyperpolarization current (I_{K-AHP}), and a Ca^{2+}-dependent K^+ current (I_{K-C}). In addition, both compartments contain passive leakage currents. Despite its small number of compartments and conductances, the PR model can reproduce a variety of realistic firing patterns when responding to somatic or dendritic stimuli, including somatic APs and dendritic calcium spikes.

In the edPR model, we have adopted all mechanisms from the original PR model. In addition, we have (i) made all ion channels and passive leakage currents ion-specific, (ii) included $3Na^+/2K^+$ pumps (I_{pump}), K^+/Cl^- cotransporters (I_{KCC2}), $Na^+/K^+/2Cl^-$ cotransporters (I_{NKCC1}), and a $Ca^{2+}/2Na^+$ exchangers (I_{Ca-dec}), and (iii) included two extracellular compartments (outside soma + outside dendrite). To compute the dynamics of the edPR, we used an electrodiffusive KNP-framework for consistently computing the voltage- and ion concentration dynamics in the intra- and extracellular compartments [60]. The model is summarized in Fig 2 and described in details in the Methods section.

Key dynamical variables in the electrodiffusive Pinsky–Rinzel model

While the key variable in the original PR model is the membrane potential ϕ_m, the edPR model allows us to compute a multitude of variables relevant to neurodynamics. The functionality of the edPR model is illustrated in Fig 3, which shows a 60 s simulation where the model fires at 1 Hz for 10 s. We have plotted a selection of output variables, including the membrane potential (Fig 3A-B), extracellular potentials (Fig 3C-D), the dynamics of all ion concentrations in all compartments (Fig 3E-H), concentration effects on ionic reversal potentials (Fig 3I-J), concentration effects on the electrical conductivity of the intra- and extracellular medium (Fig 3K), and ATP consumption (Fig 3L) of the $3Na^+/2K^+$ pumps and $Ca^{2+}/2Na^+$ exchangers.

Unlike neuronal models based on cable theory, where ϕ_e is assumed to be zero so that $\phi_m = \phi_i$, the edPR model computes ϕ_m, ϕ_i, and ϕ_e from a consistent framework where ephaptic effects from ϕ_e on ϕ_m are accounted for (Fig 3C).

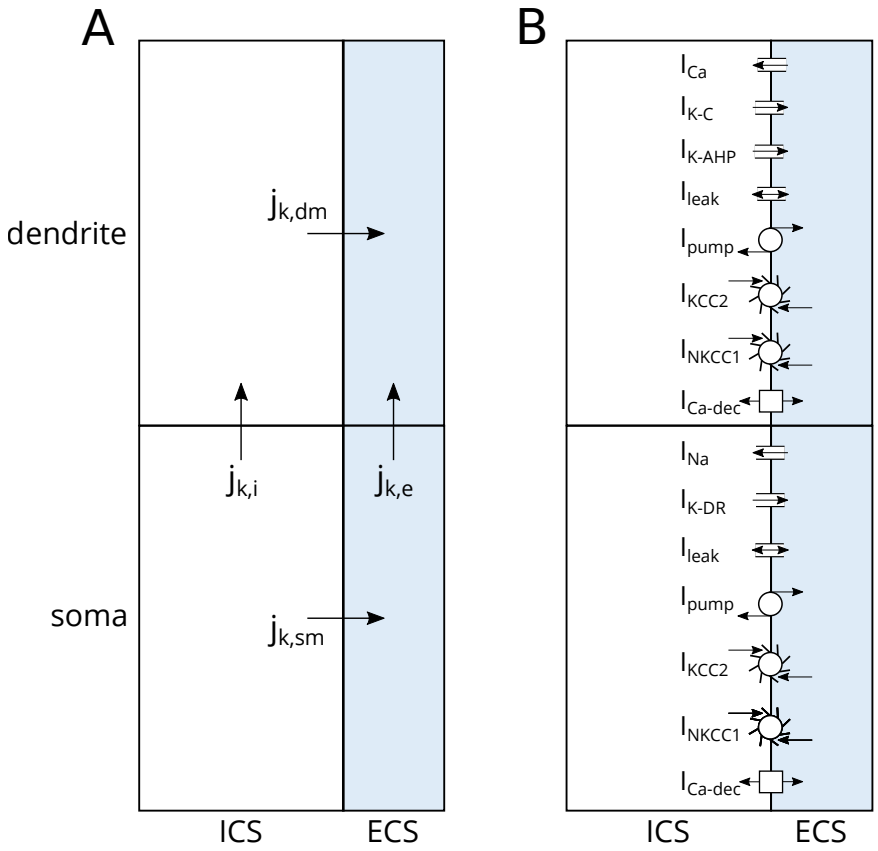

Fig 2. edPR model architecture. (A) Two plus two compartments (soma + dendrite), with intracellular space to the left and extracellular space to the right. Two kinds of fluxes of different ion species k are involved: transmembrane fluxes ($j_{\mathrm{k,dm}}$, $j_{\mathrm{k,sm}}$) and intra- and extracellular fluxes ($j_{\mathrm{k,i}}$, $j_{\mathrm{k,e}}$). The dynamics of the potential ϕ and ion concentration dynamics in all compartments were computed using an electrodiffusive framework, ensuring bulk electroneutrality and a consistent relationship between ion concentrations, electrical charge, and voltages. **(B)** Active currents were taken from the original PR model [3]. In the soma, these consisted of Na^+ and K^+ delayed rectifier currents (I_{Na} and $I_{K\text{-}DR}$). In the dendrite, these consisted of a voltage-dependent Ca^{2+} current (I_{Ca}), a Ca^{2+}-dependent K^+ current ($I_{K\text{-}C}$), and a voltage-dependent K^+ afterhyperpolarization current ($I_{K\text{-}AHP}$). Ion specific passive (leakage-) currents and homeostatic mechanisms were taken from a previous model by Wei et al. [45], and were identical in the soma and dendrite. These included Na^+, K^+ and Cl^- leak currents, a $3Na^+/2K^+$ pump (I_{pump}), a K^+/Cl^- cotransporter (I_{KCC2}), and a $Na^+/K^+/2Cl^-$ cotransporter (I_{NKCC1}). In addition, the soma and dendrite included a $Ca^{2+}/2Na^+$ exchanger ($I_{Ca\text{-}dec}$), providing an intracellular Ca^{2+} decay similar to that in the PR model.

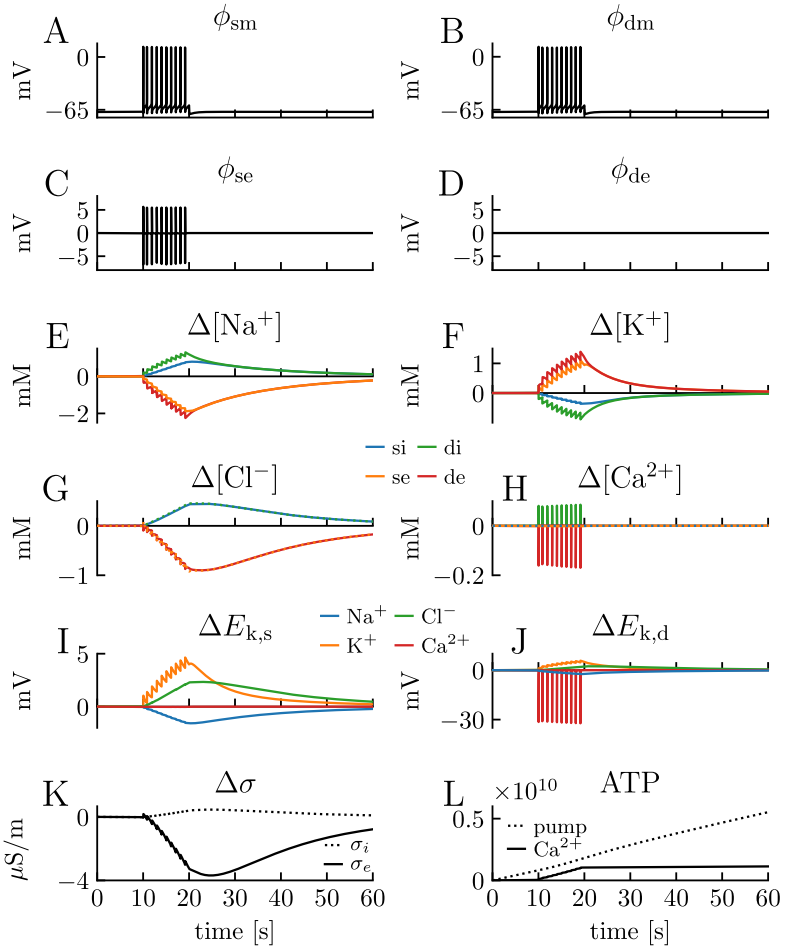

Fig 3. Output of the edPR model. A 27 pA step-current injection was applied to the somatic compartment between $t = 10$ s and $t = 20$ s, and the model responded with a firing rate of 1 Hz. **(A-B)** The membrane potential ϕ_m of the soma and the dendrite, respectively. **(C-D)** The extracellular (index e) potential ϕ_e of the soma (index s) and the dendrite (index d), respectively. The dendritic extracellular compartment was chosen as the reference point when calculating potentials, so ϕ_{de} was zero by definition. Since amplitudes in ϕ_m were so much larger than for ϕ_e, intracellular (index i) potentials ($\phi_i = \phi_e + \phi_m$) were similar to ϕ_m, and therefore not shown. **(E-F)** Ion concentrations dynamics of all ion species k (Na^+, Cl^-, K^+, Ca^{2+}) in all four compartments shown in terms of their deviance from baseline concentrations. **(I-J)** Changes in reversal potentials for all ion species in the soma and the dendrite, respectively. **(K)** Change in conductivity of the intra- and extracellular media (σ_i and σ_e, respectively). **(L)** Accumulative number of ATP molecules consumed by the $3Na^+/2K^+$ pumps and $Ca^{2+}/2Na^+$ exchangers.

Due to the electrical coupling between the soma and dendrite, the fluctuations in ϕ_m were similar in these compartments, and a more detailed analysis of the AP shapes is found further below. While an action potential essentially gave a depolarization followed by a repolarization of ϕ_m, its extracellular signature was essentially a voltage drop (to about -5 mV) followed by a voltage increase (to about +5 mV). This biphasic response of the extracellular AP signature has been seen in several studies (for an analysis, see [20, 21]). In experimental recordings, amplitudes in ϕ_e fluctuations are typically on the order of 100 μV, which is much smaller than that predicted by the edPR model. The discrepancy is an artifact that is mainly due to the 1D approximation in the edPR model (see Discussion). The dendritic extracellular potential (Fig 3D) was by definition zero at all times, as this compartment was used as the reference point for the potential.

The effect of neuronal firing on the ion concentration dynamics is illustrated in Fig 3E-H. Before the stimulus onset, the cell was resting at approximately -68 mV, and ion concentrations remained at baseline values. During AP firing, the ion concentrations varied in a jigsaw-like fashion in all compartments, except for Ca^{2+}, which returned to baseline between each AP and showed notable variation only inside/outside the dendrite since the soma contained no Ca^{2+} channels. As the extracellular volume was set to be half as big as the intracellular volume, changes in extracellular ion concentrations were about twice as big as the changes in intracellular ion concentrations. The jigsaw pattern was most pronounced for the K^+ and Na^+ concentrations, as these were the main mediators of the APs (Fig 3E-H). The pattern reflects a cycle of (i) incremental steps away from baseline concentrations, which were mediated by the complex of mechanisms active during the APs, followed by (ii) slower decays back towards baseline, which were mediated by pumps and cotransporters working between the APs. In this simulation, the decay was incomplete, so that concentrations reached gradually larger peak values by each consecutive AP. However, as we show later (see Section titled The edPR model predicts homeostatic failure due to high firing rate), the concentrations did, in this case, approach a firing-frequency dependent steady state.

When the firing ceased in Fig 3, the pumps and cotransporters could work uninterruptedly to re-establish the baseline ion concentrations. The resting membrane potential of about -68 mV, was recovered quite rapidly (ms timescale). After this, the slower recovery process of the ion concentration was due to an electroneutral exchange of ions between the neuron and the extracellular space. A full recovery of the baseline concentrations took on the order of 80 s (confirmed by running a longer simulation than the one shown in Fig 3).

As ion concentrations varied during the simulation, so did the ionic reversal potentials, E_k(Fig 3I-J). The by far largest change was seen for the Ca^{2+} reversal potential in the dendrite ($E_{k,d}$), which dropped by as much as -30 mV during an AP, (i.e., from a baseline value of 124 mV to 94 mV). The explanation is that the basal intracellular Ca^{2+}-concentration is extremely low (100 nM) compared to the concentrations of other ion species (several mM), and therefore experienced a much larger relative change during the simulation. Among the main charge carriers (Na^+, Cl^-, K^+), the lowest concentration is found for K^+

in the extracellular space (Table 5 in Methods). For that reason, the second largest change in reversal potential was found for E_{K}, which increased by about 5 mV (i.e., from a basal value of -84 mV to -79 mV) in both the soma and dendrite. The changes in E_{Ca} and E_{K} had a relatively minor impact on the firing pattern in the shown simulations, as the relative change in the driving force $\phi_{\mathrm{m}} - E_{\mathrm{k}}$ was not that severe.

The conductivities (σ) of the intra- and extracellular bulk solutions depend on the availability of free charge carriers, and are in the edPR model functions of the ion concentrations and their mobility (cf. Eq 19). The changes in σ were minimal during the conditions simulated here (Fig 3K), i.e., σ varied by a few μS/m over the course of the simulation, while the basal levels were approximately 0.11 S/m and 0.59 S/m for the intra- and extracellular solutions, respectively.

Finally, the $3Na^+/2K^+$ pump and $Ca^{2+}/2Na^+$ exchanger use energy in the form of ATP to move ions against their gradients. The $3Na^+/2K^+$ pump exchanges 3 Na^+ ions for 2 K^+ ions, and consumes one ATP per cycle [63], while we assumed that the $Ca^{2+}/2Na^+$ exchanger consumed 1 ATP per cycle (i.e., per Ca^{2+} exchanged, as in [64]). As the edPR model explicitly models these processes, we could compute the ATP (energy) consumption of the pumps during the simulation. Fig 3L shows the accumulative number of ATP consumed from the onset of the simulation. The $3Na^+/2K^+$ pump was constantly active, as it combated leakage currents and worked to maintain the baseline concentration even before stimulus onset. Before stimulus onset, it consumed ATP at a constant rate (linear curve), which increased only slightly at $t = 10$ s when the neuron started to fire (small dent in the curve). As the neuron did not contain any passive leakage of Ca^{2+}, the $Ca^{2+}/2Na^+$ exchangers were only active while the neuron was firing. During firing, the $Ca^{2+}/2Na^+$ exchanger combated the Ca^{2+} entering through the dendritic Ca^{2+} channels, and then consumed approximately the same amount of energy as the $3Na^+/2K^+$ pump (parallel curves). A high metabolic cost of dendritic Ca^{2+} spikes has previously been reported also in cortical layer 5 pyramidal neurons [64].

We note that the edPR model had a stable resting state before stimulus onset and that it returned to this resting state after the stimulus had been turned off. In this resting state, ion concentrations remained constant, and ϕ_{m} was approximately -68 mV. This resting equilibrium was due to a balance between the ion-specific leakage channels, pumps, and cotransporters, which we adopted from previous studies (see Methods). However, the existence of a homeostatic equilibrium was not highly sensitive to the choice of model parameters. As we confirmed through a sensitivity analysis, varying membrane parameters (one by one) with ±15% of their default values did not abolish the existence of a stable resting state, but shifted the resting potential by maximally ±3 mV (Fig 4A) and the resting concentrations by maximally 5% (Fig 4B-E).

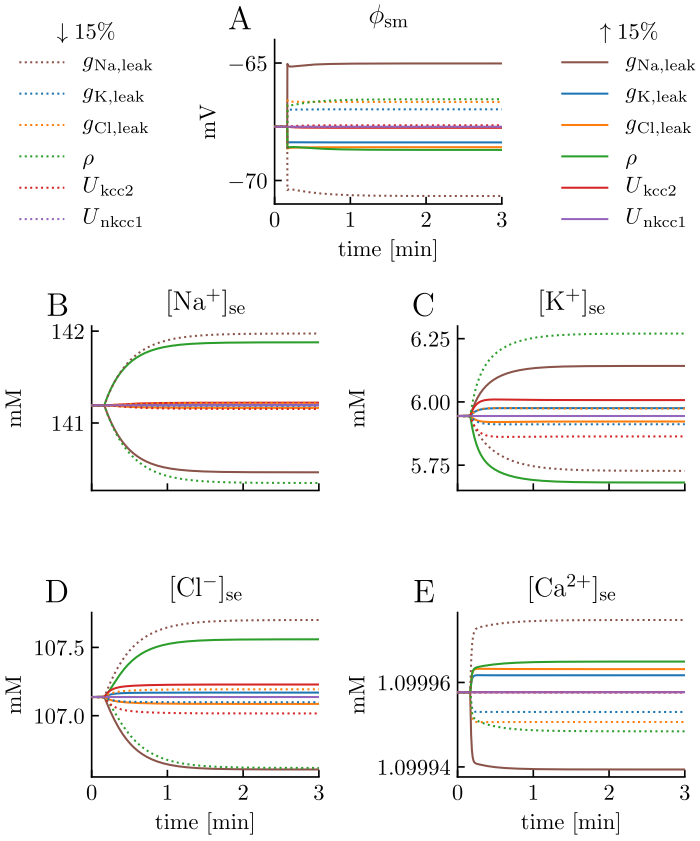

Fig 4. Sensitivity analysis. Sensitivity of **(A)** the somatic membrane potential (ϕ_{sm}) and **(B-E)** ion concentrations outside the soma to variations of the leak conductances $\bar{g}_{Na,leak}$, $\bar{g}_{K,leak}$, and $\bar{g}_{Cl,leak}$, the ATPase pump strength ρ, and the co-transporter strengths U_{nkcc1} and U_{kcc2}. The model was run for 10 s with default parameters. At $t = 10$ s, selected parameters were changed, one per simulation, by ±15% of their default value. In all cases, the model approached a new steady state during the 3 min simulation, which was not dramatically different from the default steady state. The resting potential was most sensitive to $\bar{g}_{Na,leak}$. This was not surprising, as Na^+ has the reversal potential (57 mV) that is furthest away from the resting potential (≈ -68 mV), making the driving force ($\phi_m - E_k$) largest for Na^+. All concentration variables were most sensitive either to $\bar{g}_{Na,leak}$ or ρ. For $[Ca^{2+}]_{se}$ and $[Cl^-]_{se}$ the sensitivity to these parameters were indirect, i.e., through their effects on the resting potential and driving forces. **(A-E)** Results only shown for somatic compartments, as they were almost identical in the the dendritic compartments. Only extracellular concentrations were shown, but intracellular concentrations followed the same time coarse and intracellular deviances from default values were smaller (due to larger intracellular volume fraction). As we showed in Fig 3L, the $Ca^{2+}/2Na^+$ exchanger is not active during rest, and it was therefore not included in the sensitivity analysis.

The edPR model reproduces the short term firing properties of the original PR model.

A motivation behind basing the electrodiffusive (edPR) model on a previously developed (PR) model, was that we wanted to use the firing properties of the original PR model as a "ground truth" when constraining the edPR model. In particular, we wanted the edPR model to qualitatively reproduce the interplay between somatic action potentials and dendritic Ca^{2+} spikes, as this was an essential feature of the original PR model [3]. In the PR model, this interplay depended strongly on the coupling strength (coupling conductance) between the soma and dendrite compartment. A weak coupling resulted in a wobbly ping-pong effect, where a somatic AP triggered a dendritic Ca^{2+} spike, which in turn fed back to the soma, giving rise to secondary oscillations in ϕ_m (Fig 5A). With a strong (about five times stronger) coupling, the somatic and dendritic responses became more similar in shape, as expected (Fig 5B).

Since the edPR model contained membrane mechanisms and ephaptic effects not present in the PR model, selected parameters in the edPR model had to be re-tuned in order to obtain similar firing as the PR model (see Methods). With the selected parameterization of the edPR model (see the Parameterizations section), we were able to reproduce the characteristic features seen in the PR model for a weak (Fig 5C) and strong (about five times stronger) coupling between the soma and dendrite (Fig 5D).

The edPR model predicts homeostatic failure due to high firing rate.

As previously discussed, the PR model was, as most existing neuronal models, constructed under the assumption that ion concentration effects are negligible, an assumption that is justified for short term neurodynamics, and for long term dynamics provided that the activity level is sufficiently low for the homeostatic mechanisms to maintain concentrations close to baseline over time. Hence, we expect there to be a scenario (S1) with a moderately low firing rate, where the PR and edPR can fire continuously and regularly over a long time exhibiting similar firing properties, and another scenario (S2) with a higher firing rate, where the PR and edPR models exhibit similar firing properties initially in the simulation, but where the dynamics of the two models diverge over time due to homeostatic failure accounted for by the edPR model, but not the PR model (which ad hoc assume perfect homeostasis). Simulations of two such scenarios are shown in Figs 6 and 7.

To simulate scenario S1, the PR model (Fig 6A-B) and edPR model (Fig 6C-J) were given a constant input (see figure caption) that gave them a firing rate of 1 Hz. Both models settled at a regular firing rate, and in neither of them the firing pattern changed over time, even in simulations of as much as an hour of biological time. For the edPR model, the S1 scenario is the same as that simulated for only a brief period in Fig 3. There, we observed that the ion concentrations gradually changed during the first seconds after the onset of

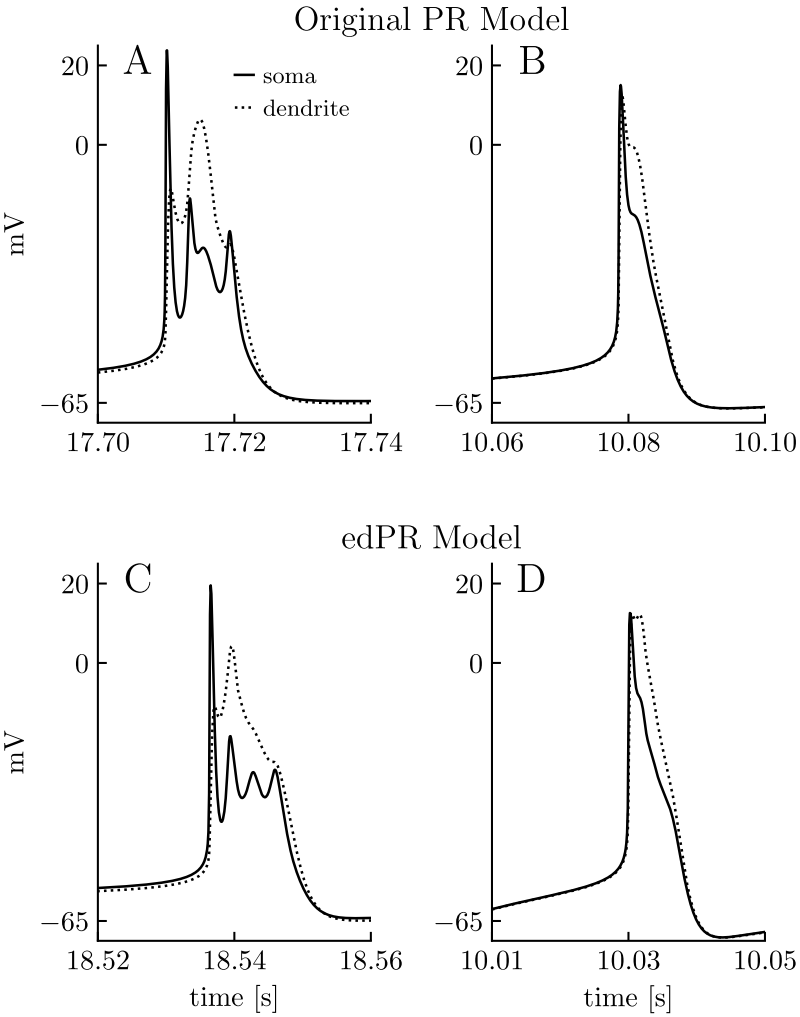

Fig 5. Short term dynamics of the PR and edPR models. The original PR model (top row) and the edPR model (bottom row) exhibit the same spike shape characteristics. **(A)** Spike shape in PR model for weak coupling (low coupling conductance) between the soma and the dendrite. **(B)** Spike shape in PR model for strong coupling (high intracellular conductivity) between the soma and the dendrite. **(C)** Spike shape in edPR model for weak coupling between the soma and the dendrite. **(D)** Spike shape in edPR model for strong coupling between the soma and the dendrite. **(A-D)** A step-stimulus current was turned on at $t = 10\,\mathrm{s}$, with stimulus strength being $1.35\,\mu\mathrm{A/cm^2}$ in **(A)**, $0.78\,\mu\mathrm{A/cm^2}$ in **(B)**, 31 pA in **(C)**, and 27 pA in **(D)**. The panels show snapshots of a selected spike. See the Parameterizations section in Methods for a full description of the parameters used.

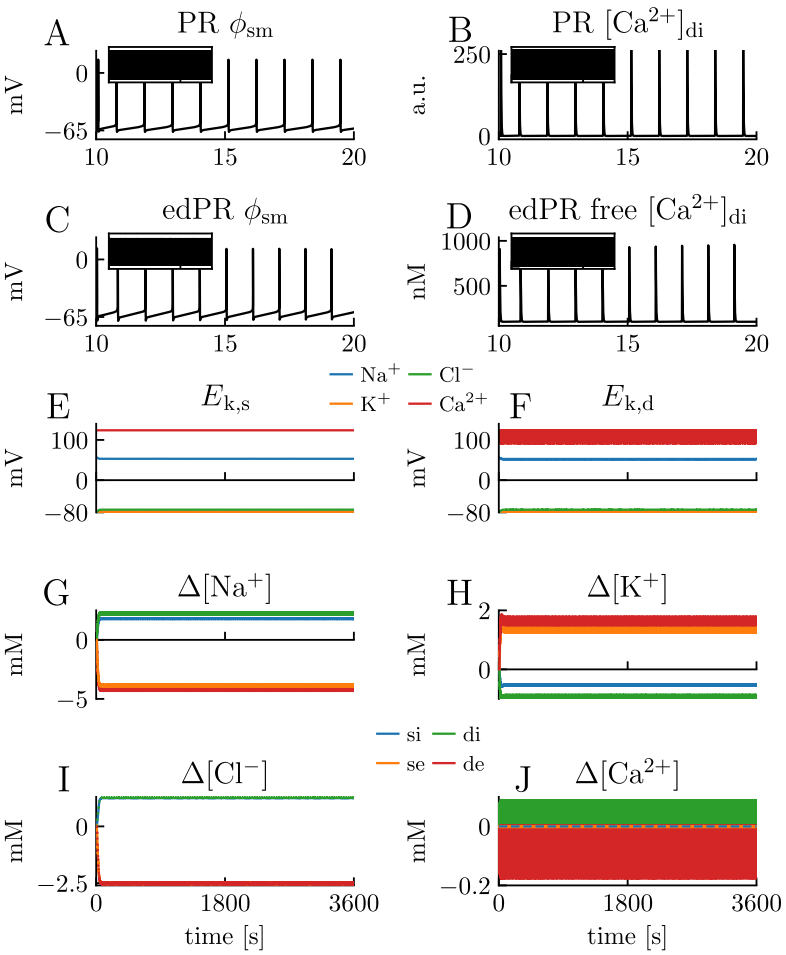

Fig 6. Model comparison for scenario with low frequency firing. Simulations on the PR model and edPR model when both models are driven by a constant input, giving them a firing rate of about 1 Hz. Simulations covered one hour (3600 s) of biological time. **(A-D)** A 10 s sample of the dynamics of the somatic membrane potential ϕ_{sm} and dendritic (free) Ca^{2+} concentration in the PR model **(A-B)** and edPR model **(C-D)**. This regular firing pattern was sustained over the full 3600 s simulation in both models (inset panels). **(D)** Of the total amount of intracellular Ca^{2+}, only 1% (as plotted) was assumed to be free (unbuffered). **(E-F)** Ionic reversal potentials and **(G-J)** ion concentrations in the edPR model did not vary on a long time scale. Indices i, e, s, and d indicate *intracellular, extracellular, soma*, and *dendrite*, respectively. **(A-J)** Stimulus onset was $t = 10\,\text{s}$ in both models, and stimulus strength was $i_{\text{stim}} = 0.78\,\mu\text{A/cm}^2$ in the PR model **(A-B)** and $i_{\text{stim}} = 27\,\text{pA}$ in the edPR model **(C-J)**. See the Parameterizations section in Methods for a full description of the parameters used.

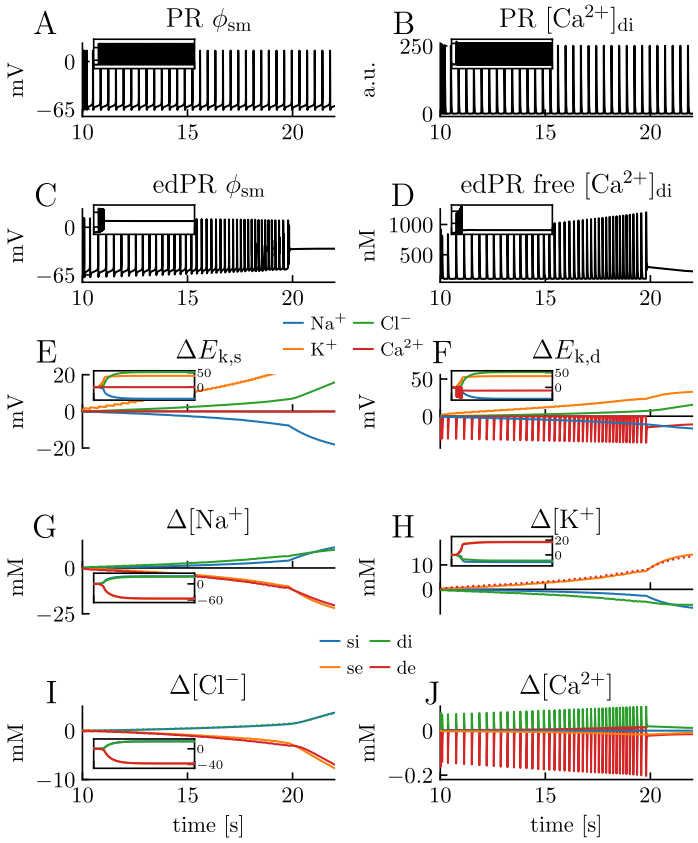

Fig 7. Model comparison for scenario with high frequency firing. Simulations on the PR model and edPR model when both models are driven by a constant input, giving them a firing rate of about 3 Hz. Simulations covered 200 s of biological time. **(A-D)** A 12 s sample of the dynamics of the somatic membrane potential ϕ_{sm} and dendritic (free) Ca^{2+} concentration in the PR model **(A-B)** and edPR model **(C-D)**. The regular firing pattern in the PR model **(A-B)** was sustained over the full 200 s simulation (inset panels), while the edPR model stopped firing and entered depolarization block around $t = 20$ s. **(D)** Of the total amount of intracellular Ca^{2+}, only 1% (as plotted) was assumed to be free (unbuffered). **(E-F)** Ionic reversal potentials and **(G-J)** ion concentrations in the edPR model varied throughout the simulation, and gradually diverged from baseline conditions. Indices *i*, *e*, *s*, and *d* indicate *intracellular, extracellular, soma*, and *dendrite*, respectively. Main panels show 12 s samples of the ion concentration dynamics, while insets show the dynamics over the full 200 s simulations. **(A-J)** Stimulus onset was $t = 10$ s in both models, and stimulus strength was $i_{stim} = 1.55\,\mu A/cm^2$ in the PR model **(A-B)** and $i_{stim} = 48$ pA in the edPR model **(C-J)**. See the Parameterizations section in Methods for a full description of the parameters used.

stimulus (Fig 3E-H). However, for endured firing, the ion concentrations and reversal potentials settled on a (new) dynamic steady state (Fig 6E-J), where they deviated by ∼1-5 mM from the baseline concentrations during rest (i.e., for edPR receiving no input). The apparent "thickness" of the curves (e.g., the red curve for K^+ in Fig 6H) is due to concentration fluctuations at the short time scale of AP firing. However, after each AP, the homeostatic mechanisms managed to re-establish ionic gradients before the next AP occurred, so that no slow concentration-dependent effect developed in the edPR model at a long time scale.

To simulate scenario S2, the PR model (Fig 7A-B) and edPR model (Fig 7C-J) were given a constant input (see figure caption) that gave them a firing rate of about 3 Hz. The PR model, which included no concentration-dependent effects, settled on a regular firing rate that it could maintain for an arbitrarily long time. Unlike the PR model, the edPR model did not settle at a steady state, but had a firing rate of ∼3 Hz only for a period of ∼5 s after stimulus onset. During this period, the ion concentrations gradually diverged from the baseline levels (Fig 7G-J). The corresponding changes in ionic reversal potentials (Fig 7E-F) affected the neuron's firing properties and caused its firing rate to gradually increase before it eventually entered the depolarization block and got stuck at about $\phi_m = -30$ mV. The main explanation behind the altered firing pattern was the change in the K^+ reversal potential, which, for example, at 9 s after stimulus onset ($t = 19$ s) had increased by as much as 20 mV from baseline. This shift led to a depolarization of the neuron, which explains both the (gradually) increased firing rate and the (final) depolarization block, i.e., the condition where ϕ_m could no longer repolarize to levels below the firing threshold, and AP firing was abolished due to a permanent inactivation of active Na^+ channels. Neuronal depolarization block is a well-studied phenomenon, which is often caused by high extracellular K^+ concentrations [65].

The homeostatic failure in S2 was due to the edPR model having a too high firing rate for the ion pumps and cotransporters to maintain ion concentrations close to baseline. The firing rate of 3 Hz was the limiting case (found by trial and error), i.e., for lower firing rates than this, the model could maintain regular firing for an arbitrarily long time. As many neurons can fire at quite high frequencies, a tolerance level of 3 Hz might seem a bit low, and we here provide some comments to this. Firstly, we note that the edPR model could fire at 3 Hz (and gradually higher frequencies) for about 9 s, and could also maintain a higher firing rate than this for a limited time. Secondly, the PR model, and thus the edPR model, represented a hippocampal CA3 neuron, which has been found to have an average firing rate of less than 0.5 Hz [66], so that endured firing of ≥3 Hz may be abnormal for these neurons. Thirdly, under biological conditions, glial cells, and in particular astrocytes, provide additional homeostatic functions [67] that were not accounted for in the edPR model, and the inclusion of such functions would probably increase the tolerance level of the neuron. Fourthly, the (3 Hz) tolerance level was a consequence of modeling choices and could be made higher, e.g., by increasing pump rates or compartment volumes. However, we did not do any model tuning in order to increase the tolerance level, as we, in

light of the above arguments, considered a 3 Hz tolerance level to be acceptable.

The edPR model predicts homeostatic failure due to impaired homeostatic mechanisms.

Above we simulated homeostatic failure occurring because the firing rate became too high for the homeostatic mechanisms to keep up (S2). Homeostatic failure may also occur due to impairment of the homeostatic mechanisms, either due to genetic mutations (see, e.g., [68]) or because the energy supply is reduced, such as after a stroke (see, e.g., [25]). Here, we have used the edPR model to simulate a version of this, i.e., a third scenario (S3) where the ATP-dependent mechanisms, that is, the $3Na^+/2K^+$ pumps and the $Ca^{2+}/2Na^+$ exchangers, were turned off.

In S3, the neuron received no external input, so that the dynamics of the neuron was solely due to gradually dissipating transmembrane ion concentration gradients. After an initial transient, we observed a slow and gradual increase in the membrane potential for about 48 s (Fig 8A). This coincided with a slow and gradual change in the ion concentrations (Fig 8D-G) and ionic reversal potentials (Fig 8B-C) due to predominantly passive leakage over the membrane.

At about $t = 48$ s, the membrane potential reached the firing threshold, at which point the active channels started to use what was left of the concentration gradients to generate action potentials and Ca^{2+} spikes. This resulted in a burst of activity. During this bursts of activity, the concentration gradients dissipated even faster, since both active and passive channels were then open. As a consequence, the "resting" membrane potential was further depolarized and the neuron went into depolarization block [65]. After this, the neuron continued to "leak" until it settled at a new steady state. The non-zero final equilibrium potential is known as the Donnan equilibrium or the Gibbs-Donnan equilibrium [69]. The reason why the cell did not approach an equilibrium with $\phi_m = 0$ and identical ion concentrations on both side of the membrane, is that the model contained static residual charges, representing negatively charged macromolecules typically residing in the intracellular environment (see Methods), the sum of which resulted in a final state with a negatively charged inside. In addition, since the Ca^{2+} channel inactivated, and since the model had no passive Ca^{2+} leakage, Ca^{2+} could end up being trapped inside/outside the membrane and did not by necessity approach the Donnan equilibrium, although it was close to it.

As the Ca^{2+} dynamics in Fig 8G may seem counterintuitive, we here give some additional explanation of it. During the burst and initial stages of the depolarization block, the dendritic Ca^{2+} channels were open. Extracellular Ca^{2+} then diffused from the soma towards the dendrite, where it flowed into the neuron. This resulted in a low Ca^{2+} concentration in both extracellular compartments and a high Ca^{2+} concentration in the intracellular dendritic compartment. The reason why the intracellular Ca^{2+} equilibrated more slowly than the extracellular, was that, by assumption, only 1% of the intracellular Ca^{2+} concentration was

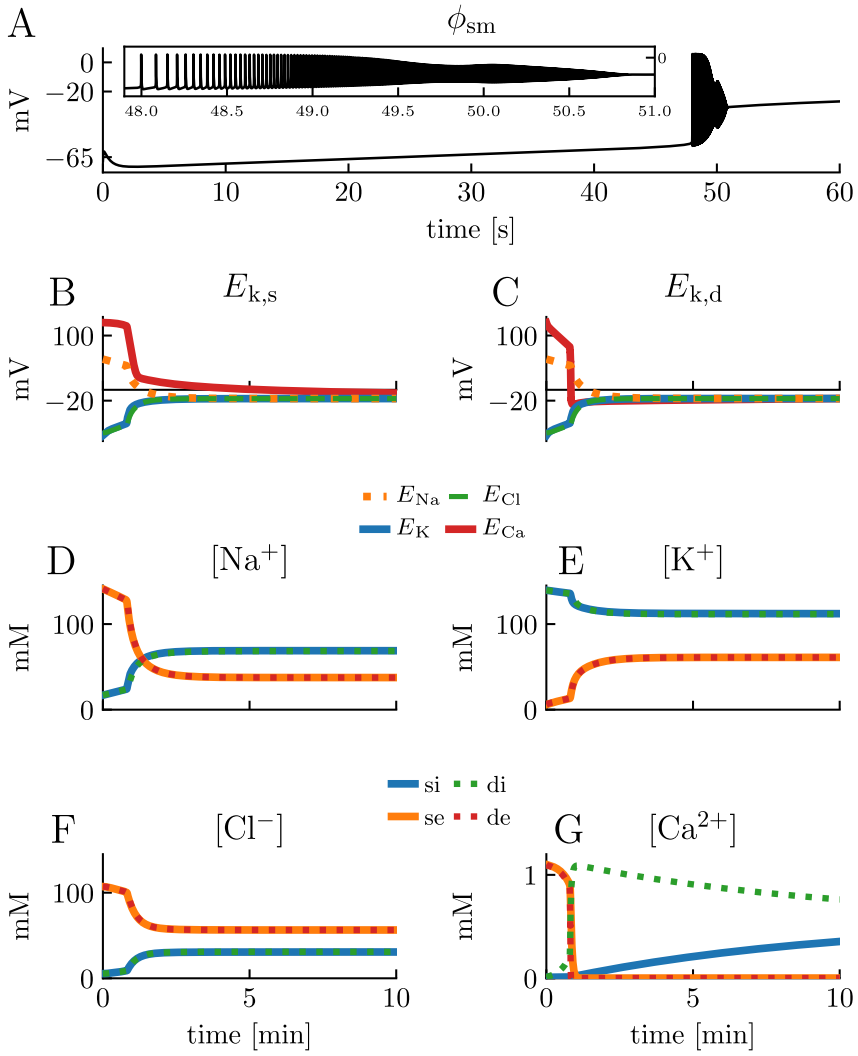

Fig 8. The wave of death. Simulation on the edPR model when the $3Na^+/2K^+$ pumps and the $Ca^{2+}/2Na^+$ exchangers were turned off. The model received no external stimulus. The simulation covered 10 minutes of biological time. **(A)** A 60 s sample of the dynamics of the somatic membrane potential ϕ_{sm}. Inset shows a close-up of the burst of activity occurring at about $t = 48$ s. **(B-C)** Reversal potentials in the soma **(B)** and dendrite **(C)**. **(D-G)** Ion concentrations in all four compartments. Somatic and dendritic concentrations were almost identical for all ion species except for Ca^{2+}. Indices i, e, s, and d indicate *intracellular, extracellular, soma*, and *dendrite*, respectively. See the Parameterizations section in Methods for a full description of the parameters used.

unbuffered and free to diffuse (see Methods), hence, the effective intracellular concentration gradient was a factor 100 lower than it "appears" in Fig 8G.

A pattern resembling that in Fig 8A, i.e., a period of silence, followed by a burst of activity, and then silence again, has been seen in experimental EEG recordings of decapitated rats [70], where the activity burst was referred to as "the wave of death", and the phenomenon was ascribed to the lack of energy supply to homeostatic mechanisms. The simulation in Fig 8A represents the single-cell correspondence to this death wave. We note that this phenomenon has been simulated and analyzed thoroughly in a previous modeling study, using a simpler, single compartmental model with ion conservation [40]. We, therefore, do not analyze it further here.

Loss in accuracy when neglecting electrodiffusive effects on concentration dynamics

The concentration-dependent effects studied in the previous subsection were predominantly due to changes in ionic reversal potentials. Effects like this could, therefore, be accounted for by any model that in some way incorporates ion concentration dynamics [27–29, 33–57], provided that the ion concentration dynamics is accurately modeled. As we argued in the Introduction, previous multicompartmental neuron models that do incorporate ion concentration dynamics have not done it in a complete, ion conserving way that ensures a biophysically consistent relationship between ion concentration, electrical charge, and electrical potentials (see, e.g., [27, 48–57]). To specify, the change in the ion concentration in a given compartment will, in reality, depend on (i) the transmembrane influx of ions into this compartment, (ii) the diffusion of ions between this compartment and its neighboring compartment(s), and (iii) the electrical drift of ions between this compartment and its neighboring compartment(s). Some of the cited models account for only (i) [27, 49, 51], others account for (i) and (ii) [48, 50, 52–57], but neither account for (iii). When (iii) is not accounted for, electrical and diffusive processes are implicitly treated as independent processes, a simplifying assumption which is also incorporated in the reaction-diffusion module [71] in the NEURON simulation environment [72]. In models that apply this assumption, there will therefore be drift currents (along axons and dendrites) that affect ϕ_{m} (through the cable equation), but not the ion concentration dynamics, although they should, since also the drift currents are mediated by ions.

Here, we use simulations on the edPR model to test the inaccuracy introduced when not accounting for the effect of drift currents on ion concentration dynamics. We do so by comparing how many ions that were transferred from the somatic to the dendritic compartment through the intracellular (Fig 9A) and extracellular (Fig 9B) space, due to ionic diffusion (orange curves) versus electrical drift (blue curves), throughout the simulation in Fig 3. We note that Fig 9 shows the accumulatively moved number of ions (from time zero to t) due to axial fluxes exclusively. That is, the large number of, for example, Na^+ ions transported intracellularly from the dendrite to the soma (negative sign) in Fig 9A1, does

not by necessity mean that Na^+ ions were piling up in the soma compartment, as the membrane efflux of Na^+ was not accounted for in the figure.

Although diffusion tended to dominate the intracellular transport of ions on the long time scale (Fig 9A1-A4), the transport due to electrical drift was not vanishingly small. For example, the number of K^+ and Cl^- ions transported by electrical drift was at the end of the stimulus period ($t = 20\,\mathrm{s}$) about 35 % of the transport due to diffusion for both species. In the extracellular space, diffusion was the clearly dominant transporter of Na^+ and K^+ (Fig 9B1-B2), while diffusion and electrical drift were of comparable magnitude for the other ion species (Fig 9B3-A4). Of course, these estimates are all specific to the edPR model, as they will depend strongly on the included ion channels, ion pumps and cotransporters, and on how they are distributed between the soma and dendrite. In general, however, the simulations in Fig 9 suggest that electrical drift is likely to have a non-negligible effect on ion concentration dynamics, and that ignoring this effect will give rise to rather inaccurate estimates.

Finally, we also converted the sum of ionic fluxes in Fig 9 into an effective current, represented as the number of transported unit charges, e^+ (Fig 9A5-B5). Interestingly, diffusion and drift contributed almost equally to the axial charge transport in the system. We note, however, that the movement of charges per time unit is indicated by the slope of the curves, which was much larger for the drift case (blue curve) than for diffusion (orange curve). The drift curve had a jigsaw shape, which shows that drift was moving charges back and forth in the system, while the diffusion always went in the same direction, explaining why it, despite being smaller than the drift current, had a comparably large accumulative effect on charge transport. The temporally averaged picture of charge transport that emerges from Fig 9A5 is that of a slow current loop where charge is transferred intracellularly from the soma to the dendrite (Fig 9A5), where it crosses the membrane (outward current), and then is transferred extracellularly back from the dendrite to the soma (Fig 9B5), before crossing the membrane again (inward current). This configuration is similar to the slow loop current seen during spatial buffering by astrocytes (see, e.g. Fig 1 in [67]).

Loss in accuracy when neglecting electrodiffusive effects on voltage dynamics

In the previous section, we investigated the consequences of neglecting (iii) the contribution of drift currents on ion concentration dynamics. Here, we investigate the consequences of neglecting the effect of ionic diffusion (along dendrites) on the electrical potential, focusing on the extracellular potential ϕ_e. Forward modeling of extracellular potentials is typically based on volume conductor (VC) theory [16–18, 20, 21], which assumes that diffusive effects on electrical potentials are negligible. Being based on a unified electrodiffusive KNP framework (Fig 1), the edPR model accounts for the effects of ionic diffusion on the electrical potentials, and can thus be used to address the validity of this assumption.

To illustrate the effect of diffusion on ϕ_e, we may split it into a component $\phi_{\mathrm{VC,e}}$ explained by standard VC-theory, and a component $\phi_{\mathrm{diff,e}}$ representing the

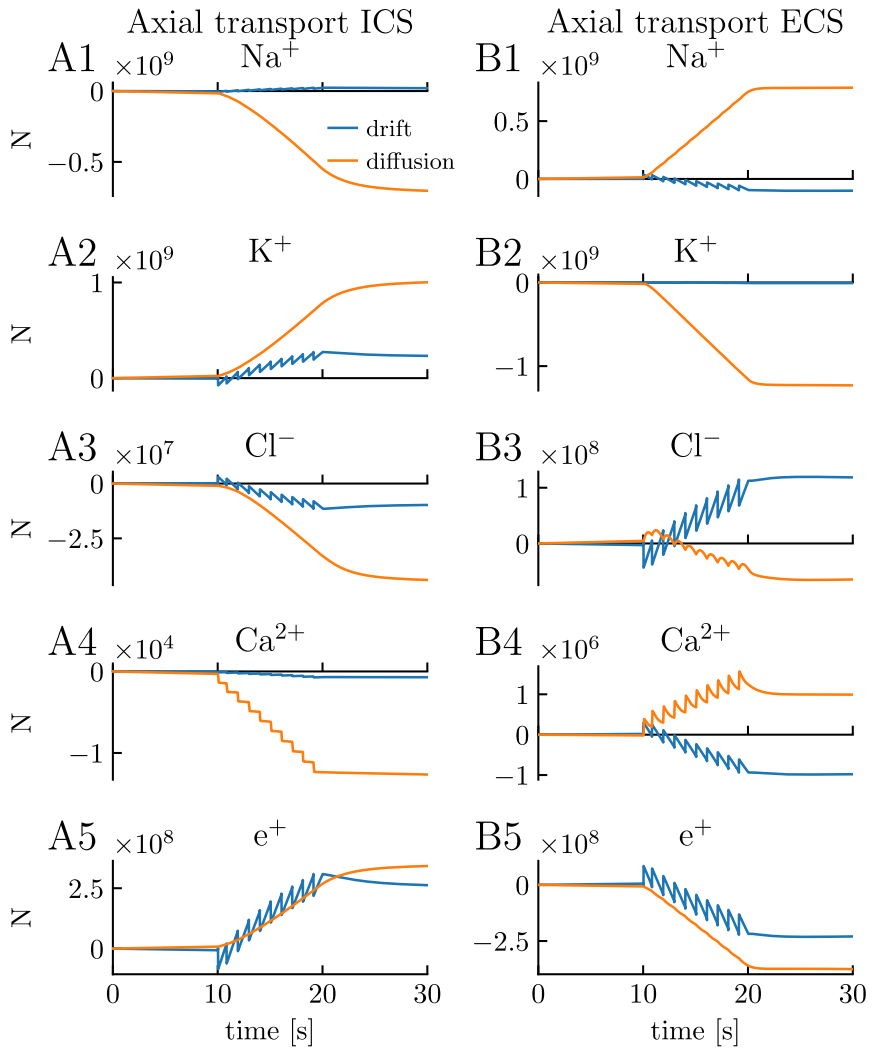

Fig 9. Axial transport of ions and charge due to drift versus diffusion. (A1-A4) The number of ions transported intracellularly from soma to dendrite from time zero to t by electrical drift versus ionic diffusion. **(B1-B4)** The number of ions transported extracellularly from (outside) soma to (outside) dendrite from time zero to t. **(A5)** Net charge transported intracellularly from soma to dendrite, represented as the number of unit charges e^+. **(B5)** Net charge transported extracellularly from soma to dendrite, represented as the number of unit charges e^+. **(A-B)** The simulation was the same as in Fig 3. See the Analysis section in Methods for a description of how we did the calculations.

additional contribution caused by diffusive currents (Eq 81). In the simulation in Fig 3, the diffusive contribution was found to be very small compared to the VC-component (Fig 10). However, while $\phi_{\mathrm{VC,e}}$ fluctuated rapidly from negative to positive values during neuronal activity, $\phi_{\mathrm{diff,e}}$ varied on a slower time scale and had the same directionality throughout the simulation. This is equivalent to what we saw in Fig 9B5, i.e., that diffusion always moved charge in the same direction. Moreover, if we take the temporal averages of the potentials over the time series in Fig 10A, we find that they are $-0.0023\,\mathrm{mV}$, $0.0037\,\mathrm{mV}$, and $-0.0060\,\mathrm{mV}$ for ϕ_{e}, $\phi_{\mathrm{diff,e}}$, and $\phi_{\mathrm{VC,e}}$, respectively. This shows that the average diffusion- and VC-components of the total potential were of the same order of magnitude. As we also have demonstrated in previous studies, diffusion is thus likely to be important for the low-frequency components of extracellular potentials [31, 32, 73, 74]. Albeit small, the slowly varying diffusion evoked shifts in ϕ_{e} are putatively important for explaining the direct-current (DC) like shifts and long-time concentration dynamics reported during, e.g., spreading depression [25, 26].

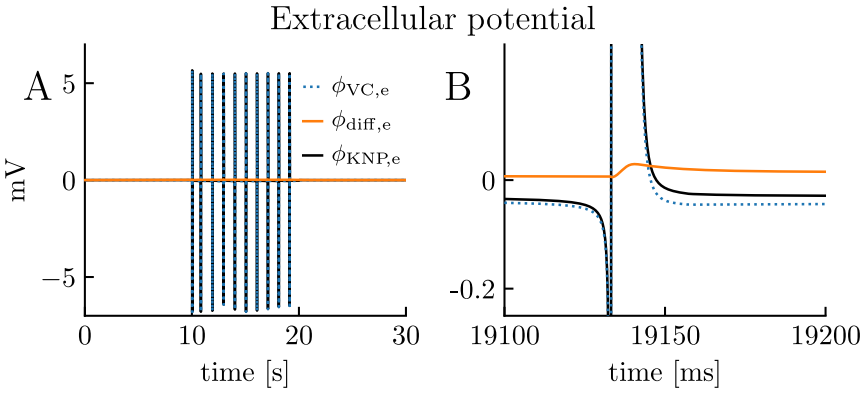

Fig 10. Effect of diffusion on extracellular potential. The extracellular potential ϕ_{e} in the edPR model, split (cf. Eq 81) into a component explained by standard VC-theory ($\phi_{\mathrm{VC,e}}$) and a "correction" ($\phi_{\mathrm{diff,e}}$) when diffusive contributions are accounted for. **(A-B)** The simulation was the same as in Fig 3. **(B)** Close-up of selected AP in **(A)**. See the Analysis section in Methods for a description of how we calculated $\phi_{\mathrm{VC,e}}$ and $\phi_{\mathrm{diff,e}}$.

Discussion

The original Pinsky–Rinzel (PR) is a reduced model of a hippocampal neuron, which reproduces the essential somatodendritic firing properties of CA3 neurons despite having only two compartments [3]. Simplified neuron models like that are useful, partly because their reduced complexity makes them easier to analyze, and as such, can lead to insight in key neuronal mechanisms, and partly because they demand less computer power and can be used as modules in large scale

network simulations. Whereas the PR model, as most available neuron models, assumes that ion concentrations remain constant during the simulated period, the electrodiffusive Pinsky–Rinzel (edPR) model proposed here models ion concentration dynamics explicitly. The edPR model may thus be seen as a supplement to the PR model, which should be applied to simulate conditions where ion concentrations are expected to vary with time.

In the results section, we showed that the edPR model closely reproduced the firing properties of the PR model for short term dynamics (Fig 5), and for long term dynamics provided that the firing rate was sufficiently low for the homeostatic mechanisms to maintain ion concentrations close to baseline (Fig 6). We also showed that if the firing rate became too high (Fig 7), or if the homeostatic mechanisms were impaired (Fig 8), unsuccessful homeostasis would cause ion concentrations to gradually shift over time, and lead to slowly developing changes in the firing properties of the edPR model, changes that were not accounted for by the original PR model. The edPR model was based on an electrodiffusive framework [60], which ensured a consistent relationship between ion concentrations, electrical charge, and electrical potential in four compartments. To our knowledge, the edPR model is the first multicompartmental neuronal model that ensures complete and consistent ion concentration and charge conservation.

Model assumptions

The construction of the edPR model naturally involved making a set of modeling choices, and the most important of these are discussed here. Firstly, in the construction of the model, we focused on morphological simplicity, biophysical rigor, and mechanistic understanding, rather than on replicating any specific biological scenario and incorporating biological details. Secondly, simultaneous data of variations in all intra- and extracellular concentrations during neuronal firing are not available, and it might not even be feasible to obtain such data. Consequently, computational modeling based on biophysical constraints may be the best means to estimate it. The concentration dynamics in the edPR model were thus not directly constrained to data but constrained so that there was, at all times, an internally consistent relationship between all ion concentrations and all electrical potentials, ensuring an electroneutral bulk solution. Thirdly, to include extracellular dynamics to models of neurons or networks of such is computationally challenging, since the extracellular space, in reality, is an unconfined three-dimensional continuum, locally affected by populations of nearby neurons and glial cells. As we wanted to keep things simple and conceptual, we chose to use closed boundary conditions, i.e., no ions and no charge were allowed to leave or enter the system consisting of the single (2-compartment) neuron and its local and confined (2-compartment) surrounding (Fig 2). Tecnically, it would be straightforward to increase the number of compartments (i.e., the spatial resolution) in the model.

A consequence of using closed boundary conditions was that the extracellular (like the intracellular) currents became one-dimensional (from soma to dendrite),

while in reality, extracellular currents pass through a three-dimensional volume conductor. The edPR model could be made three dimensional if embedded in a bi- or tri-domain model (as discussed below). However, currently, it is 1D, and the effect of the 1D assumption was essentially an increase in the total resistance (fewer degrees of freedom) for extracellular currents, which gave rise to an artificially high amplitude in extracellular AP signatures (Fig 3). We note, however, that the closed boundary is actually equivalent to assuming periodic boundary conditions, so that the edPR model essentially simulates the hypothetical case of a population of perfectly synchronized neurons, i.e., one where all neurons are doing exactly the same as the simulated neuron, so that no spatial variation occurs. Likely, this may give accurate predictions for ion concentration shifts over time, as these reflect a temporal average of activity, but less accurate predictions for brief and unique electrical events, such as action potentials, which are not likely to be elicited in perfect synchrony by a large population [31].

Fourthly, to faithfully represent a morphologically complex neuron with a reduced number of compartments is a non-trivial task. Available analytical theory for collapsing branching dendrites into equivalent cylinders are generally based on certain assumptions about branching symmetries, and on preserving electrotonic distances [75]. However, it is unlikely that the length constants of electrodynamics and ion concentration dynamics scale in the same way. Hence, in the edPR model, the volumes and membrane areas of, and cross-section areas between, the two neuronal compartments were here introduced as rather arbitrary model choices, fixed at values that were verified to give agreement between the firing properties of the edPR model and the PR model.

Outlook

Being applicable to simulate conditions with failed homeostasis, the edPR model opens up for simulating a range of pathological conditions, such as spreading depression or epilepsy [22–25], which are associated with large scale shifts in extracellular ion concentrations. A particular context in which we anticipate the edPR model to be useful is that of simulating spreading depression. Previous spatial, electrodiffusive, and biophysically consistent models of spreading depression have targeted the problem at a large-scale tissue-level, using a mean-field approach [30, 76, 77]. These models were inspired by the *bi-domain* model [78], which has been successfully applied in simulations of cardiac tissue [79, 80]. The bi-domain model is a coarse-grained model, in which the tissue is considered as a bi-phasic continuum consisting of an intracellular and extracellular domain. That is, a set of intra- and extracellular variables (i.e., voltages and ion concentrations), and the ionic exchange between the intra- and extracellular domains, are defined at each point in space. This simplification allows for large scale simulations of signals that propagate through tissue but sacrifices morphological detail. In the context of spreading depression, a shortcoming with this simplification is that the leading edge of the spreading depression wave in both the hippocampus and cortex is in the layers containing the

apical dendrites [22]. This suggests that the different expression of membrane mechanisms in deeper (somatic) and higher (dendritic) layers may be crucial for fully understanding the propagation and genesis of the wave. In this context, the edPR model could enter as a module in a, let us say, *bi-times-two-domain* model, where each point in (xy) space contains a set of (i) somatic intracellular variables, (ii) somatic extracellular variables, (iii) dendritic intracellular variables, and (iv) dendritic extracellular variables, and thus accounts for the differences between the higher and lower layers. We should note that the state of the art models of spreading depression are not bi-domain models but rather tri-domain models, as they also include a glial domain to account especially for the work done by astrocytes in K^+ buffering [30, 76, 77]. Hence, to use the edPR model to expand the current spreading depression models, a natural first step would be to include a glial (astrocytic) compartment in it, so that it eventually could be implemented as a *tri-times-two-domain* model.

Methods

The Kirchoff-Nernst-Planck (KNP) framework

In the following section, we derive the KNP continuity equations for a one-dimensional system containing two plus two compartments (Fig 2A), with sealed boundary conditions (i.e., no ions can enter or leave the system). The geometrical parameters used in the edPR model were as defined in Table 1. Since typical neuronal/extracellular/glial volume fractions in neuronal tissue are 0.4/0.2/0.4 [81], we let the extracellular space be half as voluminous as the intracellular neuronal space.

Table 1. Geometrical parameters

Parameter	Value
Δx (distance between the two compartments)	$667 \cdot 10^{-6}$ m
A_s (somatic membrane area)	$616 \cdot 10^{-12}$ m^{2*}
A_d (dendritic membrane area)	$616 \cdot 10^{-12}$ m^{2*}
A_i (intracellular cross-section area)	$\alpha \cdot A_s{}^{\dagger}$
A_e (extracellular cross-section area)	$A_i/2$
V_{si} (somatic intracellular volume)	$1437 \cdot 10^{-18}$ m^{3*}
V_{di} (dendritic intracellular volume)	$1437 \cdot 10^{-18}$ m^{3*}
V_{se} (somatic extracellular volume)	$718.5 \cdot 10^{-18}$ m^{3*}
V_{de} (dendritic extracellular volume)	$718.5 \cdot 10^{-18}$ m^{3*}

* The intracellular volumes (V_{si}, V_{di}) and membrane areas (A_s, A_d) correspond to spheres with radius 7 µm.
† The parameter α describes the coupling strength of the model and is defined in the Parameterizations section. Its default value was 2.

Two kinds of fluxes are involved: transmembrane fluxes and intra- and extracellular fluxes. The framework is general to the choice of the transmembrane

fluxes. A transmembrane flux of ion species k ($j_{\mathrm{k,m}}$) represents the sum of all fluxes through all membrane mechanisms that allow ion k to cross the membrane.

Intracellular flux densities are described by the Nernst-Planck equation:

$$j_{\mathrm{k,i}} = -\frac{D_{\mathrm{k}}}{\lambda_{\mathrm{i}}^2}\frac{\gamma_{\mathrm{k}}([\mathrm{k}]_{\mathrm{di}} - [\mathrm{k}]_{\mathrm{si}})}{\Delta x} - \frac{D_{\mathrm{k}} z_{\mathrm{k}} F}{\lambda_{\mathrm{i}}^2 RT}\overline{[\mathrm{k}]}_{\mathrm{i}}\frac{\phi_{\mathrm{di}} - \phi_{\mathrm{si}}}{\Delta x}. \tag{1}$$

In Eq 1, D_{k} is the diffusion constant, γ_{k} is the fraction of freely moving ions, that is, ions that are not buffered or taken up by the ER, λ_{i} is the tortuosity, which represents the slowing down of diffusion due to obstacles, $\gamma_{\mathrm{k}}([\mathrm{k}]_{\mathrm{di}} - [\mathrm{k}]_{\mathrm{si}})/\Delta x$ is the axial concentration gradient, z_{k} is the charge number of ion species k, F is the Faraday constant, R is the gas constant, T is the absolute temperature, $\overline{[\mathrm{k}]}_{\mathrm{i}}$ is the average concentration, that is, $\gamma_{\mathrm{k}}([\mathrm{k}]_{\mathrm{di}} + [\mathrm{k}]_{\mathrm{si}})/2$, and $(\phi_{\mathrm{di}} - \phi_{\mathrm{si}})/\Delta x$ is the axial potential gradient. Similarly, the extracellular flux densities are described by

$$j_{\mathrm{k,e}} = -\frac{D_{\mathrm{k}}}{\lambda_{\mathrm{e}}^2}\frac{[\mathrm{k}]_{\mathrm{de}} - [\mathrm{k}]_{\mathrm{se}}}{\Delta x} - \frac{D_{\mathrm{k}} z_{\mathrm{k}} F}{\lambda_{\mathrm{e}}^2 RT}\overline{[\mathrm{k}]}_{\mathrm{e}}\frac{\phi_{\mathrm{de}} - \phi_{\mathrm{se}}}{\Delta x}. \tag{2}$$

In Eq 2, we do not include γ_{k}, as all ions can move freely in the extracellular space. Diffusion constants, tortuosities, and intracellular fractions of freely moving ions used in the edPR model were as in Table 2.

Table 2. Diffusion constants, tortuosities, and intracellular fractions of freely moving ions

Parameter	Value	Reference
D_{Na} (Na^+ diffusion constant)	$1.33 \cdot 10^{-9}\,\mathrm{m}^2/\mathrm{s}$	[31, 82]
D_{K} (K^+ diffusion constant)	$1.96 \cdot 10^{-9}\,\mathrm{m}^2/\mathrm{s}$	[31, 82]
D_{Cl} (Cl^- diffusion constant)	$2.03 \cdot 10^{-9}\,\mathrm{m}^2/\mathrm{s}$	[31, 82]
D_{Ca} (Ca^{2+} diffusion constant)	$0.71 \cdot 10^{-9}\,\mathrm{m}^2/\mathrm{s}$	[31, 82]
λ_{i} (intracellular tortuosity)	3.2	[60, 81]
λ_{e} (extracellular tortuosity)	1.6	[60, 81]
$\gamma_{\mathrm{Na}}, \gamma_{\mathrm{K}}, \gamma_{\mathrm{Cl}}$ (intracellular fractions of free ions)	1	
γ_{Ca} (intracellular fraction of free ions)	0.01	

Ion conservation

The KNP framework is based on the constraint of ion conservation. To keep track of ion concentrations we solve four differential equations for each ion species k:

$$\frac{d[\mathrm{k}]_{\mathrm{si}}}{dt} = -j_{\mathrm{k,sm}} \cdot \frac{A_{\mathrm{s}}}{V_{\mathrm{si}}} - j_{\mathrm{k,i}} \cdot \frac{A_{\mathrm{i}}}{V_{\mathrm{si}}}, \tag{3}$$

$$\frac{d[\mathrm{k}]_{\mathrm{di}}}{dt} = -j_{\mathrm{k,dm}} \cdot \frac{A_{\mathrm{d}}}{V_{\mathrm{di}}} + j_{\mathrm{k,i}} \cdot \frac{A_{\mathrm{i}}}{V_{\mathrm{di}}}, \tag{4}$$

$$\frac{d[\mathrm{k}]_{\mathrm{se}}}{dt} = +j_{\mathrm{k,sm}} \cdot \frac{A_{\mathrm{s}}}{V_{\mathrm{se}}} - j_{\mathrm{k,e}} \cdot \frac{A_{\mathrm{e}}}{V_{\mathrm{se}}}, \tag{5}$$

$$\frac{d[\mathrm{k}]_{\mathrm{de}}}{dt} = +j_{\mathrm{k,dm}} \cdot \frac{A_{\mathrm{d}}}{V_{\mathrm{de}}} + j_{\mathrm{k,e}} \cdot \frac{A_{\mathrm{e}}}{V_{\mathrm{de}}}. \tag{6}$$

For each compartment, all flux densities are multiplied by the area they go through and divided by the volume they enter to calculate the change in ion concentration. If we insert the Nernst-Planck equation (Eq 1) for the intracellular flux density, the first of these equations becomes:

$$\frac{d[\mathrm{k}]_{\mathrm{si}}}{dt} = -j_{\mathrm{k,sm}} \cdot \frac{A_{\mathrm{s}}}{V_{\mathrm{si}}} + \frac{A_{\mathrm{i}} D_{\mathrm{k}}}{V_{\mathrm{si}} \lambda_{\mathrm{i}}{}^2 \Delta x} \left[\gamma_{\mathrm{k}}([\mathrm{k}]_{\mathrm{di}} - [\mathrm{k}]_{\mathrm{si}}) + \frac{z_{\mathrm{k}} F}{RT} \overline{[\mathrm{k}]}_{\mathrm{i}} (\phi_{\mathrm{di}} - \phi_{\mathrm{si}}) \right], \tag{7}$$

where the voltage variables so far are undefined.

Four constraints to derive ϕ

If we have four ion species (Na^+, K^+, Cl^-, and Ca^{2+}) in four compartments, we have 20 unknown parameters (16 for [k] and four for ϕ), while Eqs 3-6 for four ion species give us only 16 equations. To solve this, we need to define additional constraints that allow us to express the potentials ϕ in terms of ion concentrations.

As we may define an arbitrary reference point for ϕ, we take

$$\phi_{\mathrm{de}} = 0, \tag{8}$$

as our first constraint, i.e., (i) the potential outside the dendrite is defined to be zero.

The second constraint is that (ii) the membrane is a parallel plate capacitor that always separates a charge Q on one side from an opposite charge $-Q$ on the other side, giving rise to a voltage difference

$$\phi_{\mathrm{m}} = Q/C_{\mathrm{m}}. \tag{9}$$

Here, C_{m} is the total capacitance of the membrane, i.e., $C_{\mathrm{m}} = c_{\mathrm{m}} A_{\mathrm{m}}$, where c_{m} is the more commonly used capacitance per membrane area. As, by definition, $\phi_{\mathrm{m}} = \phi_{\mathrm{i}} - \phi_{\mathrm{e}}$, we get:

$$\phi_{\mathrm{dm}} = \phi_{\mathrm{di}} = Q_{\mathrm{di}}/C_{\mathrm{m}}, \tag{10}$$

in the dendrite (since $\phi_{\mathrm{de}} = 0$), and

$$\phi_{\mathrm{sm}} = \phi_{\mathrm{si}} - \phi_{\mathrm{se}} = Q_{\mathrm{si}}/C_{\mathrm{m}}, \tag{11}$$

in the soma.

The third constraint is that (iii) we assume bulk electroneutrality. This means that the net charge associated with the ion concentrations in a given compartment by constraint must be identical to the membrane charge in this compartment. The intracellular dendritic charge is thus $Q_{\mathrm{di}} = F \sum_{\mathrm{k}} z_{\mathrm{k}} [\mathrm{k}]_{\mathrm{di}} V_{\mathrm{di}}$. By inserting this into Eq 10, we obtain the final expression for ϕ_{di}:

$$\phi_{\mathrm{di}} = (F \sum_{\mathrm{k}} z_{\mathrm{k}} [\mathrm{k}]_{\mathrm{di}} V_{\mathrm{di}})/(c_{\mathrm{m}} A_{\mathrm{d}}). \tag{12}$$

By inserting the equivalent expression for Q_{si} into Eq 11, we get

$$\phi_{\mathrm{si}} - \phi_{\mathrm{se}} = Q_{\mathrm{si}}/C_{\mathrm{m}} = (F \sum_{\mathrm{k}} z_{\mathrm{k}} [\mathrm{k}]_{\mathrm{si}} V_{\mathrm{si}})/(c_{\mathrm{m}} A_{\mathrm{s}}). \tag{13}$$

Here, the extracellular potential is not set to zero, so we need a fourth constraint to determine ϕ_{si} and ϕ_{se} separately.

The fourth and final constraint is that (iv) we must ensure charge anti-symmetry. For the charge anti-symmetry between the two sides of the capacitive membrane ($Q_{\mathrm{i}} = -Q_{\mathrm{e}}$) to be preserved in time, we must define our initial conditions so that this is the case at $t = 0$, and the system dynamics so that this stays the case. Hence, the system dynamics must ensure that $dQ_{\mathrm{di}}/dt = -dQ_{\mathrm{de}}/dt$ and $dQ_{\mathrm{si}}/dt = -dQ_{\mathrm{se}}/dt$. The membrane currents (in isolation) will always fulfill this criterion, as any charge that crosses the membrane by definition disappears from one side of it and pops up at the other. Hence, we thus need to make sure that also the axial currents (in isolation) fulfill the criterion. The system must thus be constrained so that, if an extracellular current transports a charge δq into a given extracellular compartment, the intracellular current must transport the opposite charge $-\delta q$ into the adjoint intracellular compartment. That is, we must have that:

$$A_{\mathrm{i}} i_{\mathrm{i}} = -A_{\mathrm{e}} i_{\mathrm{e}}, \tag{14}$$

where i_{i} and i_{e} are the intra- and extracellular current densities, respectively. To find an expression for these, we multiply Eqs 1 and 2 by $F z_{\mathrm{k}}$ and sum over all ion species k. The expressions for the intra- and extracellular current densities then become:

$$i_{\mathrm{i}} = -\frac{F}{\lambda_{\mathrm{i}}^2 \Delta x} \sum_{\mathrm{k}} D_{\mathrm{k}} z_{\mathrm{k}} \gamma_{\mathrm{k}} ([\mathrm{k}]_{\mathrm{di}} - [\mathrm{k}]_{\mathrm{si}}) - \frac{F^2}{RT \lambda_{\mathrm{i}}^2 \Delta x} \sum_{\mathrm{k}} D_{\mathrm{k}} {z_{\mathrm{k}}}^2 \overline{[\mathrm{k}]}_{\mathrm{i}} (\phi_{\mathrm{di}} - \phi_{\mathrm{si}}), \tag{15}$$

$$i_{\mathrm{e}} = -\frac{F}{\lambda_{\mathrm{e}}^2 \Delta x} \sum_{\mathrm{k}} D_{\mathrm{k}} z_{\mathrm{k}} ([\mathrm{k}]_{\mathrm{de}} - [\mathrm{k}]_{\mathrm{se}}) - \frac{F^2}{RT \lambda_{\mathrm{e}}^2 \Delta x} \sum_{\mathrm{k}} D_{\mathrm{k}} {z_{\mathrm{k}}}^2 \overline{[\mathrm{k}]}_{\mathrm{e}} (\phi_{\mathrm{de}} - \phi_{\mathrm{se}}). \tag{16}$$

In Eq 15, the first term is the diffusion current density:

$$i_{\mathrm{diff,i}} = -\frac{F}{\lambda_{\mathrm{i}}^2 \Delta x} \sum_{\mathrm{k}} D_{\mathrm{k}} z_{\mathrm{k}} \gamma_{\mathrm{k}} ([\mathrm{k}]_{\mathrm{di}} - [\mathrm{k}]_{\mathrm{si}}), \tag{17}$$

which is defined by the ion concentrations. The second term is the field driven current density

$$i_{\mathrm{field,i}} = -\sigma_i \frac{(\phi_{\mathrm{di}} - \phi_{\mathrm{si}})}{\Delta x}, \tag{18}$$

where we have identified the conductivity as

$$\sigma_{\mathrm{i}} = \frac{F^2}{RT\lambda_{\mathrm{i}}^2} \sum_{\mathrm{k}} D_{\mathrm{k}} {z_{\mathrm{k}}}^2 \overline{[\mathrm{k}]}_{\mathrm{i}}. \tag{19}$$

Similarly, Eq 16 can be written in terms of $i_{\mathrm{diff,e}}$, $i_{\mathrm{field,e}}$, and σ_{e}. By combining Eqs 14, 15, and 16, we obtain:

$$-A_{\mathrm{i}} i_{\mathrm{diff,i}} + A_{\mathrm{i}}\sigma_{\mathrm{i}} \cdot \frac{(\phi_{\mathrm{di}} - \phi_{\mathrm{si}})}{\Delta x} = A_{\mathrm{e}} i_{\mathrm{diff,e}} - A_{\mathrm{e}}\sigma_{\mathrm{e}} \cdot \frac{(\phi_{\mathrm{de}} - \phi_{\mathrm{se}})}{\Delta x}. \tag{20}$$

In Eq 20, ϕ_{di} and ϕ_{de} are already known from Eqs 8 and 12, while i_{diff} and σ are expressed in terms of ion concentrations. We may thus solve Eqs 13 and 20 for the last two voltage variables ϕ_{se} and ϕ_{si}:

$$\phi_{\mathrm{se}} = \left(\phi_{\mathrm{di}} - \frac{\Delta x}{\sigma_{\mathrm{i}}} \cdot i_{\mathrm{diff,i}} - \frac{A_{\mathrm{e}}\Delta x}{A_{\mathrm{i}}\sigma_{\mathrm{i}}} \cdot i_{\mathrm{diff,e}} - \frac{Q_{\mathrm{si}}}{c_{\mathrm{m}} A_{\mathrm{s}}}\right) / \left(1 + \frac{A_{\mathrm{e}}\sigma_{\mathrm{e}}}{A_{\mathrm{i}}\sigma_{\mathrm{i}}}\right), \tag{21}$$

$$\phi_{\mathrm{si}} = \frac{Q_{\mathrm{si}}}{c_{\mathrm{m}} A_{\mathrm{s}}} + \phi_{\mathrm{se}}. \tag{22}$$

Membrane mechanics

Leakage channels

In the original PR model, the membrane leak current represents the combined contribution from all ion species. When using the KNP framework, on the other hand, where we keep track of all ions separately, the leak current must be ion-specific. We modeled this as in [45], that is, for each ion species k, we implemented a passive flux density across the membrane

$$j_{\mathrm{k,leak}} = \bar{g}_{\mathrm{k,leak}}(\phi_{\mathrm{m}} - E_{\mathrm{k}})/(F z_{\mathrm{k}}), \tag{23}$$

where $\bar{g}_{\mathrm{k,leak}}$ is the ion conductance, ϕ_{m} is the membrane potential, E_{k} is the reversal potential, F is the Faraday constant, and z_{k} is the charge number. The reversal potential is a function of ion concentrations, and is calculated using the Nernst equation:

$$E_{\mathrm{k}} = \frac{RT}{z_{\mathrm{k}} F} \ln \frac{[\mathrm{k}]_{\mathrm{e}}}{\gamma_{\mathrm{k}}[\mathrm{k}]_{\mathrm{i}}}. \tag{24}$$

Here, R is the gas constant, T is the absolute temperature, γ_{k} is the intracellular fraction of free ions, and $[\mathrm{k}]_{\mathrm{e}}$ and $[\mathrm{k}]_{\mathrm{i}}$ are the concentrations of ion k outside and inside the cell, respectively. We included Na^+, K^+, and Cl^- leak currents in both compartments.

Active ion channels

All active ion channel currents were adopted from the original PR model [3], as they were described in [8], and converted to ion channel fluxes. The soma compartment contained a Na^+ flux (j_{Na}) and a K^+ delayed rectifier flux ($j_{\mathrm{K-DR}}$),

while the dendrite contained a voltage-dependent Ca^{2+} flux (j_{Ca}), a voltage-dependent K^+ AHP flux (j_{K-AHP}), and a Ca^{2+}-dependent K^+ flux (j_{K-C}):

$$j_{Na} = g_{Na}(\phi_{sm} - E_{Na,s})/(Fz_{Na}), \tag{25}$$
$$j_{K-DR} = g_{DR}(\phi_{sm} - E_{K,s})/(Fz_{K}), \tag{26}$$
$$j_{Ca} = g_{Ca}(\phi_{dm} - E_{Ca,d})/(Fz_{Ca}), \tag{27}$$
$$j_{K-AHP} = g_{AHP}(\phi_{dm} - E_{K,d})/(Fz_{K}), \tag{28}$$
$$j_{K-C} = g_{C}(\phi_{dm} - E_{K,d})/(Fz_{K}). \tag{29}$$

The voltage-dependent conductances were modeled using the Hodgkin–Huxley formalism with differential equations for the gating variables:

$$\frac{dx}{dt} = \alpha_x(1-x) - \beta_x x, \quad \text{with } x = m, h, n, s, c, q, \tag{30}$$
$$\frac{dz}{dt} = \frac{z_\infty - z}{\tau_z}. \tag{31}$$

The conductances and gating variables were given by:

$$g_{Na} = \bar{g}_{Na} m_\infty^2 h, \tag{32}$$
$$g_{DR} = \bar{g}_{DR} n, \tag{33}$$
$$g_{Ca} = \bar{g}_{Ca} s^2 z, \tag{34}$$
$$g_{C} = \bar{g}_{C} c \chi([Ca^{2+}]), \tag{35}$$
$$g_{AHP} = \bar{g}_{AHP} q, \tag{36}$$
$$\alpha_m = -\frac{3.2 \cdot 10^5 \cdot \phi_1}{\exp(-\phi_1/0.004) - 1}, \text{ with } \phi_1 = \phi_m + 0.0469 \tag{37}$$
$$\beta_m = \frac{2.8 \cdot 10^5 \cdot \phi_2}{\exp(\phi_2/0.005) - 1}, \text{ with } \phi_2 = \phi_m + 0.0199 \tag{38}$$
$$m_\infty = \frac{\alpha_m}{\alpha_m + \beta_m} \tag{39}$$
$$\alpha_h = 128 \exp \frac{-0.043 - \phi_m}{0.018}, \tag{40}$$
$$\beta_h = \frac{4000}{1 + \exp(-\phi_3/0.005)}, \text{ with } \phi_3 = \phi_m + 0.02 \tag{41}$$
$$\alpha_n = -\frac{1.6 \cdot 10^4 \cdot \phi_4}{\exp(-\phi_4/0.005) - 1}, \text{ with } \phi_4 = \phi_m + 0.0249 \tag{42}$$
$$\beta_n = 250 \exp(-\phi_5/0.04), \text{ with } \phi_5 = \phi_m + 0.04 \tag{43}$$
$$\alpha_s = \frac{1600}{1 + \exp(-72(\phi_m - 0.005))}, \tag{44}$$
$$\beta_s = \frac{2 \cdot 10^4 \cdot \phi_6}{\exp(\phi_6/0.005) - 1}, \text{ with } \phi_6 = \phi_m + 0.0089 \tag{45}$$
$$z_\infty = \frac{1}{1 + \exp(\phi_7/0.001)}, \text{ with } \phi_7 = \phi_m + 0.03 \tag{46}$$

$$\tau_z = 1, \tag{47}$$

$$\alpha_c = \begin{cases} 52.7 \exp\left(\frac{\phi_8}{0.011} - \frac{\phi_9}{0.027}\right), & \text{if } \phi_m \leq -0.01 \text{ V} \\ 2000 \exp(-\phi_9/0.027), & \text{otherwise} \end{cases} \tag{48}$$

$$\text{with } \phi_8 = \phi_m + 0.05 \text{ and } \phi_9 = \phi_m + 0.0535 \tag{49}$$

$$\beta_c = \begin{cases} 2000 \exp(-\phi_9/0.027) - \alpha_c, & \text{if } \phi_m \leq -0.01 \text{ V} \\ 0, & \text{otherwise} \end{cases} \tag{50}$$

$$\chi = \min(\frac{\gamma_{Ca}[Ca^{2+}] - 99.8 \cdot 10^{-6}}{2.5 \cdot 10^{-4}}, 1), \tag{51}$$

$$\alpha_q = \min(2 \cdot 10^4 (\gamma_{Ca}[Ca^{2+}] - 99.8 \cdot 10^{-6}), 10), \tag{52}$$

$$\beta_q = 1. \tag{53}$$

All these equations were taken from [8] (with errata [83]) and converted so that values are given in SI units: units for rates (α's, β's) are 1/s, unit for τ_z is s, and units for voltages ϕ are V. The equations were used in their original form, except those related to Ca^{2+} dynamics, where we made the following changes: Firstly, as a large fraction of intracellular Ca^{2+} is buffered or taken up by the ER, we multiplied $[Ca^{2+}]$ in Eqs 51 and 52 by a factor γ_{Ca}, which refers to the fraction of free Ca^{2+} within the cell, and set this to be 0.01. As $[Ca^{2+}]$ in Eqs 51 and 52 were multiplied with 0.01, only the free Ca^{2+} could affect the Ca^{2+} activated ion channels. We further assumed that only the free Ca^{2+} could move between the intracellular compartments (Eq 1) and affect the Ca^{2+} reversal potential (Eq 24). Secondly, the original PR model had an abstract and unitless variable for the intracellular Ca^{2+} concentration, with a basal concentration of 0.2, while we defined a (biophysically realistic) baseline concentration of 0.01 mM, which corresponds to a concentration of *free* Ca^{2+} of 100 nM. In Eqs 51 and 52 we therefore subtracted $99.8 \cdot 10^{-6}$ (mol/m^3) from the Ca^{2+} concentration to correct for the shift in baseline. Thirdly, we modified the voltage-dependent Ca^{2+} current to include an inactivation variable z (Eqs 31 and 34). We implemented this inactivation like they did in [84] (Eqs A2-A3), but set the time constant to 1 s, the half-activation voltage to -30 mV, and the slope of the steady-state Boltzmann fit to z_∞ to 0.001. In the original PR model, inactivation was neglected due to the argument that it was too slow to have an impact on simulation outcomes [2]. However, in our simulations, we observed that it had a significant impact, and therefore we included it.

Homeostatic mechanisms

To maintain baseline ion concentrations for low frequency activity we added $3Na^+/2K^+$ pumps, K^+/Cl^- cotransporters (KCC2), and $Na^+/K^+/2Cl^-$ cotransporters (NKCC1). Their functional forms were taken from [45].

$$j_{pump} = \frac{\rho}{1.0 + \exp((25 - [Na^+]_i)/3)} \cdot \frac{1.0}{1.0 + \exp(3.5 - [K^+]_e)}, \tag{54}$$

$$j_{\mathrm{kcc2}} = U_{\mathrm{kcc2}} \ln\left(\frac{[\mathrm{K}^+]_\mathrm{i}[\mathrm{Cl}^-]_\mathrm{i}}{[\mathrm{K}^+]_\mathrm{e}[\mathrm{Cl}^-]_\mathrm{e}}\right), \tag{55}$$

$$j_{\mathrm{nkcc1}} = U_{\mathrm{nkcc1}} f([\mathrm{K}^+]_\mathrm{e}) \left(\ln\left(\frac{[\mathrm{K}^+]_\mathrm{i}[\mathrm{Cl}^-]_\mathrm{i}}{[\mathrm{K}^+]_\mathrm{e}[\mathrm{Cl}^-]_\mathrm{e}}\right) + \ln\left(\frac{[\mathrm{Na}^+]_\mathrm{i}[\mathrm{Cl}^-]_\mathrm{i}}{[\mathrm{Na}^+]_\mathrm{e}[\mathrm{Cl}^-]_\mathrm{e}}\right)\right), \tag{56}$$

$$f([\mathrm{K}^+]_\mathrm{e}) = \frac{1}{1+\exp(16-[\mathrm{K}^+]_\mathrm{e})}, \tag{57}$$

where ρ, U_{kcc2}, and U_{nkcc1} are pump and cotransporter strengths. We assumed optimal pump functionality and set ρ to be the pump strength used in [45] for the fully oxygenated state with normal bath potassium ($\rho_{\max}$).

Intracellular Ca^{2+} decay was modeled in a similar fashion as in [3], but to ensure ion conservation we modeled it as an electroneutral $Ca^{2+}/2Na^+$ exchanger, exchanging one Ca^{2+} (outward) for two Na^+ (inward). Putatively, this phenomenological model for the decay could represent the joint effect of several mechanisms in a real system, such as the $Ca^{2+}/3Na^+$ exchanger, a Ca^{2+} leakage current, SERCA pumps, etc. The decay flux density was defined as:

$$j_{\mathrm{Ca-dec}} = U_{\mathrm{Ca-dec}}([\mathrm{Ca}^{2+}]_\mathrm{i} - [\mathrm{Ca}^{2+}]_\mathrm{i,b}) \cdot \frac{V_\mathrm{i}}{A_\mathrm{m}} \tag{58}$$

where $U_{\mathrm{Ca-dec}}$ is the decay rate, and $[\mathrm{Ca}^{2+}]_\mathrm{i,b}$ is the basal Ca^{2+} concentration, set to 0.01 mM.

Model summary

We summarize the model here for easy reference. In short, we solved four differential equations for all ion species k:

$$\frac{d[\mathrm{k}]_\mathrm{si}}{dt} = -j_{\mathrm{k,sm}} \cdot \frac{A_\mathrm{s}}{V_\mathrm{si}} - j_{\mathrm{k,i}} \cdot \frac{A_\mathrm{i}}{V_\mathrm{si}}, \tag{59}$$

$$\frac{d[\mathrm{k}]_\mathrm{di}}{dt} = -j_{\mathrm{k,dm}} \cdot \frac{A_\mathrm{d}}{V_\mathrm{di}} + j_{\mathrm{k,i}} \cdot \frac{A_\mathrm{i}}{V_\mathrm{di}}, \tag{60}$$

$$\frac{d[\mathrm{k}]_\mathrm{se}}{dt} = +j_{\mathrm{k,sm}} \cdot \frac{A_\mathrm{s}}{V_\mathrm{se}} - j_{\mathrm{k,e}} \cdot \frac{A_\mathrm{e}}{V_\mathrm{se}}, \tag{61}$$

$$\frac{d[\mathrm{k}]_\mathrm{de}}{dt} = +j_{\mathrm{k,dm}} \cdot \frac{A_\mathrm{d}}{V_\mathrm{se}} + j_{\mathrm{k,e}} \cdot \frac{A_\mathrm{e}}{V_\mathrm{de}}. \tag{62}$$

At each time step, ϕ in all four compartments was derived algebraically:

$$\phi_\mathrm{de} = 0, \tag{63}$$

$$\phi_\mathrm{di} = Q_\mathrm{di}/(c_\mathrm{m}A_\mathrm{d}) \tag{64}$$

$$\phi_\mathrm{se} = \left(\phi_\mathrm{di} - \frac{\Delta x}{\sigma_\mathrm{i}} \cdot i_{\mathrm{diff,i}} - \frac{A_\mathrm{e}\Delta x}{A_\mathrm{i}\sigma_\mathrm{i}} \cdot i_{\mathrm{diff,e}} - \frac{Q_\mathrm{si}}{c_\mathrm{m}A_\mathrm{s}}\right) / \left(1 + \frac{A_\mathrm{e}\sigma_\mathrm{e}}{A_\mathrm{i}\sigma_\mathrm{i}}\right), \tag{65}$$

$$\phi_\mathrm{si} = \frac{Q_\mathrm{si}}{c_\mathrm{m}A_\mathrm{s}} + \phi_\mathrm{se}. \tag{66}$$

The total membrane flux densities were as follows:

$$j_{\mathrm{Na,sm}} = j_{\mathrm{Na}} + j_{\mathrm{Na,leak}} + 3j_{\mathrm{pump}} + j_{\mathrm{nkcc1}} - 2j_{\mathrm{Ca-dec}}, \tag{67}$$

$$j_{\mathrm{K,sm}} = j_{\mathrm{K-DR}} + j_{\mathrm{K,leak}} - 2j_{\mathrm{pump}} + j_{\mathrm{nkcc1}} + j_{\mathrm{kcc2}}, \tag{68}$$

$$j_{\mathrm{Cl,sm}} = j_{\mathrm{Cl,leak}} + 2j_{\mathrm{nkcc1}} + j_{\mathrm{kcc2}}, \tag{69}$$

$$j_{\mathrm{Ca,sm}} = j_{\mathrm{Ca-dec}}, \tag{70}$$

$$j_{\mathrm{Na,dm}} = j_{\mathrm{Na,leak}} + 3j_{\mathrm{pump}} + j_{\mathrm{nkcc1}} - 2j_{\mathrm{Ca-dec}}, \tag{71}$$

$$j_{\mathrm{K,dm}} = j_{\mathrm{K-AHP}} + j_{\mathrm{K-C}} + j_{\mathrm{K,leak}} - 2j_{\mathrm{pump}} + j_{\mathrm{nkcc1}} + j_{\mathrm{kcc2}}, \tag{72}$$

$$j_{\mathrm{Cl,dm}} = j_{\mathrm{Cl,leak}} + 2j_{\mathrm{nkcc1}} + j_{\mathrm{kcc2}}, \tag{73}$$

$$j_{\mathrm{Ca,dm}} = j_{\mathrm{Ca}} + j_{\mathrm{Ca-dec}}. \tag{74}$$

Fig 2 summarizes the model. The parameters involved in this model and their values used in this study are listed in Tables 1-4.

Table 3. Temperature and physical constants

Parameter	Value	Reference
T (absolute temperature)	309.14 K	[45]*
F (Faraday constant)	$9.648 \cdot 10^4$ C/mol	
R (gas constant)	8.314 J/(mol K)	

* The temperature is not explicitly given in [45], but from Eq 3 in [45] we know that $\frac{RT}{F} = 26.64 \cdot 10^{-3}$ V. By using the values of R and F listed in Table 3, we get an absolute temperature of 309.14 K, corresponding to a body temperature of 36 °C.

Original Pinsky–Rinzel model

We implemented the original Pinsky–Rinzel equations from Box 8.1 in [8]. The reversal potential of the leak current, not specified in [8], was set to −68 mV to ensure a resting potential close to that of the edPR model. We also used this as the initial potentials, that is, $\phi_{\mathrm{sm},0} = -68$ mV and $\phi_{\mathrm{dm},0} = -68$ mV. The other initial conditions were $n_0 = 0.001$, $h_0 = 0.999$, $s_0 = 0.009$, $c_0 = 0.007$, $q_0 = 0.01$, and $[\mathrm{Ca}^{2+}]_0 = 0.2$, same as in [3].

Simulations

Parameterizations

The parameters listed in Tables 1-4 were used in all the simulations of the electrodiffusive Pinsky–Rinzel (edPR) model. We tuned the Ca^{2+} conductance $\bar{g}_{\mathrm{Ca}}$ manually to obtain comparable spike shapes between the edPR model and the original PR model, as well as the fraction of free Ca^{2+} inside the cell, and the coupling strength between the soma and the dendrite.

Table 4. Membrane parameters

Parameter	Value	Reference
c_{m}	$3 \cdot 10^{-2}\,\mathrm{F/m^2}$	[3, 8]
$\bar{g}_{\mathrm{Na,leak}}$	$0.247\,\mathrm{S/m^2}$	[45]
$\bar{g}_{\mathrm{K,leak}}$	$0.5\,\mathrm{S/m^2}$	[45]
$\bar{g}_{\mathrm{Cl,leak}}$	$1.0\,\mathrm{S/m^2}$	[45]
$\bar{g}_{\mathrm{Na}}$	$300\,\mathrm{S/m^2}$	[3, 8]
$\bar{g}_{\mathrm{DR}}$	$150\,\mathrm{S/m^2}$	[3, 8]
$\bar{g}_{\mathrm{Ca}}$	$118\,\mathrm{S/m^2}$	
$\bar{g}_{\mathrm{AHP}}$	$8\,\mathrm{S/m^2}$	[3, 8]
$\bar{g}_{\mathrm{C}}$	$150\,\mathrm{S/m^2}$	[3, 8]
ρ	$1.87 \cdot 10^{-6}\,\mathrm{mol/(m^2 s)}$	[45]*
U_{kcc2}	$7.0 \cdot 10^{-7}\,\mathrm{mol/(m^2 s)}$	[45]*
U_{nkcc1}	$2.33 \cdot 10^{-7}\,\mathrm{mol/(m^2 s)}$	[45]*
$U_{\mathrm{Ca-dec}}$	$75\,\mathrm{s^{-1}}$	[3, 8]

* We multiplied the original values from [45] by a conversion factor $\frac{7}{3} \cdot 10^{-6}$ m to convert the units from mM/s to mol/m^{2}s. The conversion factor equals the initial inverse surface area to volume ratio from [45].

In the edPR model, the coupling strength between the soma and dendrite was proportional to the ratio $A_{\mathrm{i}}/\Delta x$, and all model outputs depended on this ratio, and not on A_{i} or Δx in isolation. By choice, we adjusted the coupling strength by varying $A_{\mathrm{i}} = \alpha A_{\mathrm{m}}$ through adjusting the parameter α. We could have obtained the equivalent effect by varying Δx instead. The default value of α was set to 2. All simulations were run using this value, except in Fig 5C where α was set to 0.43.

In the original PR model, the coupling strength between the soma and dendrite was represented by a coupling conductance g_{c}, which had a default value of $10.5\,\mathrm{mS/cm^2}$. In Fig 5A, g_{c} was set to $2.26\,\mathrm{mS/cm^2}$.

Initial conditions

The initial conditions for the edPR model were obtained through a two-step procedure. In the first step, we specified a set of pre-calibration initial values: We set (i) the initial membrane potential, $\phi_{\mathrm{m},0}$, to $-68\,\mathrm{mV}$, (ii) the concentrations to the pre-calibrated values in Table 5, and (iii) the gating variables (Table 5) to the same initial values as in [3]. Based on the initial concentration values, we also defined (iv) a set of static intracellular and extracellular residual charges, representing negatively charged macromolecules present in real neurons. We represented these as constant concentrations ($[\mathrm{X}^-]_{\mathrm{i},0}$ and $[\mathrm{X}^-]_{\mathrm{e},0}$) of anions with charge number $z_{\mathrm{X}} = -1$ (assuming this to be the mean charge number of the real macromolecules) and diffusion constants $D_{\mathrm{X}} = 0$ (assuming immobility). The residual charges were introduced to ensure consistency between the initial membrane potential and the charge density associated with the initial ion

concentrations:

$$[X^-]_{i,0} = z_{Na}[Na^+]_{i,0} + z_K[K^+]_{i,0} + z_{Cl}[Cl^-]_{i,0} + z_{Ca}[Ca^{2+}]_{i,0} - \phi_{m,0}\frac{c_m A_m}{V_i F}, \quad (75)$$

$$[X^-]_{e,0} = z_{Na}[Na^+]_{e,0} + z_K[K^+]_{e,0} + z_{Cl}[Cl^-]_{e,0} + z_{Ca}[Ca^{2+}]_{e,0} + \phi_{m,0}\frac{c_m A_m}{V_e F}. \quad (76)$$

Table 5. Initial conditions

Variables	Pre-calibrated	Post-calibrated[1]
$\phi_{m,0}$[†]	−68 mV	−67.7 mV
$[Na^+]_{i,0}$	15 mM	16.9 mM
$[Na^+]_{e,0}$	145 mM	141.2 mM
$[K^+]_{i,0}$	140 mM	139.5 mM
$[K^+]_{e,0}$	5 mM	5.9 mM
$[Cl^-]_{i,0}$	4 mM	5.4 mM
$[Cl^-]_{e,0}$	110 mM	107.1 mM
$[Ca^{2+}]_{i,0}$	0.01 mM*	0.01 mM*
$[Ca^{2+}]_{e,0}$	1.1 mM	1.1 mM
$[X^-]_{i,0}$[‡]	151.0 mM	151.0 mM
$[X^-]_{e,0}$[‡]	42.2 mM	42.2 mM
n_0	0.001	0.0003
h_0	0.999	0.999
s_0	0.009	0.007
c_0	0.007	0.005
q_0	0.010	0.011
z_0	1.0	1.0

[1] Preciser values (with more decimals included) were read to/from file and used in the simulations. (Available at https://github.com/CINPLA/EDPRmodel_analysis.)

[†] ϕ_m is not an independent state variable, but at each time point an algebraic function of ion concentrations, as computed through the KNP formalism.

* Only 1% of the total intracellular Ca^{2+}, that is, a 100 nM, was assumed to be free (unbuffered).

[‡] Not state variables, but constants, derived (initially) from Eqs 75 and 76.

In the next step, we calibrated the model by running it for 1800 s to obtain the post-calibrated values of all the state variables (Table 5). These post-calibrated values were written to file and used as initial conditions in all simulations shown throughout this paper. For technical reasons, we did not read the constant residual concentrations, $[X^-]_{i,0}$ and $[X^-]_{e,0}$, to/from file, but re-calculated them from Eqs 75 and 76 in the beginning of each simulation to minimize rounding errors and ensure strict electroneutrality. While the

pre-calibrated initial conditions were identical in the somatic and dendritic compartment, the post-calibration values were not strictly identical, but identical up to the decimal place included in Table 5. Hence, the indicated values apply for both the soma and dendrite compartments. The post-calibrated values of the ion concentrations gave us the following reversal potentials: $E_{\mathrm{Na}} = 57\,\mathrm{mV}$, $E_{\mathrm{K}} = -84\,\mathrm{mV}$, $E_{\mathrm{Cl}} = -79\,\mathrm{mV}$, and $E_{\mathrm{Ca}} = 124\,\mathrm{mV}$.

The pre-calibration values for the ion concentrations were taken from Table 2.1 in [85], which lists the ranges of typical intra- and extracellular concentrations in mammalian neurons. From the ranges given in this table, we selected values that made the edPR model (throughout the calibration period) reside close to the selected initial membrane potential of $-68\,\mathrm{mV}$, a typical value found for CA3 pyramidal cells in adult rats [86].

Stimulus current

We stimulated the cell by injecting a K^+ current i_{stim} into the soma. Previous computational modeling of a cardiac cell has shown that stimulus with K^+ causes the least physiological disruption [33]. To ensure ion conservation, we removed the same amount of K^+ ions from the corresponding extracellular compartment:

$$\frac{d[\mathrm{K}^+]_{\mathrm{si}}}{dt} += \frac{i_{\mathrm{stim}}}{F z_{\mathrm{K}} V_{\mathrm{si}}}, \tag{77}$$

$$\frac{d[\mathrm{K}^+]_{\mathrm{se}}}{dt} -= \frac{i_{\mathrm{stim}}}{F z_{\mathrm{K}} V_{\mathrm{se}}}. \tag{78}$$

Analysis

Fig 9: To calculate the accumulative transport of ion species k in the intracellular solution (from time zero to t) due to diffusion, we integrated $A_{\mathrm{i}} N_{\mathrm{A}} j_{\mathrm{k,diff,i}}$ from time zero to t, where N_{A} is the Avogadro constant. Similarly, we integrated $A_{\mathrm{e}} N_{\mathrm{A}} j_{\mathrm{k,diff,e}}$ to calculate the accumulative transport of ions in the extracellular solution due to diffusion. We did the same calculations with $j_{\mathrm{k,drift}}$ to study the accumulative transport of ions due to drift. When knowing the accumulative transport of each ion species, $\mathrm{k}_{\mathrm{akkum}}$, we calculated the total transport of e^+ from their weighted sum:

$$\mathrm{e}^+_{\mathrm{akkum}} = z_{\mathrm{Na}}\mathrm{Na}^+_{\mathrm{akkum}} + z_{\mathrm{K}}\mathrm{K}^+_{\mathrm{akkum}} + z_{\mathrm{Cl}}\mathrm{Cl}^-_{\mathrm{akkum}} + z_{\mathrm{Ca}}\mathrm{Ca}^{2+}_{\mathrm{akkum}}. \tag{79}$$

Fig 10: To calculate $\phi_{\mathrm{VC,e}}$ and $\phi_{\mathrm{diff,e}}$, we looked at the extracellular axial current as it is given in the KNP formalism:

$$i_{\mathrm{e}} = i_{\mathrm{diff,e}} + i_{\mathrm{field,e}} = i_{\mathrm{diff,e}} + \sigma_{\mathrm{e}} \frac{\phi_{\mathrm{se}}}{\Delta x}, \tag{80}$$

where the last equality follows when we insert Eq 18 for the extracellular field-driven current density $i_{\mathrm{field,e}}$, and use that $\phi_{\mathrm{de}} = 0$. As in [32], we may split ϕ_{se} into two components:

$$\phi_{\mathrm{se}} = \phi_{\mathrm{VC,se}} + \phi_{\mathrm{diff,se}}, \tag{81}$$

where $\phi_{\mathrm{VC,se}}$ is the potential as it would be predicted from standard volume conductor (VC) theory [20, 21], and $\phi_{\mathrm{diff,se}}$ is the additional contribution from diffusion [32]. With this, Eq 80 can be written:

$$i_{\mathrm{e}} = i_{\mathrm{diff,e}} + \sigma_{\mathrm{e}} \frac{\phi_{\mathrm{VC,se}}}{\Delta x} + \sigma_{\mathrm{e}} \frac{\phi_{\mathrm{diff,se}}}{\Delta x}. \tag{82}$$

We may split this into two equations if we recognize that

$$i_{\mathrm{e}} = \sigma_{\mathrm{e}} \frac{\phi_{\mathrm{VC,se}}}{\Delta x}, \tag{83}$$

is the standard formula used in VC theory, which is based on the assumption that the extracellular current is exclusively due to a drop in the extracellular VC-potential $\phi_{\mathrm{VC,se}}$. The remainder of Eq 82 then leaves us with

$$i_{\mathrm{diff,e}} = -\sigma_{\mathrm{e}} \frac{\phi_{\mathrm{diff,se}}}{\Delta x}. \tag{84}$$

Since we already knew i_{e} and $i_{\mathrm{diff,e}}$ from simulations with the KNP framework, we used Eqs 83 and 84 to calculate $\phi_{\mathrm{VC,se}}$ and $\phi_{\mathrm{diff,se}}$ separately.

Numerical implementation

We implemented the differential equations in Python 3.6 and solved them using the `solve_ivp` function from SciPy. We used its default Runge-Kutta method of order 5(4), and set the maximal allowed step size to 10^{-4}. The code is made available at https://github.com/CINPLA/EDPRmodel and https://github.com/CINPLA/EDPRmodel_analysis.

Funding

This work was funded by the Research Council of Norway (https://www.forskningsradet.no) via the BIOTEK2021 Digital Life project 'DigiBrain', grant no 248828 (received by GTE). The funders had no role in study design, data collection and analysis, decision to publish, or preparation of the manuscript.

Competing interests

The authors have declared that no competing interests exist.

References

[1] Hodgkin, A. L. and Huxley, A. F. "A quantitative description of membrane current and its application to conduction and excitation in nerve". In: *The Journal of physiology* vol. 117, no. 4 (1952), p. 500.

[2] Traub, R. D. et al. “A model of a CA3 hippocampal pyramidal neuron incorporating voltage-clamp data on intrinsic conductances”. In: *Journal of neurophysiology* vol. 66, no. 2 (1991), pp. 635–650.

[3] Pinsky, P. F. and Rinzel, J. “Intrinsic and network rhythmogenesis in a reduced Traub model for CA3 neurons”. In: *Journal of computational neuroscience* vol. 1, no. 1-2 (1994), pp. 39–60.

[4] Mainen, Z. F. et al. “A model of spike initiation in neocortical pyramidal neurons”. In: *Neuron* vol. 15, no. 6 (1995), pp. 1427–1439.

[5] Pospischil, M. et al. “Minimal Hodgkin-Huxley type models for different classes of cortical and thalamic neurons”. In: *Biological cybernetics* vol. 99, no. 4-5 (2008), pp. 427–441.

[6] Halnes, G. et al. “A multi-compartment model for interneurons in the dorsal lateral geniculate nucleus”. In: *PLoS computational biology* vol. 7, no. 9 (2011), e1002160.

[7] Hay, E. et al. “Models of neocortical layer 5b pyramidal cells capturing a wide range of dendritic and perisomatic active properties”. In: *PLoS computational biology* vol. 7, no. 7 (2011), e1002107.

[8] Sterratt, D. et al. *Principles of computational modelling in neuroscience*. Cambridge University Press, 2011.

[9] Offner, F. F. “Ion flow through membranes and the resting potential of cells”. In: *The Journal of membrane biology* vol. 123, no. 2 (1991), pp. 171–182.

[10] Koch, C. *Biophysics of computation: information processing in single neurons*. Oxford university press, 2004.

[11] Rall, W. “Core conductor theory and cable properties of neurons”. In: *Comprehensive physiology* (2011), pp. 39–97.

[12] Tveito, A. et al. “An evaluation of the accuracy of classical models for computing the membrane potential and extracellular potential for neurons”. In: *Frontiers in computational neuroscience* vol. 11 (2017), p. 27.

[13] Traub, R. D. et al. “Single-column thalamocortical network model exhibiting gamma oscillations, sleep spindles, and epileptogenic bursts”. In: *Journal of neurophysiology* vol. 93, no. 4 (2005), pp. 2194–2232.

[14] Markram, H. et al. “Reconstruction and simulation of neocortical microcircuitry”. In: *Cell* vol. 163, no. 2 (2015), pp. 456–492.

[15] Arkhipov, A. et al. “Visual physiology of the layer 4 cortical circuit in silico”. In: *PLoS computational biology* vol. 14, no. 11 (2018), e1006535.

[16] Buzsáki, G., Anastassiou, C. A., and Koch, C. “The origin of extracellular fields and currents–EEG, ECoG, LFP and spikes”. In: *Nature reviews neuroscience* vol. 13, no. 6 (2012), p. 407.

[17] Einevoll, G. T. et al. “Modelling and analysis of local field potentials for studying the function of cortical circuits”. In: *Nature reviews neuroscience* vol. 14, no. 11 (2013), pp. 770–785.

[18] Hagen, E. et al. “Multimodal modeling of neural network activity: computing LFP, ECoG, EEG and MEG signals with LFPy 2.0”. In: *Frontiers in neuroinformatics* vol. 12 (2018), p. 92.

[19] Anastassiou, C. A. and Koch, C. “Ephaptic coupling to endogenous electric field activity: why bother?” In: *Current opinion in neurobiology* vol. 31 (2015), pp. 95–103.

[20] Holt, G. R. and Koch, C. “Electrical interactions via the extracellular potential near cell bodies”. In: *Journal of computational neuroscience* vol. 6, no. 2 (1999), pp. 169–184.

[21] Pettersen, K. H. and Einevoll, G. T. “Amplitude variability and extracellular low-pass filtering of neuronal spikes”. In: *Biophysical journal* vol. 94, no. 3 (2008), pp. 784–802.

[22] Somjen, G. G. “Mechanisms of spreading depression and hypoxic spreading depression-like depolarization”. In: *Physiological reviews* vol. 81, no. 3 (2001), pp. 1065–1096.

[23] Fröhlich, F. and Bazhenov, M. “Potassium dynamics in the epileptic cortex: new insights on an old topic”. In: *Neuroscientist* vol. 14, no. 5 (2008), pp. 422–433.

[24] Zandt, B.-J. et al. “How does spreading depression spread? Physiology and modeling”. In: *Reviews in the Neurosciences* vol. 26, no. 2 (2015), pp. 183–198.

[25] Ayata, C. and Lauritzen, M. “Spreading depression, spreading depolarizations, and the cerebral vasculature”. In: *Physiological reviews* vol. 95, no. 3 (2015), pp. 953–993.

[26] Herreras, O. and Somjen, G. “Analysis of potential shifts associated with recurrent spreading depression and prolonged unstable spreading depression induced by microdialysis of elevated K^+ in”. In: *Brain research* vol. 610, no. 2 (1993), pp. 283–294.

[27] Kager, H., Wadman, W. J., and Somjen, G. G. “Simulated seizures and spreading depression in a neuron model incorporating interstitial space and ion concentrations”. In: *Journal of neurophysiology* vol. 84, no. 1 (2000), pp. 495–512.

[28] Barreto, E. and Cressman, J. R. “Ion concentration dynamics as a mechanism for neuronal bursting”. In: *Journal of biological physics* vol. 37, no. 3 (2011), pp. 361–373.

[29] Øyehaug, L. et al. “Dependence of spontaneous neuronal firing and depolarisation block on astroglial membrane transport mechanisms”. In: *Journal of computational neuroscience* vol. 32, no. 1 (2012), pp. 147–165.

[30] Mori, Y. “A multidomain model for ionic electrodiffusion and osmosis with an application to cortical spreading depression”. In: *Physica D: Nonlinear phenomena* vol. 308 (2015), pp. 94–108.

[31] Halnes, G. et al. “Effect of ionic diffusion on extracellular potentials in neural tissue”. In: *PLoS computational biology* vol. 12, no. 11 (2016), e1005193.

[32] Solbrå, A. et al. “A Kirchhoff-Nernst-Planck framework for modeling large scale extracellular electrodiffusion surrounding morphologically detailed neurons”. In: *PLoS computational biology* vol. 14, no. 10 (2018), e1006510.

[33] Kneller, J. et al. “Time-dependent transients in an ionically based mathematical model of the canine atrial action potential”. In: *American journal of physiology-heart and circulatory physiology* vol. 282, no. 4 (2002), H1437–H1451.

[34] Somjen, G., Kager, H., and Wadman, W. “Computer simulations of neuron-glia interactions mediated by ion flux”. In: *Journal of computational neuroscience* vol. 25, no. 2 (2008), pp. 349–365.

[35] Florence, G. et al. “The role of extracellular potassium dynamics in the different stages of ictal bursting and spreading depression: a computational study”. In: *Journal of theoretical biology* vol. 258, no. 2 (2009), pp. 219–28.

[36] Cressman, J. R. et al. “The influence of sodium and potassium dynamics on excitability, seizures, and the stability of persistent states: I. Single neuron dynamics”. In: *Journal of computational neuroscience* vol. 26, no. 2 (2009), pp. 159–170.

[37] Ullah, G. et al. “The influence of sodium and potassium dynamics on excitability, seizures, and the stability of persistent states: II. Network and glial dynamics”. In: *Journal of computational neuroscience* vol. 26, no. 2 (2009), pp. 171–183.

[38] Lee, J. and Kim, S. J. “Spectrum measurement of fast optical signal of neural activity in brain tissue and its theoretical origin”. In: *Neuroimage* vol. 51, no. 2 (2010), pp. 713–722.

[39] Lee, J., Boas, D. A., and Kim, S. J. “Multiphysics neuron model for cellular volume dynamics”. In: *IEEE Transactions on biomedical engineering* vol. 58, no. 10 (2011), pp. 3000–3003.

[40] Zandt, B.-J. et al. “Neural dynamics during anoxia and the “wave of death””. In: *PLoS one* vol. 6, no. 7 (2011), e22127.

[41] Hübel, N., Schöll, E., and Dahlem, M. A. “Bistable dynamics underlying excitability of ion homeostasis in neuron models”. In: *PLoS computational biology* vol. 10, no. 5 (2014), e1003551.

[42] Dahlem, M. A., Schumacher, J., and Hübel, N. “Linking a genetic defect in migraine to spreading depression in a computational model”. In: *PeerJ* vol. 2 (2014), e379.

[43] Hübel, N. and Dahlem, M. A. “Dynamics from seconds to hours in Hodgkin-Huxley model with time-dependent ion concentrations and buffer reservoirs”. In: *PLoS computational biology* vol. 10, no. 12 (2014), e1003941.

[44] Wei, Y. et al. “Oxygen and seizure dynamics: II. Computational modeling”. In: *Journal of neurophysiology* vol. 112, no. 2 (2014), pp. 213–223.

[45] Wei, Y., Ullah, G., and Schiff, S. J. “Unification of neuronal spikes, seizures, and spreading depression”. In: *Journal of neuroscience* vol. 34, no. 35 (2014), pp. 11733–11743.

[46] Hübel, N. and Ullah, G. “Anions govern cell volume: a case study of relative astrocytic and neuronal swelling in spreading depolarization”. In: *PLoS one* vol. 11, no. 3 (2016), e0147060.

[47] Hübel, N. et al. “The role of glutamate in neuronal ion homeostasis: A case study of spreading depolarization”. In: *PLoS computational biology* vol. 13, no. 10 (2017), e1005804.

[48] Kager, H., Wadman, W., and Somjen, G. “Conditions for the triggering of spreading depression studied with computer simulations”. In: *Journal of neurophysiology* vol. 88, no. 5 (2002), pp. 2700–2712.

[49] Cataldo, E. et al. “Computational model of touch sensory cells (T Cells) of the leech: role of the afterhyperpolarization (AHP) in activity-dependent conduction failure”. In: *Journal of computational neuroscience* vol. 18, no. 1 (2005), pp. 5–24.

[50] Kager, H., Wadman, W., and Somjen, G. “Seizure-like afterdischarges simulated in a model neuron”. In: *Journal of computational neuroscience* vol. 22, no. 2 (2007), pp. 105–128.

[51] Forrest, M. D. et al. “The sodium-potassium pump controls the intrinsic firing of the cerebellar Purkinje neuron”. In: *PLoS one* vol. 7, no. 12 (2012), e51169.

[52] Chang, J. C. et al. “A mathematical model of the metabolic and perfusion effects on cortical spreading depression”. In: *PLoS one* vol. 8, no. 8 (2013), e70469.

[53] Le Masson, G., Przedborski, S., and Abbott, L. “A computational model of motor neuron degeneration”. In: *Neuron* vol. 83, no. 4 (2014), pp. 975–988.

[54] Forrest, M. D. “Simulation of alcohol action upon a detailed Purkinje neuron model and a simpler surrogate model that runs $>$ 400 times faster”. In: *BMC neuroscience* vol. 16, no. 1 (2015), p. 27.

[55] Krishnan, G. P. et al. “Electrogenic properties of the Na^+/K^+ ATPase control transitions between normal and pathological brain states”. In: *Journal of neurophysiology* vol. 113, no. 9 (2015), pp. 3356–3374.

[56] Zylbertal, A. et al. “Prolonged intracellular Na^+ dynamics govern electrical activity in accessory olfactory bulb mitral cells”. In: *PLoS biology* vol. 13, no. 12 (2015), e1002319.

[57] Zylbertal, A., Yarom, Y., and Wagner, S. “The slow dynamics of intracellular sodium concentration increase the time window of neuronal integration: A simulation study”. In: *Frontiers in computational neuroscience* vol. 11 (2017), p. 85.

[58] Qian, N., Sejnowski, T. J., and Diego, S. "An electro-diffusion model for computing membrane potentials and ionic concentrations in branching dendrites, spines and axons". In: *Biological cybernetics* vol. 15, no. 1 (1989), pp. 1–15.

[59] Mori, Y. and Peskin, C. "A numerical method for cellular electrophysiology based on the electrodiffusion equations with internal boundary conditions at membranes". In: *Communications in applied mathematics and computational science* vol. 4, no. 1 (2009), pp. 85–134.

[60] Halnes, G. et al. "Electrodiffusive model for astrocytic and neuronal ion concentration dynamics". In: *PLoS computational biology* vol. 9, no. 12 (2013), e1003386.

[61] Niederer, S. "Regulation of ion gradients across myocardial ischemic border zones: a biophysical modelling analysis". In: *PLoS one* vol. 8, no. 4 (2013), e60323.

[62] Ellingsrud, A. J. et al. "Finite element simulation of ionic electrodiffusion in cellular geometries". In: *Frontiers in neuroinformatics* vol. 14 (2020), p. 11.

[63] Attwell, D. and Laughlin, S. B. "An energy budget for signaling in the grey matter of the brain". In: *Journal of cerebral blood flow & metabolism* vol. 21, no. 10 (2001), pp. 1133–1145.

[64] Yi, G., Fan, Y., and Wang, J. "Metabolic cost of dendritic Ca^{2+} action potentials in layer 5 pyramidal neurons". In: *Frontiers in neuroscience* vol. 13 (2019).

[65] "Depolarization Block". In: *Encyclopedia of Neuroscience*. Ed. by Binder, M. D., Hirokawa, N., and Windhorst, U. Springer Berlin Heidelberg, 2009, pp. 943–944.

[66] Mizuseki, K. et al. "Activity dynamics and behavioral correlates of CA3 and CA1 hippocampal pyramidal neurons". In: *Hippocampus* vol. 22, no. 8 (2012), pp. 1659–1680.

[67] Gardner-Medwin, A. "Analysis of potassium dynamics in mammalian brain tissue". In: *The Journal of physiology* vol. 335, no. 1 (1983), pp. 393–426.

[68] Reiffurth, C. et al. "Na^+/K^+-ATPase α isoform deficiency results in distinct spreading depolarization phenotypes". In: *Journal of cerebral blood flow & metabolism* vol. 40, no. 3 (2020), pp. 622–638.

[69] Nelson, P. *Biological physics*. WH Freeman New York, 2004.

[70] Van Rijn, C. M. et al. "Decapitation in rats: latency to unconsciousness and the "wave of death"". In: *PLoS one* vol. 6, no. 1 (2011), e16514.

[71] McDougal, R. A., Hines, M. L., and Lytton, W. W. "Reaction-diffusion in the NEURON simulator". In: *Frontiers in neuroinformatics* vol. 7 (2013), p. 28.

[72] Hines, M., Davison, A. P., and Muller, E. "NEURON and Python". In: *Frontiers in neuroinformatics* vol. 3 (2009), p. 1.

[73] Halnes, G. et al. “Ion diffusion may introduce spurious current sources in current-source density (CSD) analysis”. In: *Journal of neurophysiology* vol. 118, no. 1 (2017), pp. 114–120.

[74] Gratiy, S. L. et al. “From Maxwell’s equations to the theory of current-source density analysis”. In: *European journal of neuroscience* vol. 45, no. 8 (2017), pp. 1013–1023.

[75] Rall, W. “Core conductor theory and cable properties of neurons”. In: *Handbook of physiology*. Ed. by Kandel, E., Brookhardt, J., and Mountcastle V.M. Bethesda: American Physiological Society, 1977. Chap. 3, pp. 39–97.

[76] O’Connell, R. and Mori, Y. “Effects of glia in a triphasic continuum model of cortical spreading depression”. In: *Bulletin of mathematical biology* vol. 78, no. 10 (2016), pp. 1943–1967.

[77] Tuttle, A., Riera Diaz, J., and Mori, Y. “A computational study on the role of glutamate and NMDA receptors on cortical spreading depression using a multidomain electrodiffusion model”. In: *PLoS computational biology* vol. 15, no. 12 (2019).

[78] Eisenberg, R. S. and Johnson, E. A. “Three-dimensional electrical field problems in physiology”. In: *Progress in biophysics and molecular biology* vol. 20 (1970), pp. 1–65.

[79] Henriquez, C. S. “Simulating the electrical behavior of cardiac tissue using the bidomain model”. In: *Critical reviews in biomedical engineering* vol. 21, no. 1 (1993), pp. 1–77.

[80] Sundnes, J. et al. “On the computational complexity of the bidomain and the monodomain models of electrophysiology”. In: *Annals of biomedical engineering* vol. 34, no. 7 (2006), pp. 1088–1097.

[81] Chen, K. C. and Nicholson, C. “Spatial buffering of potassium ions in brain extracellular space”. In: *Biophysical journal* vol. 78, no. 6 (2000), pp. 2776–2797.

[82] Lyshevski, S. E. *Nano and molecular electronics handbook*. CRC Press, 2016.

[83] *Errata, Principles of computational modelling in neuroscience*. http://www.compneuroprinciples.org/errata. Accessed: 2020-01-04.

[84] Wolf, J. A. et al. “NMDA/AMPA ratio impacts state transitions and entrainment to oscillations in a computational model of the nucleus accumbens medium spiny projection neuron”. In: *Journal of neuroscience* vol. 25, no. 40 (2005), pp. 9080–9095.

[85] Purves, D. et al. *Neuroscience*. Sinauer Associates, Inc.: Sunderland, MA, 2012.

[86] Tyzio, R. et al. “Membrane potential of CA3 hippocampal pyramidal cells during postnatal development”. In: *Journal of neurophysiology* vol. 90, no. 5 (2003), pp. 2964–2972.

Paper III

Spatially resolved estimation of metabolic oxygen consumption from optical measurements in cortex

Marte J. Sætra[1,2], Andreas V. Solbrå[1,2], Anna Devor[3,4], Sava Sakadžić[4], Anders M. Dale[5,6], Gaute T. Einevoll[1,2,7]

1 Centre for Integrative Neuroplasticity, University of Oslo, Oslo, Norway
2 Department of Physics, University of Oslo, Oslo, Norway
3 Department of Biomedical Engineering, Boston University, Boston, Massachusets, United States
4 Athinoula A. Martinos Center for Biomedical Imaging, Massachusetts General Hospital and Harvard Medical School, Charlestown, Massachusetts, United States
5 Department of Radiology, University of California San Diego, La Jolla, California, United States
6 Department of Neurosciences, University of California San Diego, La Jolla, California, United States
7 Faculty of Science and Technology, Norwegian University of Life Sciences, Ås, Norway

Published in *Neurophotonics* vol. 7, no. 3 (2020), 035005. https://doi.org/10.1117/1.NPh.7.3.035005

Abstract

Significance: The cerebral metabolic rate of oxygen ($CMRO_2$) is an important indicator of brain function and pathology. Knowledge about its magnitude is also required for proper interpretation of the blood oxygenation level-dependent signal measured with functional MRI. Despite the need for estimating $CMRO_2$, no gold standard exists. Traditionally, the estimation of $CMRO_2$ has been pursued with somewhat indirect approaches combining several different types of measurements with mathematical modeling of the underlying physiological processes. The recent ability to

gaute.einevoll@nmbu.no

measure the level of oxygen (pO_2) in cortex with two-photon resolution in *in vivo* conditions has provided a more direct way for estimating $CMRO_2$, but has so far only been used to estimate the average $CMRO_2$ close to cortical penetrating arterioles in rats.

Aim: The aim of this study was to propose a method to provide spatial maps of $CMRO_2$ based on two-photon pO_2 measurements.

Approach: The method has two key steps. First, the pO_2 maps are spatially smoothed to reduce the effects of noise in the measurements. Next, the Laplace operator (a double spatial derivative) in two spatial dimensions is applied on the smoothed pO_2 maps to obtain spatially resolved $CMRO_2$ estimates.

Result: The smoothing introduces a bias, and a balance must be found where the effects of the noise are sufficiently reduced without introducing too much bias. In this model-based study, we explored this balance using synthetic model-based data, that is, data where the spatial maps of $CMRO_2$ were preset and thus known. The corresponding pO_2 maps were found by solving the Poisson equation, which relates $CMRO_2$ and pO_2. MATLAB code for using the method is provided.

Conclusion: Through this model-based study, we propose a new method for estimating $CMRO_2$ with high spatial resolution based on measurements of pO_2 in cerebral cortex.

Introduction

The level of consumption of oxygen by metabolic processes, that is, the cerebral metabolic rate of oxygen ($CMRO_2$), is an important indicator of brain function and pathology. Further, knowledge about the magnitude of the $CMRO_2$ is required for a proper interpretation of the blood oxygenation level-dependent signal measured in functional MRI studies [1]. The ability to measure $CMRO_2$ with high spatial and temporal resolution in cortex is thus crucial. Traditionally, the $CMRO_2$ has been estimated from several different types of measurements combined with mathematical modeling of the underlying physiological processes [1]. Given the numerous assumptions and experimental limitations typically involved, questions have been raised about the accuracy of the estimates of the $CMRO_2$ provided by these complex and somewhat indirect approaches [2].

The possibility to optically measure the partial pressure of oxygen (pO_2) around cortical diving arterioles with two-photon resolution *in vivo* [3] has provided a more direct way to estimate the $CMRO_2$. Previously, we (Sakadžić, Devor, and collaborators) used measured pO_2 gradients around diving arterioles in rats to estimate the average $CMRO_2$ in the vessel's vicinity, that is, within a radius of $\sim 100\,\mu$m [4]. We based our estimates on the Krogh–Erlang formula relating the pO_2 to the $CMRO_2$ in a cylinder section around an arteriole providing the brain tissue with oxygen [5, 6].

The Krogh–Erlang formula assumes the pO_2 level to have reached a stationary state, so that the fundamental equation relating the pO_2 and the $CMRO_2$ in the

neural tissue can be described by the Poisson equation:

$$\nabla^2 P(\mathbf{r}) = M(\mathbf{r}), \tag{1}$$

where $P(\mathbf{r})$ represents pO_2 measured at the position $\mathbf{r}$, and $M(\mathbf{r})$ is a measure that encapsulates the local $CMRO_2$. The Krogh–Erlang formula gives a specific solution to the forward problem of this partial differential equation, that is, the radial profile of P, for the case where (i) the $CMRO_2$ ($M(\mathbf{r})$) is assumed to be a constant, and (ii) all the oxygen provided by the center arteriole is assumed to be consumed within a radial distance R_t.

The problem of estimating $M(\mathbf{r})$ based on measured pO_2 profiles $P(\mathbf{r})$ is referred to as the inverse problem. In Ref. [4], this inverse problem was solved by fitting the Krogh–Erlang formula to pO_2 data obtained in the close vicinity of a penetrating cerebral arteriole. This approach is global in the sense that it uses all measurements within a radial distance R_t to obtain an estimate for an assumed constant value of M.

In this paper, we present a different approach to estimating M based on the same kind of two-photon pO_2 measurements. The solution of inverse source problems for systems described by differential equations is important in many fields of science and technology and has consequently received substantial attention from mathematicians [7]. Equation 1 is known as the Poisson equation, and several approaches have been taken to solve the inverse Poisson problem in different science and engineering contexts, see, for example, Refs. [8–11]. In the present study, we develop an approach to the inverse Poisson problem in the context of $CMRO_2$ estimation. Specifically, we solve the problem by applying the Laplace operator ∇^2 directly to suitably smoothed pressure maps $P(\mathbf{r})$ to obtain a measure of $M(\mathbf{r})$. We will refer to this approach as the diffusion-operator method for $CMRO_2$ estimation. Unlike the Krogh–Erlang method, the diffusion-operator method provides a spatially resolved map of $CMRO_2$ estimates around the arterioles and is thus not restricted to estimating an assumed constant value of M. Further, the diffusion-operator method is not restricted to situations with radially symmetric pO_2 maps as when a single arteriole provides all oxygen.

The double spatial derivatives in the Laplace operator make the diffusion-operator method inherently very sensitive to noise in the measured spatial pO_2 maps. In order to have a practical method for $CMRO_2$ estimation, we smooth the experimental data in two dimensions (2D) before application of the Laplace operator to reduce the effects of the noise. Smoothing introduces a bias, that is, a systematic error in the estimates, and a balance must be found where the effects of the noise are sufficiently reduced without introducing too much bias. In the present model-based study we explore this balance by examining the accuracy of $CMRO_2$ estimates in situations where the ground truth, that is, spatial maps of $M(\mathbf{r})$ are preset and thus known, and the corresponding maps of $P(\mathbf{r})$ are found by solving the forward problem of Eq. 1, either numerically or by taking advantage of the Krogh–Erlang formula.

The manuscript is organized as follows: In the Methods section we describe the diffusion-operator method, the methods used to provide model-based pO_2

maps used in the method validation, and the metrics used to quantify the accuracy of the resulting estimates. In the Results section we first illustrate the method and the necessary compromise between reducing noise and limiting bias when choosing the level of spatial smoothing. Next, we systematically explore the accuracy of $CMRO_2$ estimates for a variety of situations with different levels of noise, different grid sizes of the pO_2 measurement, and different levels of smoothing. In these systematic explorations of the efficacy of the method, the simple single-arteriole situation where the Krogh–Erlang formula gives the ground truth, is considered for simplicity. Later, we illustrate the use of the diffusion-operator method in more complicated situations where several arterioles provide the consumed oxygen, or the $CMRO_2$ varies with position. In the Discussion section we discuss the diffusion-operator method and its further development and use.

Methods

Mathematical modeling of $CMRO_2$ and pO_2

The blood-tissue O_2 transport is thought to be dominated by diffusion [12]. The relationship between pO_2 values denoted as $P(\mathbf{r}, t)$ and the net rate of oxygen consumption $s(\mathbf{r}, t)$ in the tissue can then, in the general case, be described by [6, 12]:

$$\frac{\partial P(\mathbf{r}, t)}{\partial t} = D\nabla^2 P(\mathbf{r}, t) + \frac{s(\mathbf{r}, t)}{\alpha}. \tag{2}$$

In Eq. 2, ∇^2 is the Laplace operator in three spatial dimensions (3D). Further, D and α are the diffusion coefficient and solubility, respectively, of oxygen in the tissue. They are assumed to be space-invariant. If warranted, Eq. 2 can be generalized to the case where D depends on position and direction, or when α varies with position [12].

Eq. 2 is only applicable outside the arterioles supplying the oxygen to the brain tissue. In the context of this equation, the oxygen supplied to the tissue is represented by a boundary condition of pO_2 imposed at the vessel wall of the arteriole. Note, however, that the effect of an oxygen supply from a bed of small capillary vessels located some distance away from the arteriole may be incorporated in the description. Such an oxygen supply will offset (or even reverse the sign of) the net rate of oxygen consumption $s(\mathbf{r}, t)$ in this region.

In the present paper, we will focus on a special case of this diffusion problem where (i) the system is in a steady-state so that the term $\partial P(\mathbf{r}, t)/\partial t$ can be neglected and (ii) there is no variation of pO_2 in the vertical z-direction, that is, the direction along the cortical axis parallel to the penetrating arteriole. These assumptions are also incorporated in the Krogh–Erlang model used to estimate the $CMRO_2$ in Ref. [4]. In this case, the diffusion equation (Eq. 2) simplifies to

$$\nabla^2 P(\mathbf{r}) = \frac{s(\mathbf{r})}{D\alpha}, \tag{3}$$

where ∇^2 now refers to the 2D Laplace operator (which with cartesian coordinates reads $\nabla^2 = \partial^2/\partial x^2 + \partial^2/\partial y^2$). Equation 3 can be written more compactly as

$$\nabla^2 P(\mathbf{r}) = M(\mathbf{r}), \tag{4}$$

where

$$M(\mathbf{r}) \equiv s(\mathbf{r})/D\alpha. \tag{5}$$

Here $M(\mathbf{r})$ is a new position-dependent variable encapsulating the net rate of oxygen consumption in the neural tissue. In principle, Eq. 4 describes the spatial map of pO_2 for any set of oxygen sinks (metabolic consumption, $s(\mathbf{r}) > 0$) and sources (i.e., oxygen provided by small capillaries, $s(\mathbf{r}) < 0$). The variable $M(\mathbf{r})$ is then proportional to the net rate of oxygen consumption, that is, the difference between oxygen sinks and sources at position $\mathbf{r}$ in tissue.

By introducing a characteristic length r^* and a characteristic oxygen consumption M^*, we can rewrite Eq. 4 in a dimensionless form which is useful in the further analysis:

$$\hat{\nabla}^2 \hat{P}(\hat{\mathbf{r}}) = \hat{M}(\hat{\mathbf{r}}). \tag{6}$$

In Eq. 6, $\hat{\mathbf{r}} = \mathbf{r}/r^*$, $\hat{P} = P/(M^* r^{*2})$, $\hat{M} = M/M^*$, and $\hat{\nabla}^2$ is the Laplace operator in terms of the dimensionless position variables. In this dimensionless form, the number of model parameters is effectively reduced by one, making the further analysis simpler.

Inverse problem of estimating $CMRO_2$ from pO_2 measurements

We estimate $CMRO_2$ by solving the inverse diffusion problem, that is, the problem where $P(\mathbf{r})$ is known from experiments, and the net rate of oxygen consumption $s(\mathbf{r}, t)$ is the unknown function of interest. It follows from Eq. 2 that $s(\mathbf{r}, t)$ based on pO_2 measurements $P_{\text{data}}(\mathbf{r}, t)$ is given by:

$$s_{\text{est}}(\mathbf{r}, t) = \alpha \frac{\partial P_{\text{data}}(\mathbf{r}, t)}{\partial t} + \alpha D \nabla^2 P_{\text{data}}(\mathbf{r}, t). \tag{7}$$

For the stationary 2D case, this reduces to

$$s_{\text{est}}(\mathbf{r}) = \alpha D \, \nabla^2 P_{\text{data}}(\mathbf{r}), \tag{8}$$

or

$$M_{\text{est}}(\mathbf{r}) = \nabla^2 P_{\text{data}}(\mathbf{r}), \tag{9}$$

where ∇^2 is the Laplace operator in 2D.

Equation 9 says that given a data set of oxygen partial pressure P_{data} measured on a 2D spatial grid, M can be estimated by taking the Laplacian of P_{data} (or in practice, a smoothed version of P_{data}). We refer to this approach as the diffusion-operator method for $CMRO_2$ estimation. If one wants estimates for s_{est}, values of the diffusion coefficient D and the solubility α are also required.

The double spatial derivatives in the Laplace operator make the diffusion-operator method inherently very sensitive to noise in the measured spatial pO_2 profiles. Thus to reduce adverse effects of noise in the pO_2 measurements, we pursue a method that spatially smooths P_{data} before application of the Laplace operator.

Smoothing of pO_2 data

To smooth pressure data, we performed cubic smoothing spline interpolation using the `csaps` function in MATLAB's Curve Fitting Toolbox. The function minimizes the square deviation between the estimated and measured 2D data (so-called L2 norm) while penalizing large double-spatial derivatives in the smoothed data. Other smoothing procedures could have been pursued instead, but a key motivation for this particular choice was the public availability of the tool.

In terms of dimensionless quantities, the `csaps` function takes a given data set $\hat{P}_{\mathrm{data}}(\hat{x},\hat{y})$ and generates a smoothing spline $\hat{P}_{\mathrm{smooth}}(\hat{x},\hat{y})$ that minimizes

$$(1-q)\sum_{i=1}^{n}\sum_{j=1}^{m}\left[\hat{P}_{\mathrm{data}}(\hat{x}_i,\hat{y}_j)-\hat{P}_{\mathrm{smooth}}(\hat{x}_i,\hat{y}_j)\right]^2+ q\iint\left[\left(\frac{\partial^2\hat{P}_{\mathrm{smooth}}(\hat{x},\hat{y})}{\partial\hat{x}^2}\right)^2+\left(\frac{\partial^2\hat{P}_{\mathrm{smooth}}(\hat{x},\hat{y})}{\partial\hat{y}^2}\right)^2\right]d\hat{x}\,d\hat{y}. \quad (10)$$

Here n and m are the number of entries of $\hat{x}$ and $\hat{y}$ respectively, and q is a smoothing parameter between 0 and 1. $q=0$ corresponds to the case with no smoothing, and increasing values of q imply increasing the amount of smoothing. Note that the `csaps` function takes $p=1-q$ as input argument, see MATLAB documentation. This MATLAB function allows for giving more weights to some data points than others in the optimization. We keep the weights identical to 1 for all data points in the present application.

The `csaps` function allows the smoothing spline $\hat{P}_{\mathrm{smooth}}$ to be computed with higher resolution than the spatial resolution of the measurements. This is convenient as it allows for a higher spatial resolution in the maps of estimated M obtained from the discrete Laplace function `del2`. Assuming that the measurements are taken in a rectangular grid of points [13], we here refer to the grid spacing between the pressure data points as $\hat{d}_{\mathrm{data}}$, and the grid spacing of the estimated pressure points $\hat{P}_{\mathrm{smooth}}$ as $\hat{d}_{\mathrm{est}}$. In the smoothing function, $\hat{d}_{\mathrm{est}}$ is set by inserting position vectors for the estimation points $\hat{x}_{\mathrm{est}}$ and $\hat{y}_{\mathrm{est}}$ with this spacing. Likewise, $\hat{d}_{\mathrm{data}}$ is set by inserting position vectors for the data points $\hat{x}$ and $\hat{y}$ with this spacing. Then $\hat{P}_{\mathrm{smooth}}$ is estimated from the recorded pressure by the following call of `csaps`:

$$\hat{P}_{\mathrm{smooth}}=\texttt{csaps}(\{\hat{y},\hat{x}\},\hat{P},(1-q),\{\hat{y}_{\mathrm{est}},\hat{x}_{\mathrm{est}}\}). \quad (11)$$

In this paper, we keep a fixed small value of $\hat{d}_{\mathrm{est}}$, that is, $\hat{d}_{\mathrm{est}}=0.001$, to minimize the error introduced from the discreteness of the Laplace operator used in the estimator presented in the next section. With this choice, the discreteness error is negligible far away from the arteriole and much smaller than other estimation errors close to the arteriole.

Application of Laplace operator

After the smoothing procedure, the net oxygen consumption as described by $\hat{M}(\hat{x}, \hat{y})$ can be estimated directly by application of the Laplace operator:

$$\hat{M}_{\mathrm{est}}(\hat{x}, \hat{y}) = \hat{\nabla}^2 \hat{P}_{\mathrm{smooth}}(\hat{x}, \hat{y}). \tag{12}$$

With $\hat{P}_{\mathrm{smooth}}$ given on a square (or rectangular) grid with grid spacing $\hat{d}$, we apply the discrete finite difference approximation of the Laplace operator:

$$\hat{M}_{\mathrm{est}}(\hat{x}_{\mathrm{i}}, \hat{y}_{\mathrm{j}}) = \frac{\hat{P}_{\mathrm{smooth}}(\hat{x}_{\mathrm{i}+1}, \hat{y}_{\mathrm{j}}) + \hat{P}_{\mathrm{smooth}}(\hat{x}_{\mathrm{i}-1}, \hat{y}_{\mathrm{j}}) + \hat{P}_{\mathrm{smooth}}(\hat{x}_{\mathrm{i}}, \hat{y}_{\mathrm{j}+1}) + \hat{P}_{\mathrm{smooth}}(\hat{x}_{\mathrm{i}}, \hat{y}_{\mathrm{j}-1}) - 4\hat{P}_{\mathrm{smooth}}(\hat{x}_{\mathrm{i}}, \hat{y}_{\mathrm{j}})}{\hat{d}^2}. \tag{13}$$

Here the integers i and j represent the grid point positions, that is, $\hat{x}_{\mathrm{i}} = i\hat{d}$ and $\hat{y}_{\mathrm{j}} = j\hat{d}$. In the present application, the MATLAB function `del2` is used to compute this discrete finite difference approximation of the Laplace operator. Note that in order to calculate the right-hand side of Eq. 13, one must multiply the output from `del2` by 4. Specifically, we use the command `4*del2(`$\hat{P}_{\mathrm{smooth}}, \hat{d}$`)` to calculate $\hat{M}_{\mathrm{est}}(\hat{x}, \hat{y})$.

Choice of smoothing parameter

The effect of the `csaps` smoothing function can be characterized by a smoothing length $\hat{d}_{\mathrm{q}}$ which describes how much a spatial δ-function is smeared out in space. By numerical exploration, we found that this characteristic smoothing length depends on q and $\hat{d}_{\mathrm{data}}$ through the relationship

$$\hat{d}_{\mathrm{q}} = k(q\hat{d}_{\mathrm{data}})^{1/4}, \tag{14}$$

where k is a constant.

This relationship was found numerically by smoothing a square single-entry matrix with one as the center element, and the rest of the elements set to zero. The resulting spatially-smoothed δ-function was then plotted, for a fixed value of $\hat{d}_{\mathrm{data}}$ and different values of q, as a function of the distance r to the center point, as shown in Fig. 1A. We then defined the characteristic length $\hat{d}_{\mathrm{q}}$ to be the distance from the center point at which the function value had fallen 50% compared to the center value, see dotted lines in panel A. Panel B shows the dependence of the estimated $\hat{d}_{\mathrm{q}}$ on q (for a fixed $\hat{d}_{\mathrm{data}}$ of 0.005). We observe that $\hat{d}_{\mathrm{q}}$ increases slowly with q, that is, when q is increased by a factor 10^4, $\hat{d}_{\mathrm{q}}$ increases only by a factor 10. Fig. 1C shows the smoothed δ-function when instead the value of q is fixed, while $\hat{d}_{\mathrm{data}}$ has different values. Again, when $\hat{d}_{\mathrm{q}}$ is read out from the curve and plotted as a function of $\hat{d}_{\mathrm{data}}$ (panel D), we see that $\hat{d}_{\mathrm{q}}$ increases slowly with $\hat{d}_{\mathrm{data}}$, that is, when $\hat{d}_{\mathrm{data}}$ is increased by a factor 10^4, $\hat{d}_{\mathrm{q}}$ increases only by a factor 10.

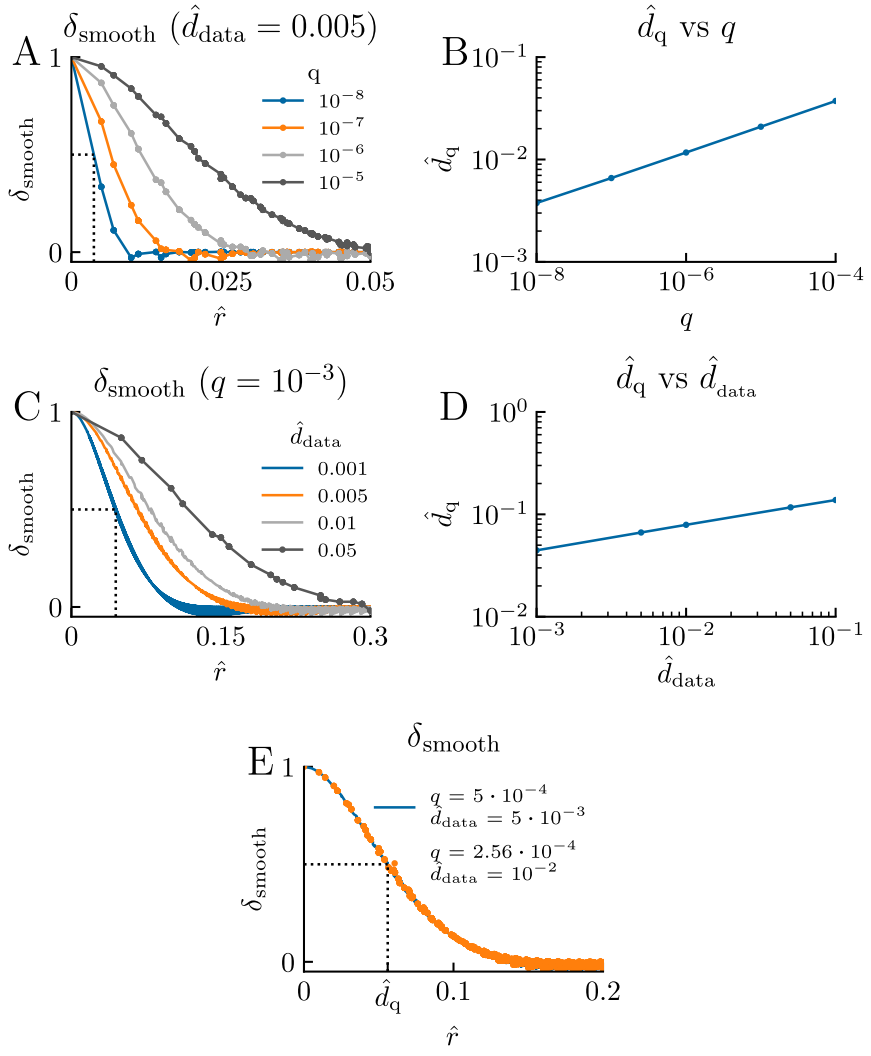

Fig 1. Choice of smoothing parameter in `csaps`. The effect of the smoothing function `csaps` is characterized by a smoothing length $\hat{d}_{\text{q}}$ that is related to the smoothing factor q and the spatial spacing $\hat{d}_{\text{data}}$ through Eq. 14. We found this relationship by smoothing a two-dimensional spatial δ-function using different values of q and $\hat{d}_{\text{data}}$, and plotting the result as a function of the distance $\hat{r}$ from the position of the δ-function. Panels A and C show the normalized smoothed δ-function ($\delta_{\text{smooth}}(\hat{r})$) for different values of q ($\hat{d}_{\text{data}}$ fixed) and $\hat{d}_{\text{data}}$ (q fixed), respectively. The characteristic smoothing length $\hat{d}_{\text{q}}$ is defined as the distance corresponding to $\delta_{\text{smooth}} = 0.5$ (dotted lines) and is plotted as a function of q and $\hat{d}_{\text{data}}$ in panels B and D, respectively. In panel E we demonstrate how different sets of q and $\hat{d}_{\text{data}}$-values correspond to the same $\hat{d}_{\text{q}}$, that is, the same smoothing effect.

The detailed value of the constant k in Eq. 14 is not critical for our purpose. We set it by reading out the value for $\hat{d}_{\mathrm{q}}$ from the graph for the case with $\hat{d}_{\mathrm{data}} = 5 \cdot 10^{-3}$ and $q = 5 \cdot 10^{-4}$ as shown with a blue line in Fig. 1E. The readout value, $\hat{d}_{\mathrm{q}} \approx 5.6 \cdot 10^{-2}$, was then used to calculate k from Eq. 14. After rounding to one decimal, this gave $k = 1.4$.

Thus, given $\hat{d}_{\mathrm{data}}$ and a chosen value of $\hat{d}_{\mathrm{q}}$, we can find which q to use in `csaps` in Eq. 11 through the following formula:

$$q = \left(\frac{\hat{d}_{\mathrm{q}}}{1.4} \right)^4 \frac{1}{\hat{d}_{\mathrm{data}}}. \tag{15}$$

This equation tells us that if, say, $\hat{d}_{\mathrm{data}}$ increases from $5 \cdot 10^{-3}$ to $1 \cdot 10^{-2}$, then q must decrease from $q = 5 \cdot 10^{-4}$ to about $q = 2.6 \cdot 10^{-4}$ to keep the same smoothing effect, that is, give the same value of $\hat{d}_{\mathrm{q}}$. The dotted orange line in Fig. 1E illustrates that this is indeed the case.

Forward modeling of ground truth pO_2 data

To validate the $CMRO_2$ estimation method, we generate synthetic data of oxygen partial pressure $\hat{P}(\hat{\mathbf{r}})$ by solving Eq. 4 for chosen values of $\hat{M}(\hat{\mathbf{r}})$ and chosen geometries of vascular sources and measurements points. The synthetic data work as a "ground truth." Since we know its true value of $\hat{M}(\hat{\mathbf{r}})$, we can use it to test our estimation method. In the present study, we compute this ground truth data by means of two methods: (i) using the Krogh–Erlang model and (ii) by means of finite-element modeling.

Krogh–Erlang model

In the well-known Krogh–Erlang model [5], a cylindrical geometry, mimicking a straight segment of a blood vessel, was used to model the metabolic consumption of oxygen provided by capillaries in muscles. In Ref. [4], the same model was used to study metabolic consumption of oxygen provided by penetrating arterioles in brain tissue. The model describes the blood vessel as a small cylinder with radius R_{ves} supplying a tissue cylinder with radius R_{t} with oxygen. The further assumptions are (i) uniform consumption of oxygen in the tissue, that is, constant M outside the vessel, (ii) no axial diffusion of oxygen, (iii) $P = P_{\mathrm{ves}}$ at R_{ves}, and (iv) no pressure gradient at the surface of the tissue cylinder, that is, $dP/dr = 0$ at R_{t}. With these four assumptions, the solution of Eq. 4 is found to be

$$P(r) = P_{\mathrm{ves}} + \frac{1}{4} M (r^2 - R_{\mathrm{ves}}^2) - \frac{1}{2} M R_{\mathrm{t}}^2 \ln \frac{r}{R_{\mathrm{ves}}}, \tag{16}$$

for $R_{\mathrm{t}} \geq r \geq R_{\mathrm{ves}}$. This so-called Krogh–Erlang formula predicts the oxygen pressure P in the tissue as a function of the distance r from the vessel's center. For our application we set $P(r) = P_{\mathrm{ves}}$ if $r < R_{\mathrm{ves}}$.

Equation 16 can be written in dimensionless form as

$$\hat{P}(\hat{r}) = \begin{cases} \hat{P}_{\text{ves}}, & \text{if } r < \hat{R}_{\text{ves}} \\ \hat{P}_{\text{ves}} + \frac{1}{4}\hat{M}(\hat{r}^2 - \hat{R}_{\text{ves}}^2) - \frac{1}{2}\hat{M}\hat{R}_{\text{t}}^2 \ln \frac{\hat{r}}{\hat{R}_{\text{ves}}}, & \text{if } \hat{R}_{\text{t}} \geq r \geq \hat{R}_{\text{ves}}. \end{cases} \tag{17}$$

Here we also have introduced $\hat{P}_{\text{ves}} = P_{\text{ves}}/(M^* r^{*2})$, $\hat{r} = r/r^*$, $\hat{R}_{\text{ves}} = R_{\text{ves}}/r^*$, and $\hat{R}_{\text{t}} = R_{\text{t}}/r^*$. Further, the boundary condition $d\hat{P}/d\hat{r} = 0$ for $\hat{r} = \hat{R}_{\text{t}}$ is assumed.

Finite element modeling: FEniCS model

The Krogh–Erlang formula relates the oxygen consumption and the partial oxygen pressure under very specific conditions. Another option is to solve Eq. 6 numerically. This allows for the solutions for more general cases, such as a more complicated geometry with, for example, several arterioles providing oxygen, or an inhomogenous oxygen consumption. We implemented Eq. 6 in the finite element software package FEniCS [14], and verified the implementation by comparing the result to that of the Krogh–Erlang formula.

The FEniCS implementation solves the variational formulation of Eq. 6: Let V be a space of test functions $\{v_1, \ldots v_N\}$ on the computational domain Ω. We aim to find $\hat{P}$ such that

$$\int_\Omega \nabla\hat{P} \cdot \nabla v_i + \hat{M} v_i \, \mathrm{d}x - \int_{\partial\Omega} \nabla\hat{P} \cdot \mathbf{n} \, \mathrm{d}s = 0, \qquad \forall v_i \in V, \tag{18}$$

where $\partial\Omega$ denotes the boundary of the domain, and $\mathbf{n}$ is a normal vector pointing out of the domain. This variational form is obtained by multiplying Eq. 6 with the test function v_i and integrating over Ω, followed by integration by parts of the Laplacian term. Note that as we apply a fixed value for $\hat{P}$ by the blood vessel and no pressure gradient at the boundary of the domain, the boundary integral in Eq. 18 vanishes.

The solution to Eq. 18 gives us $\hat{P}$ on an unstructured finite element mesh. Experimental data is typically measured on a structured Cartesian grid, and to better mimic this we transfer the synthetic data generated by FEniCS to a 2D NumPy array. We do this by first defining a new Cartesian mesh using NumPy with a distance $\hat{d}_{\text{data}}$ between each point. Then, in the next step, we pick out values of $\hat{P}$ from the FEniCS solution corresponding to these positions and save them to a 2D NumPy array. We set $P(r) = P_{\text{ves}}$ if $r < R_{\text{ves}}$.

Noise

We add additive Gaussian noise to the synthetic data using the `normrnd` function in MATLAB. For each value $\hat{P}$ of oxygen partial pressure, whether it comes from the Krogh–Erlang equation or the FEniCS solution, we draw a random number from a Gaussian distribution with mean $\hat{P}$ and standard deviation (SD) $\hat{\sigma}_{\text{P}}$, and replace $\hat{P}$ by this number.

Performance measures of the diffusion-operator method

In order to evaluate the performance of the diffusion-operator method, we test it on the synthetic data and calculate its bias, precision, and accuracy. As precision and accuracy measures we use SD and root-mean-square error (RMSE). The mathematical definitions of these measures are

$$\text{bias} = \frac{1}{N}\sum_{j=1}^{N}(\hat{M}_{\text{est},j} - \hat{M}), \tag{19}$$

$$\text{SD} = \sqrt{\frac{1}{N}\sum_{j=1}^{N}(\hat{M}_{\text{est},j} - \overline{\hat{M}_{\text{est}}})^2}, \tag{20}$$

and

$$\text{RMSE} = \sqrt{\frac{1}{N}\sum_{j=1}^{N}(\hat{M}_{\text{est},j} - \hat{M})^2}, \tag{21}$$

where N is the number of synthetic samples and $\hat{M}_{\text{est},j}$ is the j'th estimate of $\hat{M}$.

The RMSE combines both bias and precision as its squared value MSE is equal to the SD squared plus the bias squared: $\text{MSE} = \text{SD}^2 + \text{bias}^2$ [15].

Results

Illustration of the diffusion-operator method

The principle of the diffusion-operator method for estimation of the net oxygen consumption $M(\mathbf{r})$ from pO_2 measurements $P(\mathbf{r})$ is illustrated in Fig. 2. In this example, we assume the spatial map of pO_2 to follow the Krogh–Erlang formula in Eq. 16, mimicking the situation where a single arteriole is the source of the oxygen, and the oxygen consumption M is constant around the arteriole.

Panel A shows the pressure profile in the radial directions as described by this formula with example parameters P_{ves}, M, and R_{ves} chosen to be in qualitative agreement with example data from Ref. [4], that is, $P_{\text{ves}} = 80\,\text{mmHg}$, $M = 0.001\,\text{mmHg}\mu\text{m}^{-2}$, and $R_{\text{ves}} = 6\,\mu\text{m}$, and R_{t} set to $200\,\mu\text{m}$. Panel B shows a contour plot of this synthetic pO_2 map in 2D. Here dimensionless parameters (cf. Methods) are used with $r^* = 141\,\mu\text{m}$ and the convenient choice $M^* = M$ so that the maximal pressure P_{ves} corresponds to $\hat{P}_{\text{ves}} \approx 4.1$ and $\hat{M} = 1$. We show the pO_2 map in a square window with side lenghts of $282\,\mu\text{m}$ so that the dimensionless position coordinates extends from -1 to 1 along the $\hat{x}$ and $\hat{y}$ axes. With this choice, the corners of the square correspond to a radial distance equal to $\hat{R}_{\text{t}}$, the radius of the tissue cylinder.

The problem of $CMRO_2$ estimation now corresponds to estimating M at the different locations inside the square window based on these recordings. Panel C shows the estimated M (in units of M^*) found by applying the Laplace

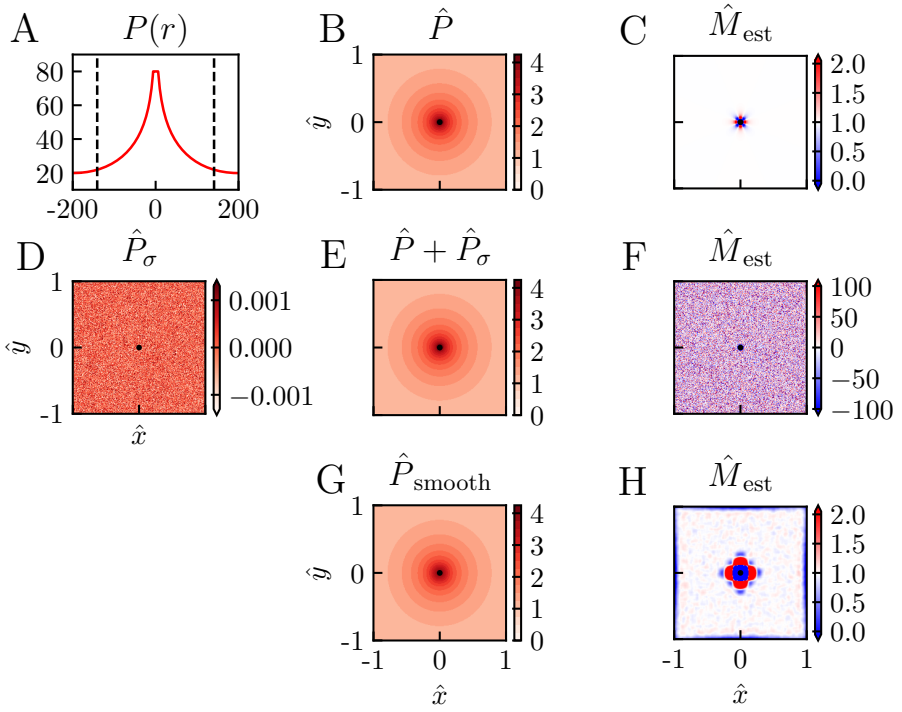

Fig 2. Illustration of diffusion-operator estimation method. Panel A shows an example of a synthetic pO_2 profile calculated using the Krogh–Erlang formula in Eq. 17 without noise. Panel B shows the corresponding 2D representation of this pO_2 data set with use of dimensionless parameters. Panel D shows a map of additive Gaussian noise $\hat{P}_\sigma$ and panel E shows the corresponding pO_2 map where this noise has been added. Panel G shows a data set where smoothing has been applied. Panel C, F, and H show estimated $\hat{M}$s calculated from the pO_2 data in panels B, E, and G, respectively. Parameter values: All panels: $P_{\mathrm{ves}} = 80\,\mathrm{mmHg}$, $R_{\mathrm{ves}} = 6\,\mu\mathrm{m}$, $R_{\mathrm{t}} = 200\,\mu\mathrm{m}$, $M = 0.001\,\mathrm{mmHg}\mu\mathrm{m}^{-2}$. For panel A: $d_{\mathrm{data}} = 1\,\mu\mathrm{m}$. For panels B–H: $\hat{d}_{\mathrm{data}} = 0.007$, $r^* = 141\,\mu\mathrm{m}$, $M^* = M$. For panels D–H: $\hat{\sigma}_{\mathrm{P}} = 5 \cdot 10^{-4}$. For panels G–H: $\hat{d}_{\mathrm{est}} = 0.001$, $\hat{d}_{\mathrm{q}} = 0.04$.

estimator in Eq. 13 on the data in panel B. In this example, the dimensionless distance between the grid points at which pO_2 is "measured" is set to $\hat{d} = 0.007$, corresponding to a physical grid-point distance of about $1\,\mu$m. It is seen that some distance away from the vessel, the estimator predicts $\hat{M}$ very close to 1, that is, $M \simeq M^*$, as it should.

However, close to the vessel, that is, for $\hat{r} \gtrsim \hat{R}_{\text{ves}}$, clearly incorrect values of $\hat{M}$ are obtained. One obvious reason is that the discrete Laplace estimator in Eq. 13 will be inaccurate when one or more of the grid points used in the estimation is inside the vessel. Here the pressure P is not described by Eq. 16 and is instead assumed constant so that $\nabla^2 P \neq M$, cf. Eq. 4. For the present example, a more important reason is that immediately outside the vessel, the pressure profile drops sharply (due to the last term in the Krogh–Erlang formula in Eq. 16) so that the discrete Laplace estimator becomes inaccurate when the grid-point distance $\hat{d}$ is too large. The "flower-like" symmetric pattern of this estimation error in panel C reflects the cartesian symmetry of the estimator in Eq. 13. This discretization error can be reduced by reducing the value of $\hat{d}$, i.e., using a finer grid.

Panel C in Fig. 2 illustrates that if the experimental measurements were noiseless, the Laplace estimator in Eq. 13 could be used directly on the pO_2 data, at least when the grid of recordings is finely spaced. This would apply for any distribution of vessels as long as the estimator $\hat{M}_{\text{est}}$ in Eq. 13 is used sufficiently far away from the vessel wall. Experimental pO_2 data will always contain noise, however, and panel D shows a map of additive Gaussian noise $\hat{P}_\sigma$ with zero mean and standard deviation $\hat{\sigma}_{\text{P}} = 0.0005$. Panel E shows the same synthetic data as in B where this noise has been added, indistiguishable by eye from the noise-free map in panel B. When $\hat{M}_{\text{est}}$ in Eq. 13 is applied on these synthetic data, the estimated values of $\hat{M}$ are wildly inaccurate (panel F). Not only does the estimated values of $\hat{M}$ have much larger magnitudes than the true value of $\hat{M} = 1$, they also have both signs and vary strongly between neighboring grid positions (that is, between neighboring pixels in the map). These poor estimates reflect that the double-derivative operation of the Laplacian estimator corresponds to a high-pass spatial filtering that effectively amplifies the effects of the noise in the data.

This noise in the estimated $\hat{M}$ can be reduced by the use of spatial smoothing, that is, low-pass filtering, of the data $\hat{P}$ before application of $\hat{M}_{\text{est}}$. While the smoothed map $\hat{P}_{\text{smooth}}$ in panel G at first glance does not appear to be very different from the unsmoothed version in panel E, the effect of the smoothing on the estimated M is dramatic (panel H). With the choice of smoothing used in this example (see figure caption for details), quite accurate estimates of $\hat{M}$ are found for a large region of the area around the central vessel (light-colored regions of panel H). However, the smoothing procedure results in large estimation errors in a sizable region around the blood vessel as well as close to the edges of the square data set.

To summarize, suitable smoothing of the pO_2 data before using the Laplace estimator $\hat{M}_{\text{est}}$ may dramatically improve the estimation accuracy. However,

the choice of smoothing is critical: too little low-pass smoothing will not remove enough of the high-frequency spatial noise; too much smoothing will smooth away spatial information in the data and thus give poor estimates of M. Next, we will investigate this dilemma in more detail.

Noise removal versus bias

Figure 3 illustrates the dilemma when choosing the right level of low-pass smoothing of the pO_2 data P before using the Laplace estimator in Eq. 13. In the smoothing algorithm, the quantity described in Eq. 10 was minimized to penalize sharp variations in P_{smooth} while at the same time fitting the synthetic data P_{data}. The level of smoothing is set by the smoothing length d_{q} (or $\hat{d}_{\text{q}}$ in dimensionless units) which is related to the smoothing parameter used in the presently used MATLAB function `csaps` via Eq. 14 (see Methods). This smoothing length describes how much a point (that is, a two-dimensional spatial δ-function) will be smeared out in space. Thus, the larger d_{q} is, the more the pO_2 map will be smeared out or smoothed.

To quantify the performance of the estimator, we use the following three performance measures: bias, SD, and RMSE. The bias (Eq. 19) measures the systematic error in the estimator M_{est} introduced by the smoothing (and discreteness of data points) whether the data is noisy or not. It can be evaluated from noiseless data (that is, with $P_\sigma = 0$), and the results for different values of smoothing are shown on the left of Fig. 3 (panels A, D, G, J). In the case of no smoothing ($\hat{d}_{\text{q}} = 0$, panel A) the only bias comes from the discreteness of the grid of data points, and is only observed close to the vessel. With a small amount of smoothing ($\hat{d}_{\text{q}} = 0.02$, panel D), the bias around the vessel is increased. For $\hat{d}_{\text{q}} = 0.04$ (panel G) and $\hat{d}_{\text{q}} = 0.08$ (panel J) this tendency of increased bias with increasing $\hat{d}_{\text{q}}$ is continued, and some bias is also observed close to the edges of the square grid. For the largest smoothing depicted in panel J, about one-third or so of the map has a bias with a magnitude larger than 100%.

The SD (Eq. 20) measures the precision or the error in the estimation due to the presence of noise. This measure obviously depends on the level of noise P_σ. In the present example in Fig. 3, a Gaussian noise with a SD of $\hat{\sigma}_{\text{P}} = 5 \cdot 10^{-4}$ is used. With $r^* = 141\,\mu\text{m}$ and $M^* = 0.001\,\text{mmHg}\mu\text{m}^{-2}$ as in Fig. 2 this corresponds to a physical noise level of $\sigma_{\text{P}} \approx 0.01\,\text{mmHg}$. The SD for different amounts of smoothing is shown in the middle column of Fig. 3 (panels B, E, H, K). Three observations of note are that (i) the SD of the estimates is extremely large when no smoothing is applied ($\hat{d}_{\text{q}} = 0$), (ii) the SD decreases with increasing $\hat{d}_{\text{q}}$, and (iii) unlike for the bias, the SD has similar values at the different positions.

An essential feature of the SD is that it is proportional to the SD of the noise in the pressure $\hat{\sigma}_{\text{P}}$. Thus if $\hat{\sigma}_{\text{P}}$ was doubled to 0.001, the SDs in panels B, E, H, and K would be doubled as well.

The accuracy of the estimator M_{est} is measured by the RMSE (Eq. 21), which incorporates both the bias and precision (SD) through the relation

$$\text{RMSE} = \sqrt{\text{bias}^2 + \text{SD}^2}\,. \tag{22}$$

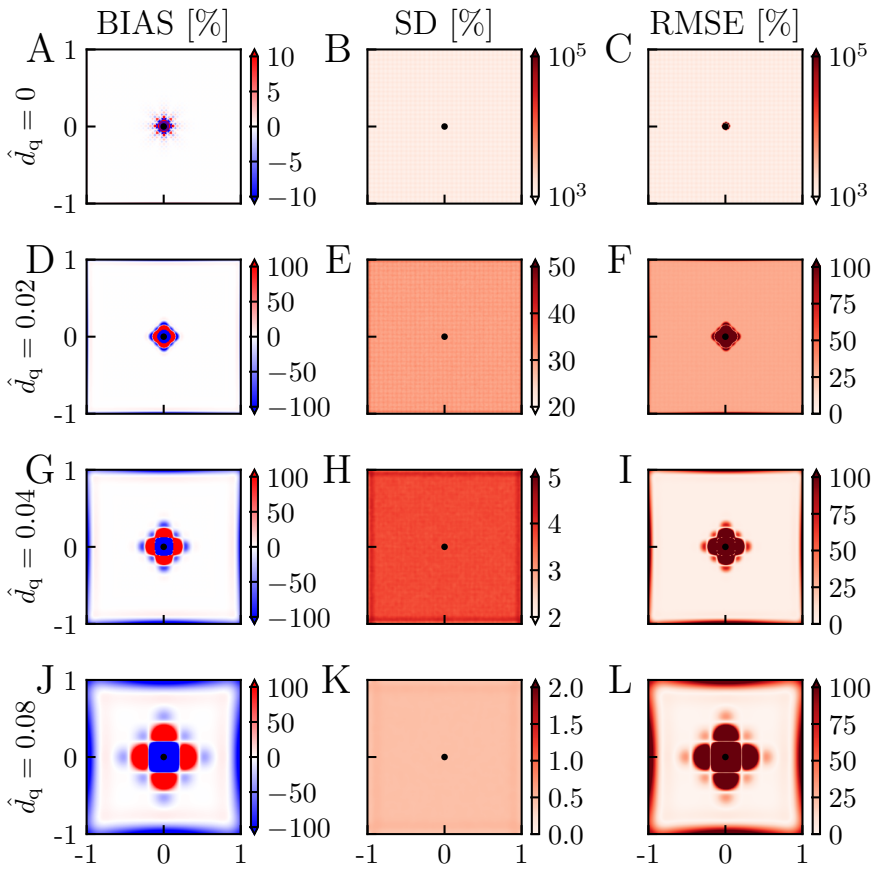

Fig 3. Illustration of noise removal versus bias. A, D, G, and J: Bias of $\hat{M}_{\text{est}}$ for different values of $\hat{d}_{\text{q}}$. B, E, H, and K: SD of $\hat{M}_{\text{est}}$ for different values of $\hat{d}_{\text{q}}$. C, F, I, and L: RMSE of $\hat{M}_{\text{est}}$ for different values of $\hat{d}_{\text{q}}$. Bias is computed from Eq. 19 for the case without noise $\hat{\sigma}_{\text{P}} = 0$ so that a single estimate of $\hat{M}_{\text{est}}$ is sufficient, that is $N = 1$ in Eq. 19. SD is computed from Eq. 20 with 10^4 estimates of $\hat{M}_{\text{est}}$, that is, $N = 10^4$. In the computation of SD and RMSE, $\hat{\sigma}_{\text{P}} = 5 \cdot 10^{-4}$. All performance measures are given as the percentage of the ground truth value $\hat{M} = 1$. Note also that the MATLAB routine `csaps` is used also for the case without smoothing ($\hat{d}_{\text{q}}$=0) with $q = 0$ inserted in Eq. 11. Other parameter values: $\hat{d}_{\text{data}} = 0.007$, $P_{\text{ves}} = 80\,\text{mmHg}$, $R_{\text{ves}} = 6\,\mu\text{m}$, $R_{\text{t}} = 200\,\mu\text{m}$, $M = 0.001\,\text{mmHg}\mu\text{m}^{-2}$, $r^* = 141\,\mu\text{m}$, $M^* = M$.

This measure describes the total statistical uncertainty of the estimates when M_{est} is applied on individual data sets. The bias increases with increasing $\hat{d}_{\text{q}}$ (panels A, D, G, J), whereas the SD instead decreases with increasing $\hat{d}_{\text{q}}$ (panels B, E, H, K). One would thus expect a suitable intermediate value of $\hat{d}_{\text{q}}$ to give the smallest RMSE. For the example in Fig. 3, we indeed see that for the values of $\hat{d}_{\text{q}}$ considered, the intermediate value $\hat{d}_{\text{q}} = 0.04$ (panel I) offers the best compromise between bias and noise removal and gives the smallest RMSE. For this value of $\hat{d}_{\text{q}}$, the RMSE is smaller than 25% for almost all positions except for a region around the blood vessel.

The large RMSE close to the blood vessel even for the "best" choice of $\hat{d}_{\text{q}}$ in panel I reflects the large bias at these locations (panel G).

Choice of smoothing length d_{q}

As illustrated in the previous section, a key question when using the Laplace estimator in Eq. 13 is the choice of the amount of smoothing, or more specifically, the choice of the smoothing length d_{q}. This will not only depend on the noise level, but also the spatial resolution of the data as described by the grid resolution, that is, the distance between adjacent points on the measurement grid, d_{data}. Since the bias is independent of the noise level, and the SD is linearly proportional to the SD σ_{P} of the noise, it is convenient to first explore the interplay between d_{q} and d_{data} for the bias and SD separately.

In Fig. 4, we show how the bias varies with d_{data} and d_{q} for three choices of parameter values of each: $\hat{d}_{\text{data}} = 0.0035$, 0.007, 0.014 (here corresponding to physical grid resolutions of approximately $0.5\,\mu$m, $1\,\mu$m, and $2\,\mu$m, respectively), $\hat{d}_{\text{q}} = 0$, 0.02, 0.04 (corresponding to physical smoothing lengths of approximately $0\,\mu$m, $3\,\mu$m, and $6\,\mu$m, respectively). For the case with no smoothing (panels A, D, G), we observe that the bias increases with increasing $\hat{d}_{\text{data}}$. This illustrates that the error due to the discreteness of the Laplace estimator is sensitive to d_{data} even when d_{est} is set to a very small number ($\hat{d}_{\text{est}} = 0.001$, cf. Methods). This is not surprising because decreasing the grid resolution from $\hat{d}_{\text{data}}$ to $\hat{d}_{\text{est}}$ means that we estimate $\hat{P}$ at a denser grid of points than what is directly available in the data. With smoothing added (two rightmost columns of panels), the bias increases, and the larger the value of $\hat{d}_{\text{q}}$, the larger the bias. (Note the difference in color scales in the figure.)

In Fig. 5 we correspondingly show how the SD varies with d_{data} and d_{q} for the same set of parameters as in Fig. 4 for a fixed level of noise in the data, $\hat{\sigma}_{\text{P}} = 5 \cdot 10^{-4}$. Here the most important feature is that the SD is strongly reduced with increased smoothing, that is, increasing d_{q} (from left to right). For the smoothed cases (two rightmost columns) we also observe that SD increases with increasing d_{data} (i.e., making the grid of measurements more sparse).

Figure 6 shows the RMSE, computed from Eq. 22, for the example bias and SD shown in Figs. 4 and 5, respectively. For the smoothed cases (two right columns) we observe that the RMSE always increases with the $\hat{d}_{\text{data}}$. Thus with the noise level fixed, it is (unsurprisingly) always advantageous to have a dense

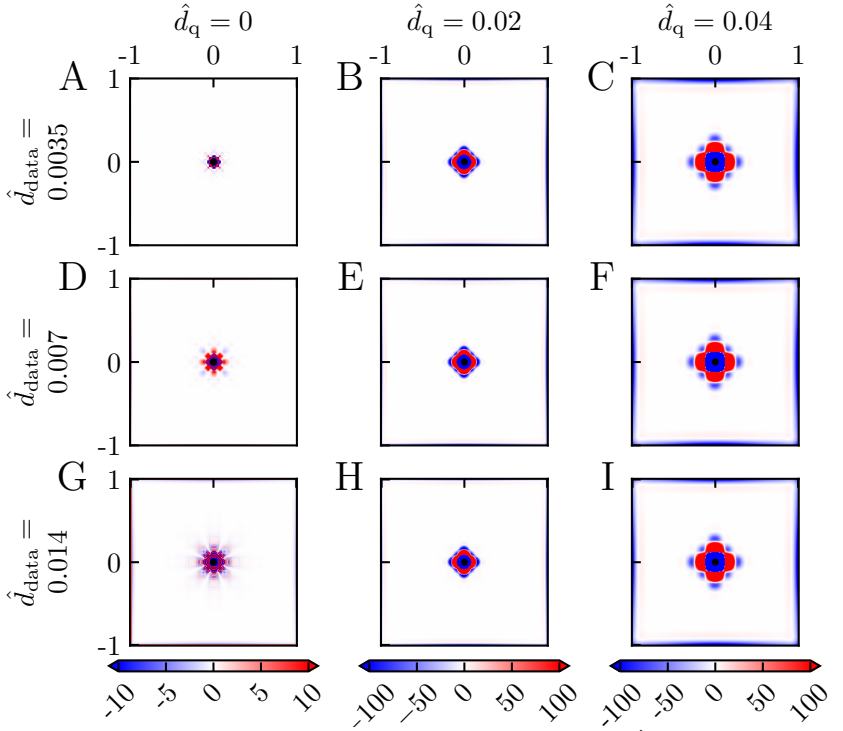

Fig 4. Bias for different smoothing. A-I: Bias of $\hat{M}_{\text{est}}$ for different values of $\hat{d}_{\text{q}}$ (increasing from left to right) and $\hat{d}_{\text{data}}$ (increasing from top to bottom) computed from Eq. 19 and given as the percentage of the ground truth value $\hat{M} = 1$. There was no noise added to the pressure data so that a single estimate of $\hat{M}_{\text{est}}$ is sufficient, that is $N = 1$ in Eq. 19. Parameter values: $P_{\text{ves}} = 80\,\text{mmHg}$, $R_{\text{ves}} = 6\,\mu\text{m}$, $R_{\text{t}} = 200\,\mu\text{m}$, $M = 0.001\,\text{mmHg}\mu\text{m}^{-2}$, $r^* = 141\,\mu\text{m}$, $M^* = M$.

measurement grid. For the noise level in this example we see that the choice $\hat{d}_{\text{q}} = 0.02$ (second column) gives a good estimate for $\hat{d}_{\text{data}} = 0.0035$, that is, low RMSE, for large parts of the map. For $\hat{d}_{\text{data}} = 0.007$ and especially $\hat{d}_{\text{data}} = 0.014$ the SD is not sufficiently reduced, and the RMSE is overall high. For the case with a larger smoothing ($\hat{d}_{\text{q}} = 0.04$, third column) the SD is much reduced for all values of $\hat{d}_{\text{data}}$. However, the region with large bias around the vessel is increased, and the spatial region in which RMSE values are small is shrunken.

Note that the SD results in Fig. 5 and the RMSE results in Fig. 6 only pertain to the particular noise level used in the example, that is, $\hat{\sigma}_{\text{P}} = 5 \cdot 10^{-4}$. However, the SD is proportional to the noise level, so a doubling of $\hat{\sigma}_{\text{P}}$ would simply double the SD from what is shown in Fig. 5. RMSE results analogous to Fig. 6 for other noise levels can thus be obtained by appropriate scaling of SD in Eq. 22.

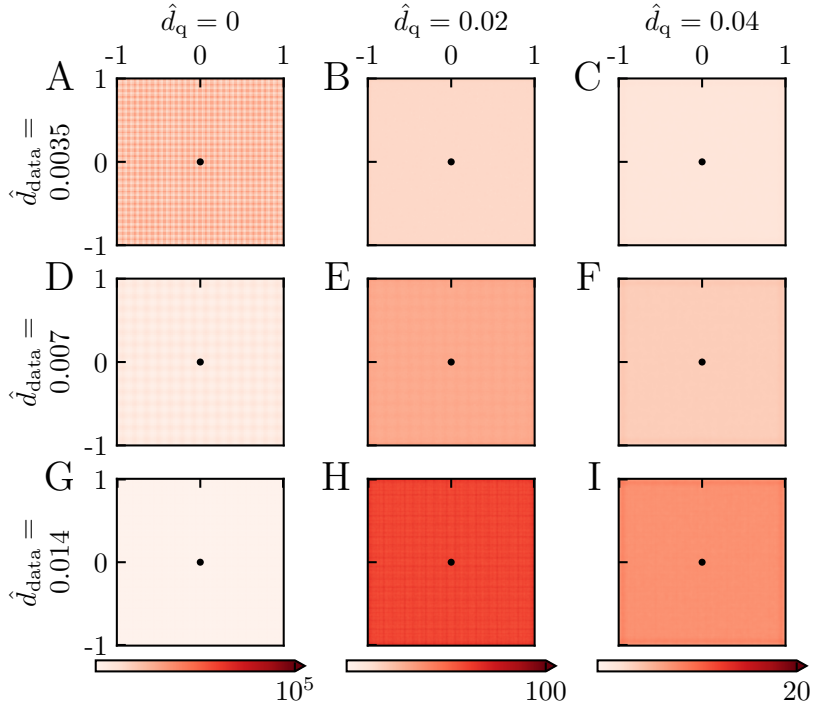

Fig 5. SD for different smoothing - fixed noise level. A-I: SD of $\hat{M}_{est}$ for different values of $\hat{d}_q$ (increasing from left to right) and $\hat{d}_{data}$ (increasing from top to bottom) computed from Eq. 20 with $N = 10^4$. Values are given as the percentage of the ground truth value $\hat{M} = 1$. (Note that the grid-like pattern visible in some of the panels is a numerical artifact resulting from the application of the MATLAB routine `csaps`.) Parameter values: $\hat{\sigma}_P = 5 \cdot 10^{-4}$, $P_{ves} = 80\,\text{mmHg}$, $R_{ves} = 6\,\mu\text{m}$, $R_t = 200\,\mu\text{m}$, $M = 0.001\,\text{mmHg}\mu\text{m}^{-2}$, $r^* = 141\,\mu\text{m}$, $M^* = M$.

Estimation of $CMRO_2$ for other example situations

In the examples above, we have applied the diffusion-operator method to the situation with (i) a constant value of M and (ii) a single vessel providing the oxygen so that the pO_2 map is described by the Krogh–Erlang formula in Eq. 16. For these examples, an alternative approach could be to estimate M by fitting the Krogh–Erlang formula directly to measured data [4]. In other situations where, for example, M varies with position or several nearby vessels provide the oxygen so that the circular symmetry assumed in the Krogh–Erlang formula does not hold, this approach would not be applicable. In contrast, the current diffusion-operator method does not assume a constant M and can be applied to cases where multiple arterioles deliver oxygen.

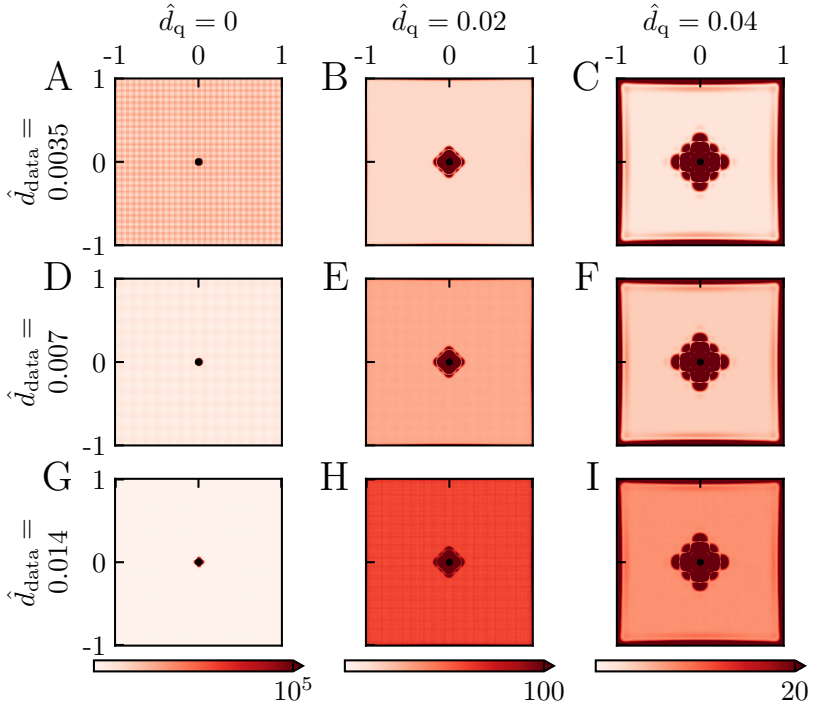

Fig 6. Root-mean-square error for different smoothing - fixed noise level. A-I: RMSE computed from Eq. 21 for the bias and SDs shown in Figs. 4 and 5, respectively. Values are given as the percentage of the ground truth value $\hat{M} = 1$.

Spatially varying $CMRO_2$

To illustrate the applicability of the Laplace estimator to the situation with varying M, we consider in Fig. 7 a hypothetical case where a single vessel provides the oxygen, but where the parameter M varies with distance from the vessel. Specifically, the value of M is assumed to be smaller far away from the vessel. This can be due to genuine differences in $CMRO_2$. Alternatively, this can mimic the situation where a distant bed of capillaries acts as an oxygen source unaccounted for in the model and leading to an apparent decrease in $CMRO_2$. Here the solution of the Poisson equation in Eq. 4 must be found numerically, and in panel A and B, we illustrate the pO_2 maps found using the FEniCS numerical solver (see Methods). Panel A shows a 1D representation of this pO_2 profile in the radial direction for the case without any added noise. Panel B correspondingly shows a 2D colormap of the same synthetic data when noise has been added. The dotted lines in panel A mark the distance from the vessel ($|\hat{r}| = 0.7$) where the value of $\hat{M}$ changes. With the characteristic length r^* used throughout this paper, this corresponds to a physical distance of approximately

100 μm, which is a typical size of the region around diving arterioles void of capillaries in the rat cortex [4]. We see in panel A that beyond this distance, there is almost no decay in the pO_2 compared to that within the capillary-free region.

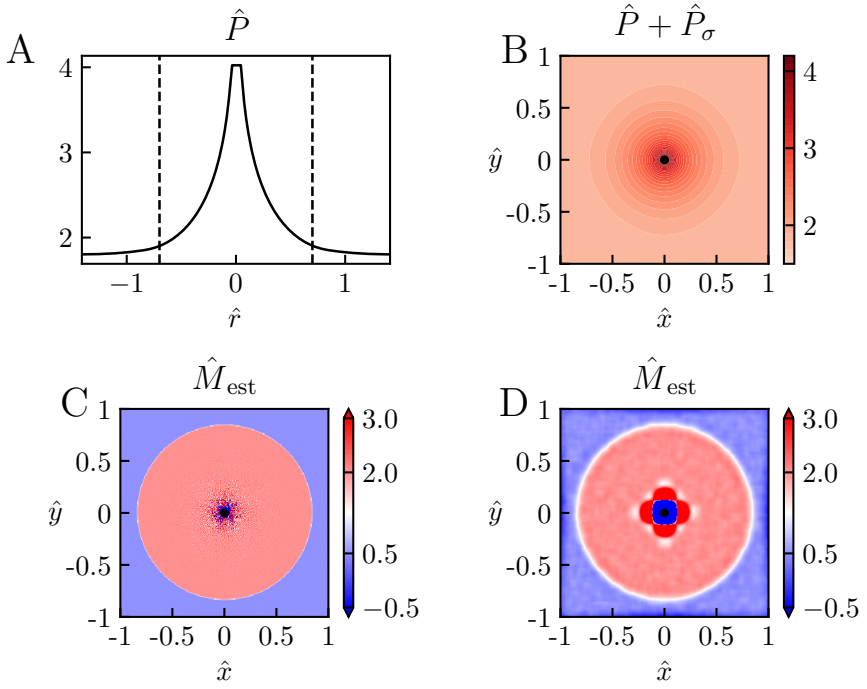

Fig 7. Estimation of spatially varying M. Diffusion-operator estimation of $\hat{M}$ for the case with a single oxygen-releasing vessel in the center with a larger $\hat{M}$ close to the vessel ($\hat{r} < 0.7$ and $\hat{M} = 2$) than far away ($\hat{r} > 0.7$ and $\hat{M} = 0.5$). The synthetic pO_2 maps were calculated using the FEniCS numerical solver (see Methods). A: 1D illustration of pO_2 map for the case without noise ($\hat{\sigma}_{\text{P}} = 0$). The dotted lines mark the boundary between different levels of $\hat{M}$. B: 2D illustration of the case with noise added ($\hat{\sigma}_{\text{P}} = 0.0005$). C: Estimated $\hat{M}$ from the noise-less data without use of smoothing. D: Estimated $\hat{M}$ from the data in B (where noise is present) with use of smoothing ($\hat{d}_{\text{q}} = 0.04$). Other parameter values: $\hat{d}_{\text{data}} = 0.007$, $P_{\text{ves}} = 80\,\text{mmHg}$, $R_{\text{ves}} = 6\,\mu\text{m}$, $r^* = 141\,\mu\text{m}$, $M^* = 10^{-3}$.

When using the Laplace estimator on the noise-free data, we obtain excellent estimates of M, that is, $\hat{M}_{\text{est}} \approx 2$ within the capillary-free region and $\hat{M}_{\text{est}} \approx 0.5$ outside this region (panel C). We only observe sizable errors in the immediate vicinity of the vessel, the errors stemming from the discreteness of the synthetic pO_2 data used in the estimation ($\hat{d}_{\text{data}} = 0.007$). Further, when using the Laplace estimator on a smoothed version of the data in Fig. 7B, we still obtain good estimates of $\hat{M}$ some distance away from the vessel. This is in agreement

with the low values for the RMSE found for suitable smoothing of noisy data for the case with constant $\hat{M}$ in Fig. 6.

Several vessels providing oxygen

An example of a situation where multiple nearby vessels serve as oxygen sources is shown in Fig. 8. Again, no analytical solution for the pO_2 map is available, and the Poisson equation is instead computed by means of FEniCS. As observed in the left panel, the circular symmetry of the pO_2 map seen in the earlier examples is broken around the vessels, but the Laplace estimator is still able to accurately estimate $\hat{M}$ except in locations close to the vessels (right panel).

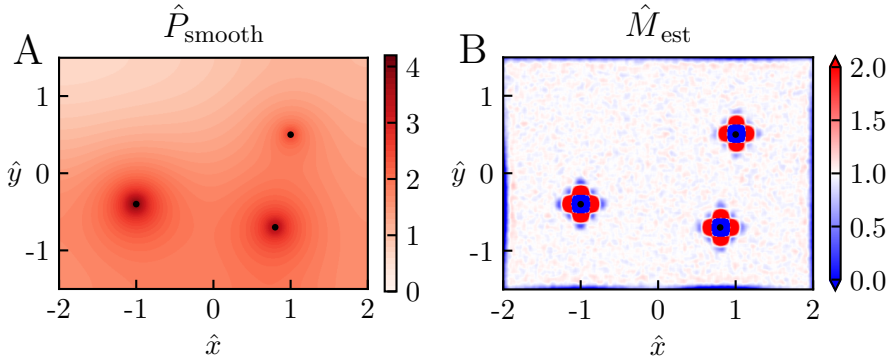

Fig 8. Estimation of M with several vessels providing oxygen. Example of diffusion-operator estimation for a situation where three vessels release oxygen into the tissue. The synthetic pO_2 map was calculated using the FEniCS numerical solver (see Methods). Here P_{ves} is set to 80 mmHg, 70 mmHg, and 50 mmHg for the vessel on the left, lower right, and upper right, respectively, whereas R_{ves} is set to 6 μm for all vessels. Noise is added to the synthetic data in panel A ($\hat{\sigma}_{\text{P}} = 0.0005$), and $\hat{d}_{\text{q}} = 0.04$ is used in the smoothing to provide the estimates of $\hat{M}$ in panel B. Other parameter values: $\hat{d}_{\text{data}} = 0.007$, $M = 0.001\,\text{mmHg}\mu\text{m}^{-2}$, $r^* = 141\,\mu$m, $M^* = M$.

Estimation of spatially-averaged M

So far, we have used the Laplace estimator to estimate spatial maps of M. The Laplace estimator can give accurate estimates as long as the noise level is not too large, but the estimates of M in the immediate vicinity of the oxygen-releasing blood vessels are typically inaccurate due to the bias introduced by the smoothing procedure.

In situations where the pO_2 data are too noisy to give reliable spatially resolved maps of estimated M, one can still obtain estimates of spatially-averaged values of M (as when estimating $CMRO_2$ based on fitting the Krogh–Erlang model in Eq. 16 to experimental data [4]). The obvious procedure for estimating

such average values $M_{\mathrm{est,av}}$ is to take the average over spatially resolved values of M_{est}, that is

$$M_{\mathrm{est,av}} = \frac{1}{N}\sum_{i=1}^{N} M_{\mathrm{est}}(\mathbf{r}_i). \tag{23}$$

The SD of $M_{\mathrm{est,av}}$ is then expected to be a factor $\sqrt{N}$ reduced compared to the SD for the spatially resolved estimates $M_{\mathrm{est}}(\mathbf{r})$.

The bias is not reduced by such an averaging procedure, however. To reduce the effects of smoothing-induced bias, one possible procedure is to take the average of M only for positions outside a circular region around the oxygen-delivering vessel. As illustrated in Fig. 9A this can reduce the bias in the $M_{\mathrm{est,av}}$ substantially. Larger values of the smoothing length $\hat{d}_{\mathrm{q}}$ give larger regions of large bias around the vessel (Fig. 4). Thus larger areas around the vessel, parameterized by the diameter $\hat{d}_{\mathrm{cut}}$, should be removed from the averaging sum in Eq. 23 to keep the bias small. This removal of area from the averaging sum implies a smaller value for N in Eq. 23 and thus a larger value of SD of $M_{\mathrm{est,av}}$. Again, a compromise between the bias and the SD must be found to get the most accurate estimate.

This compromise is illustrated in Figs. 9B–G. Panel B shows the spatially resolved RMSE for a case with low noise corresponding to no smoothing applied (cf. left column of Fig. 6). Here the noise level is so low that even without smoothing, the SD of $M_{\mathrm{est,av}}$ becomes $< 1\%$ for all averaging areas considered, that is, all choices of $\hat{d}_{\mathrm{cut}}$ (cf. $\hat{d}_{\mathrm{q}} = 0$ in panel C). With smoothing applied, the SD of $M_{\mathrm{est,av}}$ becomes even smaller, much $< 0.1\%$ (panel C). We also note that the SD is largest for the largest value of $\hat{d}_{\mathrm{cut}}$, reflecting that here the averaging area (and thus N in Eq. 23) is the smallest. The corresponding RMSE is shown in panel D. For this low-noise situation, there is nothing to gain by doing smoothing when estimating $M_{\mathrm{est,av}}$. The lowest RMSEs are obtained for $\hat{d}_{\mathrm{q}} \approx 0$ since smoothing reduces the accuracy of the estimates due to the bias introduced (cf. panel A).

The situation with a much higher noise level ($\hat{\sigma}_{\mathrm{P}}$ a factor 100 larger, that is, $\hat{\sigma}_{\mathrm{P}} = 5 \cdot 10^{-2}$) is shown in panels E–G. The spatially resolved RMSE using a smoothing factor of $\hat{d}_{\mathrm{q}} = 0.1$ is seen to give large lobes with high RMSE values around the vessel (panel E). Moreover, the typical RMSE value outside the lobe region is about 120%. The SD of $M_{\mathrm{est,av}}$ (panel F) is seen to be on the order of 50% for the case without smoothing ($\hat{d}_{\mathrm{q}} = 0$), and a smaller RMSE can thus be obtained with smoothing applied (panel G). The smallest RMSE, less than $\sim 10\%$, is obtained for $\hat{d}_{\mathrm{q}} \approx 0.1$ and $\hat{d}_{\mathrm{cut}} = 0.3$.

This high-noise example illustrates how accurate estimates of M_{av} can be obtained even when the spatially resolved estimates for M have a large uncertainty. With the parameter values used here, that is, $M^* = 0.001\,\mathrm{mmHg}\mu\mathrm{m}^{-2}$ and $r^* = 141\,\mu\mathrm{m}$, a $\hat{\sigma}_{\mathrm{P}}$ of $5 \cdot 10^{-2}$ corresponds to a physical noise level σ_{P} of $\approx 1\,\mathrm{mmHg}$. (Here we have used that $\sigma_{\mathrm{P}} = \hat{\sigma}_{\mathrm{P}} M^* r^{*2}$, cf. Eq. 6.) For comparison, the corresponding pO_2 at the vessel wall in this example would be $P_{\mathrm{ves}} = 80\,\mathrm{mmHg}$.

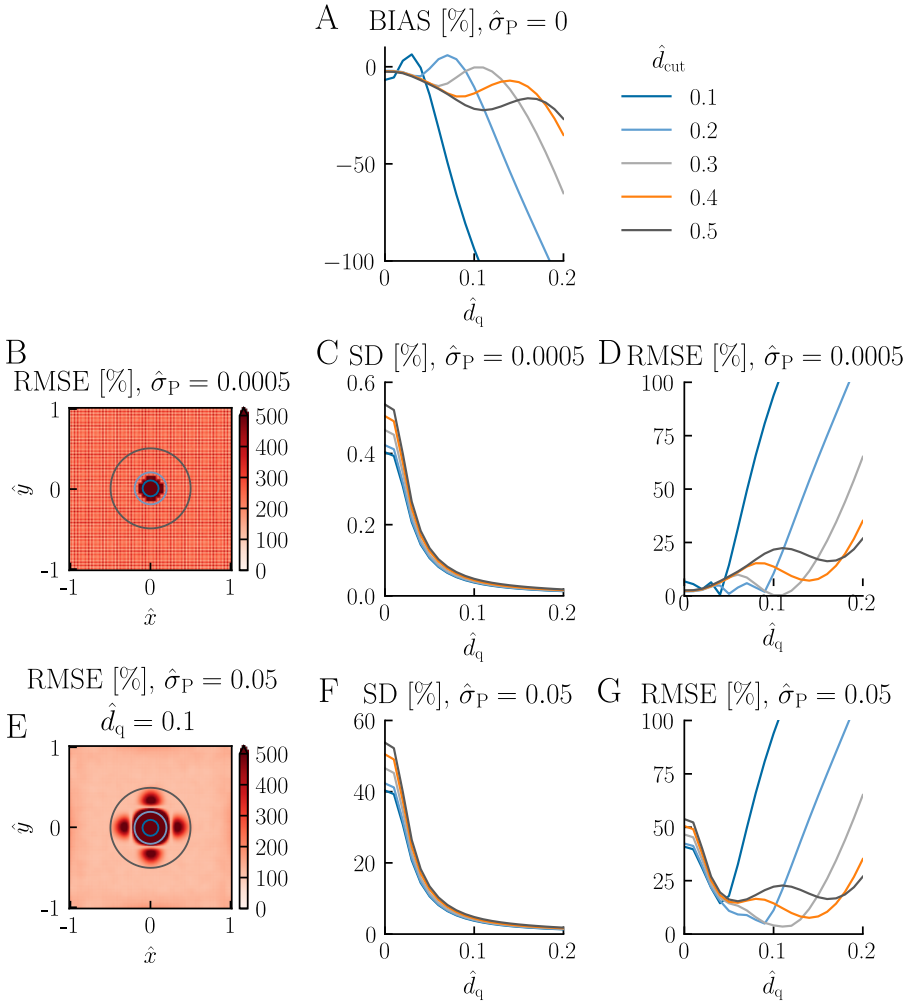

Fig 9. Estimation of spatially-averaged M. Illustration of accuracy of the estimation of spatially-averaged M for different values of the diameter $\hat{d}_{cut}$ of the circular disc removed from the average in Eq. 23. $N = 1000$ has been used in the estimation of the standard deviation (Eq. 20). Other parameter values: All panels: $\hat{d}_{data} = 0.035$, $P_{ves} = 80\,\text{mmHg}$, $R_{ves} = 6\,\mu\text{m}$, $R_t = 200\,\mu\text{m}$, $M = 0.001\,\text{mmHg}\mu\text{m}^{-2}$, $r^* = 141\,\mu\text{m}$, $M^* = M$. For panel A: $\hat{\sigma}_P = 0$. For panels B-D: $\hat{\sigma}_P = 5 \cdot 10^{-4}$. For panels E-G: $\hat{\sigma}_P = 5 \cdot 10^{-2}$, $\hat{d}_q = 0.1$. Note that for figure clarity, only the circles corresponding to $\hat{d}_{cut} = 0.1$, 0.2, and 0.5 are shown in panels B and E.

Discussion

In the present paper, we have introduced a new method, the diffusion-operator method, to provide spatially resolved maps of $CMRO_2$ estimates based on two-photon measurements of pO_2 [3, 4]. The method has two key steps: (i) spatial smoothing of measured pO_2 maps followed by (ii) application of double spatial derivatives in two spatial dimensions, that is, a Laplace operator. This method is an alternative to the Krogh–Erlang method where a spatially averaged value of $CMRO_2$ is obtained around arterioles assuming circular symmetry [4].

Choice of inverse-modeling method

The present diffusion-operator method is a new approach to the inverse diffusion problem in the context of $CMRO_2$ estimation from high-resolution pO_2 data obtained with two-photon microscopy. The two key elements of the method are (i) the Poisson equation in Eq. 4 describing how estimates of $CMRO_2$, or more precisely the variable $M(\mathbf{r})$ in principle can be found by applying the Laplace operator on measured pO_2 maps $P_{\text{data}}(\mathbf{r})$, and (ii) the use of a smoothing routine on $P_{\text{data}}(\mathbf{r})$ to reduce effects of spatial noise before application of the Laplace operator. The development of the inverse-modeling method was mainly motivated by the need to have a method that is conceptually clear, easy to use, and based on publicly available software.

As the double spatial-derivative operation in the diffusion-operator approach is inherently sensitive to spatial noise, the choice of a suitable smoothing method is thus essential for obtaining accurate $CMRO_2$ estimates. The ideal smoothing method should reduce the effects of this spatial noise without introducing large biases in the resulting estimates. We performed smoothing using the cubic smoothing spline function `csaps` from MATLAB's Curve Fitting Toolbox. This method minimizes the square deviation between the estimated and measured data (so-called L2 norm) while penalizing large double-spatial derivatives in the smoothed pO_2 maps (Eq. 10). However, other smoothing methods could be used, for example with norms other than L2 or using different types of splines. Also, since $CMRO_2$, or more precisely the variable M in Eq. 4, is proportional to double spatial derivatives, the smoothing method inherent in `csaps` effectively penalizes large magnitudes of M and thus introduces an unwanted bias. An alternative approach could be to penalize instead changes in the spatial derivatives of M, that is, third spatial derivatives of the pO_2. Finally, while `csaps` allows for different weighting of different locations within the map, the weighting functions are restricted to be spatially separable in the x and y directions. For the present application, this limitation is not optimal as it would be preferable to exclude only a small region in and around the vessel.

While the exploration of effects of different smoothing methods on estimation accuracy is beyond the current scope, an obvious next step would be to test the accuracy of the diffusion-operator method with other smoothing methods. In particular, it would be interesting to explore to what extent other methods could reduce the size and magnitude of the lobes of large bias seen around the

vessel in Fig. 4. The present MATLAB scripts, which can be found online at https://github.com/CINPLA/CMRO2estimation, are designed to allow for an easy exchange of smoothing methods for such exploration.

Use of the diffusion-operator method

The noise level and sampling distance in the experimental pO_2 data reported in Ref. [4] were too large to allow for reliable estimation of spatially resolved maps of $CMRO_2$ (results not shown). Further advancements in engineering of brighter and more sensitive optical pO_2 probes and further development of optical instrumentation will improve the measurement accuracy [4] and facilitate estimation of such maps. Additionally, other inverse-modeling methods may allow for more accurate spatially-resolved $CMRO_2$ estimation based on the same set of data.

Pooling of spatially-resolved estimates (as described in Eq. 23) will always improve the accuracy, but this will be at the expense of spatial resolution. This trade-off can be investigated within the present version or future variations of the diffusion-operator method using the scripts accompanying this paper. Estimation accuracy can be studied systematically with model-based ground truth data (either based on the Krogh–Erlang model or based on FEniCS simulations) using the same grid density and noise levels as those in the experimental setting.

Generalization of the diffusion-operator method

Here the diffusion-operator method has been applied to estimation of $CMRO_2$ for the case with 2D measurements of (assumed) steady state pO_2 data. The diffusion-operator method straightforwardly generalizes to the 3D situation and also the non-stationary case where the pO_2 varies with time. With time-resolved measurements of pO_2 across a 3D volume of brain tissue, spatiotemporally resolved estimates of $CMRO_2$ can be found by an analogous inverse-modeling problem based on Eq. 7. Also here, model-based validation of the estimation method can easily be pursued with synthetic data generated by finite element modeling, for example, using FEniCS.

Disclosures

The authors declare that no competing interests exists. Early versions of some of the present work have been published as a Master's thesis [16] and in abstract form [17].

Acknowledgements

We thank Payam Saisan for useful input in the initial phase of the project and gratefully acknowledge support from the Research Council of Norway via the BIOTEK2021 Digital Life project "Digibrain", Grant No. 248828, and the BRAIN Initiative, Grant No. R01MH111359.

References

[1] Buxton, R. "Interpreting oxygenation-based neuroimaging signals: the importance and the challenge of understanding brain oxygen metabolism". In: *Frontiers in neuroenergetics* vol. 2 (2010), p. 8.

[2] Devor, A. et al. "Neuronal basis of non-invasive functional imaging: from microscopic neurovascular dynamics to BOLD fMRI". In: *Neural metabolism in vivo*. Springer, 2012, pp. 433–500.

[3] Sakadžić, S. et al. "Two-photon high-resolution measurement of partial pressure of oxygen in cerebral vasculature and tissue". In: *Nature methods* vol. 7, no. 9 (2010), p. 755.

[4] Sakadžić, S. et al. "Two-photon microscopy measurement of cerebral metabolic rate of oxygen using periarteriolar oxygen concentration gradients". In: *Neurophotonics* vol. 3, no. 4 (2016), p. 045005.

[5] Krogh, A. "The number and distribution of capillaries in muscles with calculations of the oxygen pressure head necessary for supplying the tissue". In: *The Journal of physiology* vol. 52, no. 6 (1919), pp. 409–415.

[6] Goldman, D. "Theoretical models of microvascular oxygen transport to tissue". In: *Microcirculation* vol. 15, no. 8 (2008), pp. 795–811.

[7] Isakov, V. *Inverse problems for partial differential equations*. Springer, 2017.

[8] Kagawa, Y., Sun, Y., and Matsumoto, O. "Inverse solution for poisson equations using drm boundary element models—identification of space charge distribution". In: *Inverse problems in engineering* vol. 1, no. 3 (1995), pp. 247–265.

[9] Farcas, A. et al. "A dual reciprocity boundary element method for the regularized numerical solution of the inverse source problem associated to the Poisson equation". In: *Inverse problems in engineering* vol. 11, no. 2 (2003), pp. 123–139.

[10] Kołodziej, J. A., Mierzwiczak, M., and Ciałkowski, M. "Application of the method of fundamental solutions and radial basis functions for inverse heat source problem in case of steady-state". In: *International communications in heat and mass transfer* vol. 37, no. 2 (2010), pp. 121–124.

[11] Frąckowiak, A., Wolfersdorf, J., and Ciałkowski, M. "Solution of the inverse heat conduction problem described by the Poisson equation for a cooled gas-turbine blade". In: *International journal of heat and mass transfer* vol. 54, no. 5-6 (2011), pp. 1236–1243.

[12] Nicholson, C. "Diffusion and related transport mechanisms in brain tissue". In: *Reports on progress in physics* vol. 64, no. 7 (2001), p. 815.

[13] Devor, A. et al. ""Overshoot" of O_2 is required to maintain baseline tissue oxygenation at locations distal to blood vessels". In: *Journal of neuroscience* vol. 31, no. 38 (2011), pp. 13676–13681.

[14] Logg, A., Mardal, K.-A., and Wells, G. *Automated solution of differential equations by the finite element method: The FEniCS book*. Vol. 84. Springer Science & Business Media, 2012.

[15] Wasserman, L. *All of statistics: a concise course in statistical inference*. Springer Science & Business Media, 2013.

[16] Sætra, M. J. "Estimation of metabolic oxygen consumption from optical measurements in cortex". MA thesis. University of Oslo, 2016.

[17] Sætra, M. J. et al. "Estimation of metabolic oxygen consumption from optical measurements in cortex". In: *26th Annual Computational Neuroscience Meeting*. 2017.